Title

The e+e-→2(π+π-)π0, 2(π+π-)η, K+K-π+π-π0 and K+K-π+π-η cross sections measured with initial-state radiation

Journal

Physical Review D - Particles, Fields, Gravitation and Cosmology, 76(9)

ISSN

1550-7998

Authors

Aubert, B
Bona, M
Boutigny, D
et al.

Publication Date

2007-11-20

DOI

10.1103/PhysRevD.76.092005

The $e^+e^- \to 2(\pi^+\pi^-)\pi^0$, $2(\pi^+\pi^-)\eta$, $K^+K^-\pi^+\pi^-\pi^0$ and $K^+K^-\pi^+\pi^-\eta$ cross sections measured with initial-state radiation

B. Aubert,[1] M. Bona,[1] D. Boutigny,[1] Y. Karyotakis,[1] J. P. Lees,[1] V. Poireau,[1] X. Prudent,[1] V. Tisserand,[1] A. Zghiche,[1] J. Garra Tico,[2] E. Grauges,[2] L. Lopez,[3] A. Palano,[3] M. Pappagallo,[3] G. Eigen,[4] B. Stugu,[4] L. Sun,[4] G. S. Abrams,[5] M. Battaglia,[5] D. N. Brown,[5] J. Button-Shafer,[5] R. N. Cahn,[5] Y. Groysman,[5] R. G. Jacobsen,[5] J. A. Kadyk,[5] L. T. Kerth,[5] Yu. G. Kolomensky,[5] G. Kukartsev,[5] D. Lopes Pegna,[5] G. Lynch,[5] L. M. Mir,[5] T. J. Orimoto,[5] I. L. Osipenkov,[5] M. T. Ronan,[5,*] K. Tackmann,[5] T. Tanabe,[5] W. A. Wenzel,[5] P. del Amo Sanchez,[6] C. M. Hawkes,[6] A. T. Watson,[6] H. Koch,[7] T. Schroeder,[7] D. Walker,[8] D. J. Asgeirsson,[9] T. Cuhadar-Donszelmann,[9] B. G. Fulsom,[9] C. Hearty,[9] T. S. Mattison,[9] J. A. McKenna,[9] M. Barrett,[10] A. Khan,[10] M. Saleem,[10] L. Teodorescu,[10] V. E. Blinov,[11] A. D. Bukin,[11] V. P. Druzhinin,[11] V. B. Golubev,[11] A. P. Onuchin,[11] S. I. Serednyakov,[11] Yu. I. Skovpen,[11] E. P. Solodov,[11] K. Yu. Todyshev,[11] M. Bondioli,[12] S. Curry,[12] I. Eschrich,[12] D. Kirkby,[12] A. J. Lankford,[12] P. Lund,[12] M. Mandelkern,[12] E. C. Martin,[12] D. P. Stoker,[12] S. Abachi,[13] C. Buchanan,[13] S. D. Foulkes,[14] J. W. Gary,[14] F. Liu,[14] O. Long,[14] B. C. Shen,[14] G. M. Vitug,[14] L. Zhang,[14] H. P. Paar,[15] S. Rahatlou,[15] V. Sharma,[15] J. W. Berryhill,[16] C. Campagnari,[16] A. Cunha,[16] B. Dahmes,[16] T. M. Hong,[16] D. Kovalskyi,[16] J. D. Richman,[16] T. W. Beck,[17] A. M. Eisner,[17] C. J. Flacco,[17] C. A. Heusch,[17] J. Kroseberg,[17] W. S. Lockman,[17] T. Schalk,[17] B. A. Schumm,[17] A. Seiden,[17] M. G. Wilson,[17] L. O. Winstrom,[17] E. Chen,[18] C. H. Cheng,[18] F. Fang,[18] D. G. Hitlin,[18] I. Narsky,[18] T. Piatenko,[18] F. C. Porter,[18] R. Andreassen,[19] G. Mancinelli,[19] B. T. Meadows,[19] K. Mishra,[19] M. D. Sokoloff,[19] F. Blanc,[20] P. C. Bloom,[20] S. Chen,[20] W. T. Ford,[20] J. F. Hirschauer,[20] A. Kreisel,[20] M. Nagel,[20] U. Nauenberg,[20] A. Olivas,[20] J. G. Smith,[20] K. A. Ulmer,[20] S. R. Wagner,[20] J. Zhang,[20] A. M. Gabareen,[21] A. Soffer,[21,†] W. H. Toki,[21] R. J. Wilson,[21] F. Winklmeier,[21] D. D. Altenburg,[22] E. Feltresi,[22] A. Hauke,[22] H. Jasper,[22] J. Merkel,[22] A. Petzold,[22] B. Spaan,[22] K. Wacker,[22] V. Klose,[23] M. J. Kobel,[23] H. M. Lacker,[23] W. F. Mader,[23] R. Nogowski,[23] J. Schubert,[23] K. R. Schubert,[23] R. Schwierz,[23] J. E. Sundermann,[23] A. Volk,[23] D. Bernard,[24] G. R. Bonneaud,[24] E. Latour,[24] V. Lombardo,[24] Ch. Thiebaux,[24] M. Verderi,[24] P. J. Clark,[25] W. Gradl,[25] F. Muheim,[25] S. Playfer,[25] A. I. Robertson,[25] J. E. Watson,[25] Y. Xie,[25] M. Andreotti,[26] D. Bettoni,[26] C. Bozzi,[26] R. Calabrese,[26] A. Cecchi,[26] G. Cibinetto,[26] P. Franchini,[26] E. Luppi,[26] M. Negrini,[26] A. Petrella,[26] L. Piemontese,[26] E. Prencipe,[26] V. Santoro,[26] F. Anulli,[27] R. Baldini-Ferroli,[27] A. Calcaterra,[27] R. de Sangro,[27] G. Finocchiaro,[27] S. Pacetti,[27] P. Patteri,[27] I. M. Peruzzi,[27,‡] M. Piccolo,[27] M. Rama,[27] A. Zallo,[27] A. Buzzo,[28] R. Contri,[28] M. Lo Vetere,[28] M. M. Macri,[28] M. R. Monge,[28] S. Passaggio,[28] C. Patrignani,[28] E. Robutti,[28] A. Santroni,[28] S. Tosi,[28] K. S. Chaisanguanthum,[29] M. Morii,[29] J. Wu,[29] R. S. Dubitzky,[30] J. Marks,[30] S. Schenk,[30] U. Uwer,[30] D. J. Bard,[31] P. D. Dauncey,[31] R. L. Flack,[31] J. A. Nash,[31] W. Panduro Vazquez,[31] M. Tibbetts,[31] P. K. Behera,[32] X. Chai,[32] M. J. Charles,[32] U. Mallik,[32] J. Cochran,[33] H. B. Crawley,[33] L. Dong,[33] V. Eyges,[33] W. T. Meyer,[33] S. Prell,[33] E. I. Rosenberg,[33] A. E. Rubin,[33] Y. Y. Gao,[34] A. V. Gritsan,[34] Z. J. Guo,[34] C. K. Lae,[34] A. G. Denig,[35] M. Fritsch,[35] G. Schott,[35] N. Arnaud,[36] J. Béquilleux,[36] A. D'Orazio,[36] M. Davier,[36] G. Grosdidier,[36] A. Höcker,[36] V. Lepeltier,[36] F. Le Diberder,[36] A. M. Lutz,[36] S. Pruvot,[36] S. Rodier,[36] P. Roudeau,[36] M. H. Schune,[36] J. Serrano,[36] V. Sordini,[36] A. Stocchi,[36] W. F. Wang,[36] G. Wormser,[36] D. J. Lange,[37] D. M. Wright,[37] I. Bingham,[38] J. P. Burke,[38] C. A. Chavez,[38] J. R. Fry,[38] E. Gabathuler,[38] R. Gamet,[38] D. E. Hutchcroft,[38] D. J. Payne,[38] K. C. Schofield,[38] C. Touramanis,[38] A. J. Bevan,[39] K. A. George,[39] F. Di Lodovico,[39] R. Sacco,[39] G. Cowan,[40] H. U. Flaecher,[40] D. A. Hopkins,[40] S. Paramesvaran,[40] F. Salvatore,[40] A. C. Wren,[40] D. N. Brown,[41] C. L. Davis,[41] J. Allison,[42] D. Bailey,[42] N. R. Barlow,[42] R. J. Barlow,[42] Y. M. Chia,[42] C. L. Edgar,[42] G. D. Lafferty,[42] T. J. West,[42] J. I. Yi,[42] J. Anderson,[43] C. Chen,[43] A. Jawahery,[43] D. A. Roberts,[43] G. Simi,[43] J. M. Tuggle,[43] G. Blaylock,[44] C. Dallapiccola,[44] S. S. Hertzbach,[44] X. Li,[44] T. B. Moore,[44] E. Salvati,[44] S. Saremi,[44] R. Cowan,[45] D. Dujmic,[45] P. H. Fisher,[45] K. Koeneke,[45] G. Sciolla,[45] M. Spitznagel,[45] F. Taylor,[45] R. K. Yamamoto,[45] M. Zhao,[45] Y. Zheng,[45] S. E. Mclachlin,[46,*] P. M. Patel,[46] S. H. Robertson,[46] A. Lazzaro,[47] F. Palombo,[47] J. M. Bauer,[48] L. Cremaldi,[48] V. Eschenburg,[48] R. Godang,[48] R. Kroeger,[48] D. A. Sanders,[48] D. J. Summers,[48] H. W. Zhao,[48] S. Brunet,[49] D. Côté,[49] M. Simard,[49] P. Taras,[49] F. B. Viaud,[49] H. Nicholson,[50] G. De Nardo,[51] F. Fabozzi,[51,§] L. Lista,[51] D. Monorchio,[51] C. Sciacca,[51] M. A. Baak,[52] G. Raven,[52] H. L. Snoek,[52] C. P. Jessop,[53] K. J. Knoepfel,[53] J. M. LoSecco,[53] G. Benelli,[54] L. A. Corwin,[54] K. Honscheid,[54] H. Kagan,[54] R. Kass,[54] J. P. Morris,[54] A. M. Rahimi,[54] J. J. Regensburger,[54] S. J. Sekula,[54] Q. K. Wong,[54] N. L. Blount,[55] J. Brau,[55] R. Frey,[55] O. Igonkina,[55] J. A. Kolb,[55] M. Lu,[55] R. Rahmat,[55] N. B. Sinev,[55] D. Strom,[55] J. Strube,[55] E. Torrence,[55] N. Gagliardi,[56] A. Gaz,[56] M. Margoni,[56] M. Morandin,[56] A. Pompili,[56] M. Posocco,[56] M. Rotondo,[56] F. Simonetto,[56] R. Stroili,[56] C. Voci,[56] E. Ben-Haim,[57] H. Briand,[57] G. Calderini,[57] J. Chauveau,[57] P. David,[57] L. Del Buono,[57] Ch. de la Vaissière,[57] O. Hamon,[57] Ph. Leruste,[57] J. Malclès,[57] J. Ocariz,[57] A. Perez,[57] J. Prendki,[57] L. Gladney,[58] M. Biasini,[59] R. Covarelli,[59] E. Manoni,[59] C. Angelini,[60] G. Batignani,[60]

S. Bettarini,[60] M. Carpinelli,[60] R. Cenci,[60] A. Cervelli,[60] F. Forti,[60] M. A. Giorgi,[60] A. Lusiani,[60] G. Marchiori,[60] M. A. Mazur,[60] M. Morganti,[60] N. Neri,[60] E. Paoloni,[60] G. Rizzo,[60] J. J. Walsh,[60] J. Biesiada,[61] P. Elmer,[61] Y. P. Lau,[61] C. Lu,[61] J. Olsen,[61] A. J. S. Smith,[61] A. V. Telnov,[61] E. Baracchini,[62] F. Bellini,[62] G. Cavoto,[62] D. del Re,[62] E. Di Marco,[62] R. Faccini,[62] F. Ferrarotto,[62] F. Ferroni,[62] M. Gaspero,[62] P. D. Jackson,[62] L. Li Gioi,[62] M. A. Mazzoni,[62] S. Morganti,[62] G. Piredda,[62] F. Polci,[62] F. Renga,[62] C. Voena,[62] M. Ebert,[63] T. Hartmann,[63] H. Schröder,[63] R. Waldi,[63] T. Adye,[64] G. Castelli,[64] B. Franek,[64] E. O. Olaiya,[64] W. Roethel,[64] F. F. Wilson,[64] S. Emery,[65] M. Escalier,[65] A. Gaidot,[65] S. F. Ganzhur,[65] G. Hamel de Monchenault,[65] W. Kozanecki,[65] G. Vasseur,[65] Ch. Yèche,[65] M. Zito,[65] X. R. Chen,[66] H. Liu,[66] W. Park,[66] M. V. Purohit,[66] R. M. White,[66] J. R. Wilson,[66] M. T. Allen,[67] D. Aston,[67] R. Bartoldus,[67] P. Bechtle,[67] R. Claus,[67] J. P. Coleman,[67] M. R. Convery,[67] J. C. Dingfelder,[67] J. Dorfan,[67] G. P. Dubois-Felsmann,[67] W. Dunwoodie,[67] R. C. Field,[67] T. Glanzman,[67] S. J. Gowdy,[67] M. T. Graham,[67] P. Grenier,[67] C. Hast,[67] W. R. Innes,[67] J. Kaminski,[67] M. H. Kelsey,[67] H. Kim,[67] P. Kim,[67] M. L. Kocian,[67] D. W. G. S. Leith,[67] S. Li,[67] S. Luitz,[67] V. Luth,[67] H. L. Lynch,[67] D. B. MacFarlane,[67] H. Marsiske,[67] R. Messner,[67] D. R. Muller,[67] C. P. O'Grady,[67] I. Ofte,[67] A. Perazzo,[67] M. Perl,[67] T. Pulliam,[67] B. N. Ratcliff,[67] A. Roodman,[67] A. A. Salnikov,[67] R. H. Schindler,[67] J. Schwiening,[67] A. Snyder,[67] D. Su,[67] M. K. Sullivan,[67] K. Suzuki,[67] S. K. Swain,[67] J. M. Thompson,[67] J. Va'vra,[67] A. P. Wagner,[67] M. Weaver,[67] W. J. Wisniewski,[67] M. Wittgen,[67] D. H. Wright,[67] A. K. Yarritu,[67] K. Yi,[67] C. C. Young,[67] V. Ziegler,[67] P. R. Burchat,[68] A. J. Edwards,[68] S. A. Majewski,[68] T. S. Miyashita,[68] B. A. Petersen,[68] L. Wilden,[68] S. Ahmed,[69] M. S. Alam,[69] R. Bula,[69] J. A. Ernst,[69] V. Jain,[69] B. Pan,[69] M. A. Saeed,[69] F. R. Wappler,[69] S. B. Zain,[69] M. Krishnamurthy,[70] S. M. Spanier,[70] R. Eckmann,[71] J. L. Ritchie,[71] A. M. Ruland,[71] C. J. Schilling,[71] R. F. Schwitters,[71] J. M. Izen,[72] X. C. Lou,[72] S. Ye,[72] F. Bianchi,[73] F. Gallo,[73] D. Gamba,[73] M. Pelliccioni,[73] M. Bomben,[74] L. Bosisio,[74] C. Cartaro,[74] F. Cossutti,[74] G. Della Ricca,[74] L. Lanceri,[74] L. Vitale,[74] V. Azzolini,[75] N. Lopez-March,[75] F. Martinez-Vidal,[75,‖] D. A. Milanes,[75] A. Oyanguren,[75] J. Albert,[76] Sw. Banerjee,[76] B. Bhuyan,[76] K. Hamano,[76] R. Kowalewski,[76] I. M. Nugent,[76] J. M. Roney,[76] R. J. Sobie,[76] P. F. Harrison,[77] J. Ilic,[77] T. E. Latham,[77] G. B. Mohanty,[77] H. R. Band,[78] X. Chen,[78] S. Dasu,[78] K. T. Flood,[78] J. J. Hollar,[78] P. E. Kutter,[78] Y. Pan,[78] M. Pierini,[78] R. Prepost,[78] S. L. Wu,[78] and H. Neal[79]

(*BABAR* Collaboration)

[1]*Laboratoire de Physique des Particules, IN2P3/CNRS et Université de Savoie, F-74941 Annecy-Le-Vieux, France*
[2]*Facultat de Fisica, Departament ECM, Universitat de Barcelona, E-08028 Barcelona, Spain*
[3]*Dipartimento di Fisica, Università di Bari and INFN, I-70126 Bari, Italy*
[4]*Institute of Physics, University of Bergen, N-5007 Bergen, Norway*
[5]*Lawrence Berkeley National Laboratory and University of California, Berkeley, California 94720, USA*
[6]*University of Birmingham, Birmingham, B15 2TT, United Kingdom*
[7]*Institut für Experimentalphysik 1, Ruhr Universität Bochum, D-44780 Bochum, Germany*
[8]*University of Bristol, Bristol BS8 1TL, United Kingdom*
[9]*University of British Columbia, Vancouver, British Columbia, Canada V6T 1Z1*
[10]*Brunel University, Uxbridge, Middlesex UB8 3PH, United Kingdom*
[11]*Budker Institute of Nuclear Physics, Novosibirsk 630090, Russia*
[12]*University of California at Irvine, Irvine, California 92697, USA*
[13]*University of California at Los Angeles, Los Angeles, California 90024, USA*
[14]*University of California at Riverside, Riverside, California 92521, USA*
[15]*University of California at San Diego, La Jolla, California 92093, USA*
[16]*University of California at Santa Barbara, Santa Barbara, California 93106, USA*
[17]*Institute for Particle Physics, University of California at Santa Cruz, Santa Cruz, California 95064, USA*
[18]*California Institute of Technology, Pasadena, California 91125, USA*
[19]*University of Cincinnati, Cincinnati, Ohio 45221, USA*
[20]*University of Colorado, Boulder, Colorado 80309, USA*
[21]*Colorado State University, Fort Collins, Colorado 80523, USA*
[22]*Institut für Physik, Universität Dortmund, D-44221 Dortmund, Germany*
[23]*Institut für Kern- und Teilchenphysik, Technische Universität Dresden, D-01062 Dresden, Germany*
[24]*Laboratoire Leprince-Ringuet, CNRS/IN2P3, Ecole Polytechnique, F-91128 Palaiseau, France*
[25]*University of Edinburgh, Edinburgh EH9 3JZ, United Kingdom*
[26]*Dipartimento di Fisica, Università di Ferrara and INFN, I-44100 Ferrara, Italy*
[27]*Laboratori Nazionali di Frascati dell'INFN, I-00044 Frascati, Italy*
[28]*Dipartimento di Fisica, Università di Genova and INFN, I-16146 Genova, Italy*
[29]*Harvard University, Cambridge, Massachusetts 02138, USA*
[30]*Physikalisches Institut, Philosophenweg 12, Universität Heidelberg, D-69120 Heidelberg, Germany*

[31]*Imperial College London, London, SW7 2AZ, United Kingdom*
[32]*University of Iowa, Iowa City, Iowa 52242, USA*
[33]*Iowa State University, Ames, Iowa 50011-3160, USA*
[34]*Johns Hopkins University, Baltimore, Maryland 21218, USA*
[35]*Institut für Experimentelle Kernphysik, Universität Karlsruhe, D-76021 Karlsruhe, Germany*
[36]*Laboratoire de l'Accélérateur Linéaire, Centre Scientifique d'Orsay, IN2P3/CNRS et Université Paris-Sud 11, B.P. 34, F-91898 ORSAY Cedex, France*
[37]*Lawrence Livermore National Laboratory, Livermore, California 94550, USA*
[38]*University of Liverpool, Liverpool L69 7ZE, United Kingdom*
[39]*Queen Mary, University of London, E1 4NS, United Kingdom*
[40]*Royal Holloway and Bedford New College, University of London, Egham, Surrey TW20 0EX, United Kingdom*
[41]*University of Louisville, Louisville, Kentucky 40292, USA*
[42]*University of Manchester, Manchester M13 9PL, United Kingdom*
[43]*University of Maryland, College Park, Maryland 20742, USA*
[44]*University of Massachusetts, Amherst, Massachusetts 01003, USA*
[45]*Laboratory for Nuclear Science, Massachusetts Institute of Technology, Cambridge, Massachusetts 02139, USA*
[46]*McGill University, Montréal, Québec, Canada H3A 2T8*
[47]*Dipartimento di Fisica, Università di Milano and INFN, I-20133 Milano, Italy*
[48]*University of Mississippi, University, Mississippi 38677, USA*
[49]*Université de Montréal, Physique des Particules, Montréal, Québec, Canada H3C 3J7*
[50]*Mount Holyoke College, South Hadley, Massachusetts 01075, USA*
[51]*Dipartimento di Scienze Fisiche, Università di Napoli Federico II and INFN, I-80126, Napoli, Italy*
[52]*NIKHEF, National Institute for Nuclear Physics and High Energy Physics, NL-1009 DB Amsterdam, The Netherlands*
[53]*University of Notre Dame, Notre Dame, Indiana 46556, USA*
[54]*The Ohio State University, Columbus, Ohio 43210, USA*
[55]*University of Oregon, Eugene, Oregon 97403, USA*
[56]*Dipartimento di Fisica, Università di Padova and INFN, I-35131 Padova, Italy*
[57]*Laboratoire de Physique Nucléaire et de Hautes Energies, IN2P3/CNRS, Université Pierre et Marie Curie-Paris6, Université Denis Diderot-Paris7, F-75252 Paris, France*
[58]*University of Pennsylvania, Philadelphia, Pennsylvania 19104, USA*
[59]*Dipartimento di Fisica, Università di Perugia and INFN, I-06100 Perugia, Italy*
[60]*Dipartimento di Fisica, Scuola Normale Superiore, Università di Pisa and INFN, I-56127 Pisa, Italy*
[61]*Princeton University, Princeton, New Jersey 08544, USA*
[62]*Dipartimento di Fisica, Università di Roma La Sapienza and INFN, I-00185 Roma, Italy*
[63]*Universität Rostock, D-18051 Rostock, Germany*
[64]*Rutherford Appleton Laboratory, Chilton, Didcot, Oxon, OX11 0QX, United Kingdom*
[65]*DSM/Dapnia, CEA/Saclay, F-91191 Gif-sur-Yvette, France*
[66]*University of South Carolina, Columbia, South Carolina 29208, USA*
[67]*Stanford Linear Accelerator Center, Stanford, California 94309, USA*
[68]*Stanford University, Stanford, California 94305-4060, USA*
[69]*State University of New York, Albany, New York 12222, USA*
[70]*University of Tennessee, Knoxville, Tennessee 37996, USA*
[71]*University of Texas at Austin, Austin, Texas 78712, USA*
[72]*University of Texas at Dallas, Richardson, Texas 75083, USA*
[73]*Dipartimento di Fisica Sperimentale, Università di Torino and INFN, I-10125 Torino, Italy*
[74]*Dipartimento di Fisica, Università di Trieste and INFN, I-34127 Trieste, Italy*
[75]*IFIC, Universitat de Valencia-CSIC, E-46071 Valencia, Spain*
[76]*University of Victoria, Victoria, British Columbia, Canada V8W 3P6*
[77]*Department of Physics, University of Warwick, Coventry CV4 7AL, United Kingdom*
[78]*University of Wisconsin, Madison, Wisconsin 53706, USA*
[79]*Yale University, New Haven, Connecticut 06511, USA*
(Received 21 August 2007; published 20 November 2007)

[*]Deceased.
[†]Current address: Tel Aviv University, Tel Aviv, 69978, Israel.
[‡]Also at: Dipartimento di Fisica, Università di Perugia, Perugia, Italy.
[§]Also at: Università della Basilicata, Potenza, Italy.
[‖]Also at: Facultat de Fisica, Departament ECM, Universitat de Barcelona, E-08028 Barcelona, Spain.

We study the processes $e^+e^- \to 2(\pi^+\pi^-)\pi^0\gamma$, $2(\pi^+\pi^-)\eta\gamma$, $K^+K^-\pi^+\pi^-\pi^0\gamma$ and $K^+K^-\pi^+\pi^-\eta\gamma$ with the hard photon radiated from the initial state. About 20 000, 4300, 5500, and 375 fully reconstructed events, respectively, are selected from 232 fb^{-1} of *BABAR* data. The invariant mass of the hadronic final state defines the effective e^+e^- center-of-mass energy, so that the obtained cross sections from the threshold to about 5 GeV can be compared with corresponding direct e^+e^- measurements, currently available only for the $\eta\pi^+\pi^-$ and $\omega\pi^+\pi^-$ submodes of the $e^+e^- \to 2(\pi^+\pi^-)\pi^0$ channel. Studying the structure of these events, we find contributions from a number of intermediate states, and we extract their cross sections where possible. In particular, we isolate the contribution from $e^+e^- \to \omega(782)\pi^+\pi^-$ and study the $\omega(1420)$ and $\omega(1650)$ resonances. In the charmonium region, we observe the J/ψ in all these final states and several intermediate states, as well as the $\psi(2S)$ in some modes, and we measure the corresponding branching fractions.

DOI: 10.1103/PhysRevD.76.092005 PACS numbers: 13.66.Bc, 13.25.Gv, 13.25.Jx, 14.40.Cs

I. INTRODUCTION

Electron-positron annihilation at fixed center-of-mass (c.m.) energies has long been a mainstay of research in elementary particle physics. The idea of utilizing initial-state radiation (ISR) to study e^+e^- reactions below the nominal c.m. energies was outlined in Ref. [1], and discussed in the context of high-luminosity ϕ and B factories in Refs. [2–4]. At high energies, e^+e^- annihilation is dominated by quark-level processes producing two or more hadronic jets. However, low-multiplicity processes dominate at energies below about 2 GeV, and the region near charm threshold, 3.0–4.5 GeV, features a number of resonances [5]. The ISR processes allow us to probe a wealth of physics parameters, including cross sections, spectroscopy, and form factors.

Of particular current interest are several recently observed charmonium states and a possible discrepancy between the measured value of the anomalous magnetic moment of the muon $(g-2)_\mu$ and that predicted by the standard model [6]. Charmonium and other states with $J^{PC} = 1^{--}$ can be observed as resonances in the cross section, and intermediate states may be present in the hadronic system. Measurement of the decay modes and their branching fractions is important in understanding the nature of these states. The prediction for $(g-2)_\mu$ is based on hadronic-loop corrections measured from low-energy $e^+e^- \to$ hadrons data, and these dominate the uncertainty on the prediction. Improving this prediction requires not only more precise measurements, but also measurements over the entire energy range and inclusion of all the important subprocesses in order to understand possible acceptance effects. ISR events at B factories provide independent measurements of hadronic cross sections with complete coverage from the production threshold to about 5 GeV.

The cross section for the radiation of a photon of energy E_γ followed by the production of a particular hadronic final state f is related to the corresponding direct $e^+e^- \to f$ cross section $\sigma_f(s)$ by

$$\frac{d\sigma_{\gamma f}(s,x)}{dx} = W(s,x)\cdot\sigma_f(s(1-x)), \qquad (1)$$

where $\sqrt{s}$ is the initial e^+e^- c.m. energy, $x = 2E_\gamma/\sqrt{s}$ is the fractional energy of the ISR photon, and $E_{\rm c.m.} \equiv \sqrt{s(1-x)}$ is the effective c.m. energy at which the final state f is produced. The probability density function $W(s,x)$ for ISR photon emission has been calculated with better than 1% precision (see e.g. Ref. [4]). It falls rapidly as E_γ increases from zero, but has a long tail, which combines with the increasing $\sigma_f(s(1-x))$ to produce a sizable cross section at very low $E_{\rm c.m.}$. The angular distribution of the ISR photon peaks along the beam directions, but 10%–15% [4] of the photons are within a typical detector acceptance.

Experimentally, the measured invariant mass of the hadronic final state defines $E_{\rm c.m.}$ with better accuracy than measured photon energy. An important feature of ISR data is that a wide range of energies is scanned simultaneously in one experiment, so that no structure is missed and the relative normalization uncertainties in data from different experiments or accelerator parameters are avoided. Furthermore, for large values of x the hadronic system is collimated, reducing acceptance issues and allowing measurements at energies down to production threshold. The mass resolution is not as good as a typical beam energy spread used in direct measurements, but the resolution and absolute energy scale can be monitored by the width and mass of well-known resonances, such as the J/ψ produced in the reaction $e^+e^- \to J/\psi\gamma$. Backgrounds from $e^+e^- \to$ hadrons events at the nominal $\sqrt{s}$ and from other ISR processes can be suppressed by a combination of particle identification and kinematic fitting techniques. Studies of $e^+e^- \to \mu^+\mu^-\gamma$ and several multihadron ISR processes using *BABAR* data have been reported [7–11], demonstrating the viability of such measurements.

The contributions to the $2(\pi^+\pi^-)\pi^0$ final state from the $\eta\pi^+\pi^-$ and $\omega\pi^+\pi^-$ channels have been measured directly by the DM1 [12], DM2 [13,14], CMD2 [15], and ND [16] collaborations for $\sqrt{s} < 2.2$ GeV. In this paper we present a comprehensive study of the $2(\pi^+\pi^-)\pi^0$ final state along with new measurements of the $2(\pi^+\pi^-)\eta$, $K^+K^-\pi^+\pi^-\pi^0$ and $K^+K^-\pi^+\pi^-\eta$ final states. In all cases we require detection of the ISR photon and perform

a set of kinematic fits. We are able to suppress backgrounds sufficiently to study these final states from their respective production thresholds up to 4.5 GeV. In addition to measuring the overall cross sections, we study the internal structure of the events and measure cross sections for a number of intermediate states. We study the charmonium region, measuring several J/ψ and $\psi(2S)$ branching fractions.

II. *BABAR* DETECTOR AND DATA SET

The data used in this analysis were collected with the *BABAR* detector at the PEP-II asymmetric energy e^+e^- storage rings. The total integrated luminosity used is 232 fb^{-1}, which includes 211 fb^{-1} collected at the $\Upsilon(4S)$ peak, $\sqrt{s} = 10.58$ GeV, and 21 fb^{-1} collected below the resonance, at $\sqrt{s} = 10.54$ GeV.

The *BABAR* detector is described elsewhere [17]. Here we use charged particles reconstructed in the tracking system, which comprised the five-layer silicon vertex tracker (SVT) and the 40-layer drift chamber (DCH) in a 1.5 T axial magnetic field. Separation of charged pions, kaons, and protons uses a combination of Cherenkov angles measured in the detector of internally reflected Cherenkov light (DIRC) and specific ionization measured in the SVT and DCH. Here we use a kaon identification algorithm that provides 90%–95% efficiency, depending on momentum, and rejects pions and protons by factors of 20–100. Photon and electron energies are measured in the CsI(Tl) electromagnetic calorimeter (EMC).

To study the detector acceptance and efficiency, we use a simulation package developed for radiative processes. The simulation of signal and background hadronic final states is based on the approach suggested by Czyż and Kühn [18]. Multiple soft-photon emission from the initial-state charged particles is implemented with a structure-function technique [19,20], and photon radiation from the final-state particles is simulated by the PHOTOS package [21]. The accuracy of the radiative corrections is about 1%.

We simulate the $2(\pi^+\pi^-)\pi^0$ final state both according to phase space and with models that include the $\eta\rho$, $\omega\pi^+\pi^-$ and $\omega f_0(980)$ intermediate states, and the $K^+K^-\pi^+\pi^-\pi^0$ final state both according to phase space and including the intermediate ϕ and/or η resonances. The generated events go through a detailed detector simulation [22], and we reconstruct them with the same software chain as the experimental data. Variations in detector and background conditions are taken into account.

We generate a large number of background processes, including the ISR channels $e^+e^- \to \pi^+\pi^-\pi^+\pi^-\gamma$, $K^+K^-\pi^+\pi^-\gamma$, $2(\pi^+\pi^-)\pi^0\pi^0\gamma$, and $K^+K^-\pi^+\pi^-\pi^0\pi^0\gamma$. These can contribute due to a combination of particle misidentification, and missing or spurious tracks or photons. In addition, we study the non-ISR backgrounds $e^+e^- \to q\bar{q}$ $(q = u, d, s, c)$ generated by JETSET [23] and $e^+e^- \to \tau^+\tau^-$ by KORALB [24]. The contribution from the $\Upsilon(4S)$ decays is negligible. The cross sections for these processes are known with about 10% accuracy or better, which is sufficient for these measurements.

III. EVENT SELECTION AND KINEMATIC FIT

In the initial selection of candidate events, we consider photon candidates in the EMC with energy above 0.03 GeV and charged tracks reconstructed in the DCH or SVT or both that extrapolate within 0.25 cm of the beam axis and within 3 cm of the nominal collision point along the axis. We require a high-energy photon in the event with an energy in the initial e^+e^- c.m. frame of $E_\gamma > 3$ GeV, and exactly four charged tracks with zero net charge that combine with a pair of other photons to roughly balance the momentum of the highest-energy photon. We fit a vertex to the set of charged tracks and use it as the point of origin to calculate the photon directions. Most events contain additional soft photons due to machine background or interactions in the detector material.

We subject each of these candidate events to a set of constrained kinematic fits, and use the fit results, along with charged-particle identification, both to select the final states of interest and to measure backgrounds from other processes. We assume the photon with the highest E_γ is the ISR photon, and the kinematic fits use its direction and energy along with the four-momenta and covariance matrices of the initial e^+e^- and the set of selected tracks and photons. The fitted three-momenta for each charged track and photon are used in further kinematical calculations.

We pair all non-ISR photon candidates and consider combinations with invariant mass within ± 30 MeV$/c^2$ of the $\pi^0(\eta)$ mass as $\pi^0(\eta)$ candidates. For each candidate event, we perform a kinematic fit using the momenta of the ISR photon, of the two additional photons and of the four tracks (under the relevant mass hypotheses for each considered final state), imposing five constraints (5C): the two-photon invariant mass must match the nominal π^0 or η mass, and the energy and momentum of the whole event must match the energy and momentum of the initial e^+e^- state. We retain the combination with the lowest χ^2, either $\chi^2_{4\pi\pi^0}$ or $\chi^2_{4\pi\eta}$, as a $2(\pi^+\pi^-)\pi^0$ or $2(\pi^+\pi^-)\eta$ candidate, respectively. If the four tracks include two identified kaons with zero net charge, we perform a set of similar fits under the hypotheses and retain the two-photon combination with the lowest $\chi^2_{2K2\pi\pi^0/\eta}$. If only one track identified as a kaon, we test two possible combinations under the $K^+K^-\pi^+\pi^-\pi^0$ and $K^+K^-\pi^+\pi^-\eta$ hypotheses and also retain the lowest $\chi^2_{2K2\pi\pi^0/\eta}$. In case of one identified kaon to reduce the large background from ISR $2(\pi^+\pi^-)$ events [9] with no additional neutral hadrons, we also fit each candidate event under the $2(\pi^+\pi^-)$ hypothesis and require $\chi^2_{4\pi} > 20$.

IV. $2(\pi^+\pi^-)\pi^0$ FINAL STATE

A. Final selection and backgrounds

To suppress $K^+K^-\pi^+\pi^-\pi^0$ background, we require that no more than one track in the event is identified as a kaon, and require $\chi^2_{2K2\pi\pi^0} > 30$. To reject any $K^\pm K^0_S \pi^\mp \pi^0$ background, we require all tracks to extrapolate within 2.5 mm of the beam axis. The result of the 5C fit for the remaining events under the $2(\pi^+\pi^-)\pi^0\gamma$ hypothesis with the $2(\pi^+\pi^-)\pi^0$ invariant mass up to 4.5 GeV/c^2 is used for the final event selection and background estimate. We consider two types of background: a non-ISR-type background and an ISR-type background.

The non-ISR-type background comes from the $e^+e^- \to q\bar{q}$ events and we estimate it using the JETSET simulation. It is dominated by events with a hard π^0 producing a fake ISR photon, and the similar kinematics causes it to peak at low values of $\chi^2_{4\pi\pi^0}$. We evaluate this background in a number of $E_{\rm c.m.}$ ranges by combining the ISR photon candidate with another photon candidate in both data and simulated events, and comparing the π^0 signals in the resulting $\gamma\gamma$ invariant mass distributions. The simulation gives an $E_{\rm c.m.}$ dependence consistent with the data, so we normalize it by an overall factor. The hatched histogram in Fig. 1 represents this background and we subtract it from the experimental distribution.

The $\chi^2_{4\pi\pi^0}$ distribution for the remaining events is shown in Fig. 1 as points, and the open histogram is the distribution for the simulated $2(\pi^+\pi^-)\pi^0$ events. The simulated distribution is normalized to the data in the region $\chi^2_{4\pi\pi^0} < 10$ where the backgrounds and radiative corrections are smallest. The experimental distribution has contributions from ISR-type background processes, but the simulated distribution is also broader than the expected 5C χ^2 distribution. This is due to multiple soft-photon emission from the initial state and radiation from the final-state charged particles, which are not taken into account by the fit. The shape of the χ^2 distribution at high values was studied in detail [9,10] using ISR processes for which very clean samples can be obtained without any limit on the χ^2 value and Monte Carlo (MC) signal events have been found to accurately simulate it.

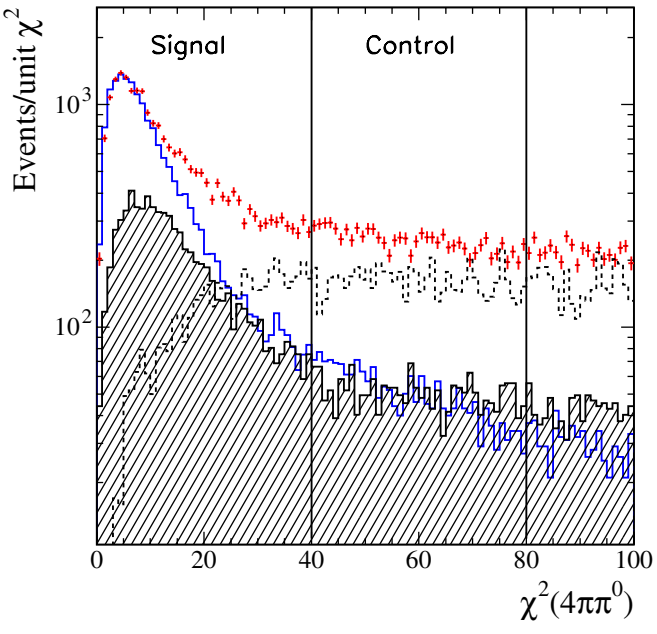

FIG. 1 (color online). Distribution of χ^2 from the five-constraint fit for $2(\pi^+\pi^-)\pi^0$ candidates in the data (points) after subtracting the $e^+e^- \to q\bar{q}$ background (hatched histogram). The open histogram is the distribution for simulated signal events, normalized as described in the text. The dashed histogram is the estimated backgrounds from other ISR channels, as described in the text.

All ISR-type background sources are consistent with having a $\chi^2_{4\pi\pi^0}$ distribution that is nearly uniform over the range shown in Fig. 1. As an example, the $\chi^2_{4\pi\pi^0}$ distribution predicted from our simulations of other ISR channels (see Sec. II) is shown as the dashed histogram, with the main contribution from the $2(\pi^+\pi^-)\pi^0\pi^0\gamma$ process [10]. We therefore determine the $\chi^2_{4\pi\pi^0}$ distribution of the ISR-type background ($\chi^2_{\rm ISR\ bkg}$) from the data distribution, by subtracting the $\chi^2_{4\pi\pi^0}$ distributions of simulated signal and of the $q\bar{q}$ backgrounds, both of which are normalized to data as mentioned above. The obtained $\chi^2_{\rm ISR\ bkg}$ distribution is in agreement with simulation in shape, but contains events from the processes which are not included into simulation.

In order to determine the mass spectrum of the genuine $2(\pi^+\pi^-)\pi^0$ events, we define signal ($\chi^2_{4\pi\pi^0} < 40$) and control ($40 < \chi^2_{4\pi\pi^0} < 80$) regions as shown in Fig. 1. The signal region of Fig. 1 contains 30 776 data and 17 477 simulated signal events, and the control region contains 11 829 data and 2012 simulated events. For each mass bin, the number of signal events is obtained by subtracting the $q\bar{q}$-background events first. The contribution of the ISR-background events in the χ^2-signal region are obtained using the data-MC difference in number of events in the χ^2-control region normalized according to the shape of simulated $\chi^2_{\rm ISR\ bkg}$ distribution. The $q\bar{q}$ subtraction is actually performed using a smooth function fitted to the simulated mass distribution.

Figure 2 shows the $2(\pi^+\pi^-)\pi^0$ invariant-mass distribution from threshold up to 4.5 GeV/c^2 for the experimental events in the signal region of Fig. 1. Narrow peaks are apparent at the J/ψ and $\psi(2S)$ masses. The hatched histogram represents the $q\bar{q}$ background, which is negligible at low mass but becomes large at higher masses. The open histogram represents the sum of all backgrounds, including those estimated from the control region. They total about 20% at low mass but account for 60%–80% of the observed data near 4 GeV/c^2.

Considering uncertainties in the cross sections for the background processes, the normalization of events in the

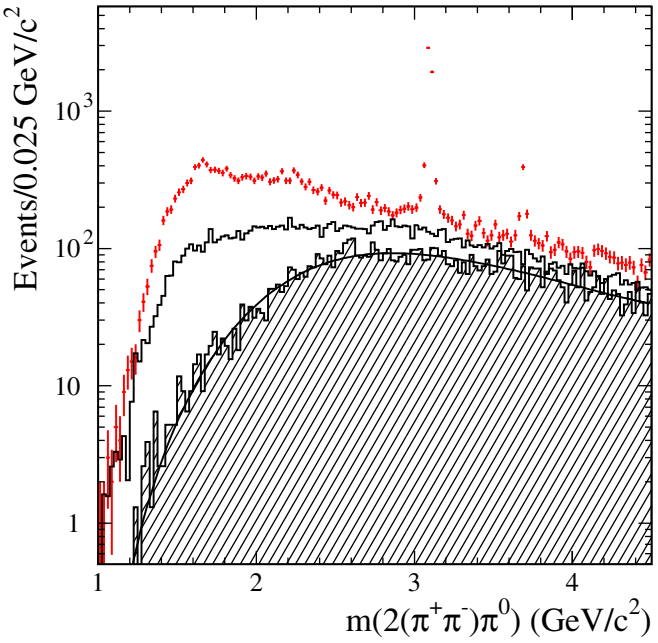

FIG. 2 (color online). Invariant mass distribution for selected $2(\pi^+\pi^-)\pi^0$ events in the data (points). The hatched and open histograms represent the non-ISR background and sum of all backgrounds, respectively. The smooth line approximates the non-ISR background, as described in the text.

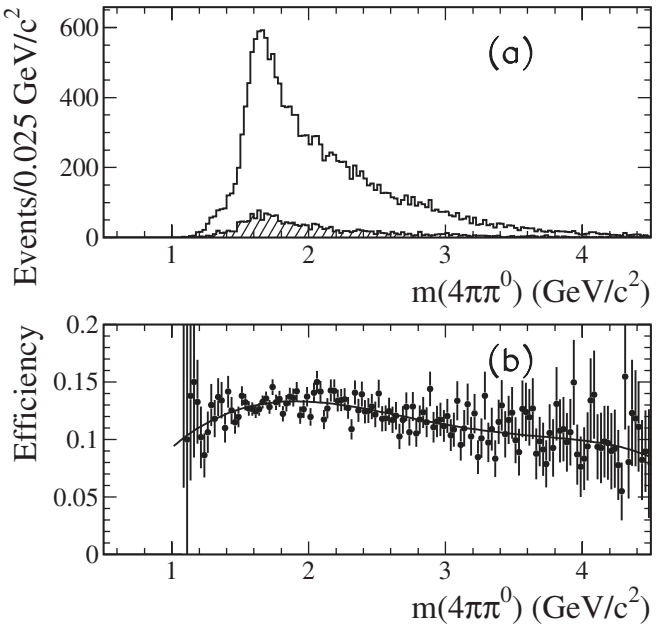

FIG. 3. (a) Invariant mass distributions for simulated $2(\pi^+\pi^-)\pi^0$ events in the phase space model, reconstructed in the signal (open) and control (hatched) regions of Fig. 1. (b) Net reconstruction and selection efficiency as a function of mass obtained from this simulation. The curve represents a 3rd order polynomial fit.

control region and the simulation statistics, we estimate a systematic uncertainty on the signal yield that is about 5% in the 1.5–1.8 GeV/c^2 mass region, but increases to 20% at 2.5 GeV/c^2 and to more than 50% in the region above 3.5 GeV/c^2.

B. Selection efficiency

The selection procedures applied to the data are also applied to the simulated signal samples. The resulting $2(\pi^+\pi^-)\pi^0$ invariant-mass distributions in the signal and control regions of Fig. 1 are shown in Fig. 3(a) for the phase space simulation. The fraction of simulated events in the $\chi^2_{4\pi\pi^0}$ control region remains constant over mass, supporting the assumption of mass-independent χ^2 shape. The broad, smooth mass distribution is chosen to facilitate the estimation of the efficiency as a function of mass, and this model reproduces the observed distributions of pion momenta and polar angles. We divide the number of reconstructed simulated events in each 25 MeV/c^2 mass interval by the number generated in that interval to obtain the efficiency shown as the points in Fig. 3(b); the curve represents a 3rd order polynomial fit to the points. We simulate events with the ISR photon confined to the angular range of EMC acceptance. The computed efficiency is for this fiducial region, but includes the acceptance for the final-state hadrons, the inefficiencies of the detector subsystems, and event loss due to additional soft-photon emission.

The simulations including the $\omega\pi^+\pi^-$ and/or $\eta\pi^+\pi^-$ channels have very different distributions of mass and angles in the $2(\pi^+\pi^-)\pi^0$ rest frame. However, the angular acceptance is quite uniform for ISR events, and the efficiencies are consistent with those from the phase space simulation within 3%.

We study the shape of the $\chi^2_{4\pi\pi^0}$ distribution using events in the large J/ψ peak. By comparing J/ψ yields in data and simulation for $\chi^2_{4\pi\pi^0} < 40$ and $\chi^2_{4\pi\pi^0} < 200$, we limit any mismodeling of the efficiency to 3%. We correct the track-finding efficiency following the procedures described in Ref. [9], with a much larger sample of $2(\pi^+\pi^-)$ events. We consider data and simulated events that contain a high-energy photon plus exactly three charged tracks and satisfy a set of kinematic criteria, including a good χ^2 from a kinematic fit under the hypothesis that there is exactly one missing track in the event. We find that the simulated track-finding efficiency is overestimated by $(0.8 \pm 0.5)\%$ per track, so we apply a correction of $+(3 \pm 2)\%$ to the signal yield. We correct the π^0-finding efficiency using the procedure described in detail in Ref. [10]. From ISR $e^+e^- \to \omega\pi^0\gamma \to \pi^+\pi^-\pi^0\pi^0\gamma$ events selected with and without the π^0 from the ω decay, we find an excess of simulated efficiency for one π^0 of $(3 \pm 2)\%$.

C. Cross section for $e^+e^- \to 2(\pi^+\pi^-)\pi^0$

We calculate the cross section as a function of effective c.m. energy for the reaction $e^+e^- \to 2(\pi^+\pi^-)\pi^0$ from

$$\sigma_{2(\pi^+\pi^-)\pi^0}(E_{\rm c.m.}) = \frac{dN_{2(\pi^+\pi^-)\pi^0\gamma}(E_{\rm c.m.})}{d\mathcal{L}(E_{\rm c.m.}) \cdot \epsilon_{2(\pi^+\pi^-)\pi^0}(E_{\rm c.m.})}, \quad (2)$$

where $E_{\rm c.m.} \equiv m_{2(\pi^+\pi^-)\pi^0}c^2$, $m_{2(\pi^+\pi^-)\pi^0}$ is the measured invariant mass of the $2(\pi^+\pi^-)\pi^0$ system, $dN_{2(\pi^+\pi^-)\pi^0\gamma}$ is the number of selected events after background subtraction in the interval $dE_{\rm c.m.}$, and $\epsilon_{2(\pi^+\pi^-)\pi^0}(E_{\rm c.m.})$ is the corrected detection efficiency. We calculate the differential luminosity, $d\mathcal{L}(E_{\rm c.m.})$, in each interval $dE_{\rm c.m.}$ using integrated *BABAR* luminosity and the probability density function from Eq. (1). We compare the experimental dimuon mass spectrum from ISR $\mu^+\mu^-\gamma$ events, selected with the help of the instrumented flux return (IFR), with the calculated one [9] and conservatively estimate a systematic uncertainty on $d\mathcal{L}$ of 3%. This $d\mathcal{L}$ has been corrected for vacuum polarization (VP), so the obtained cross section includes contribution from VP which should be excluded when using these data in calculations of $(g-2)_\mu$ [6]. The initial- and part of the final-state soft-photon emissions are canceled out in the ratio.

We show the cross section as a function of energy in Fig. 4, with statistical errors only, and provide a list of our results in Table I. There is no direct e^+e^- measurement of inclusive $2(\pi^+\pi^-)\pi^0$ final state for a comparison. The applied corrections and systematic uncertainties are summarized in Table II.

The cross section rises from threshold to a peak value of about 4.0 nb near 1.65 GeV, then generally decreases with increasing energy except for prominent peaks at the J/ψ and $\psi(2S)$ masses. Gaussian fits to the simulated line shapes give a resolution on the measured $2(\pi^+\pi^-)\pi^0$ mass that varies between 6.8 MeV/c^2 in the 1.5–2.5 GeV/c^2 region and 8.8 MeV/c^2 in the 2.5–3.5 GeV/c^2 region. The resolution function is not purely Gaussian due to soft-photon radiation, but less than 20% of the signal is outside the 25 MeV/c^2 mass bin. Since the cross section has no sharp structure other than the J/ψ and $\psi(2S)$ peaks discussed in Sec. VIII below, we apply no correction for the resolution.

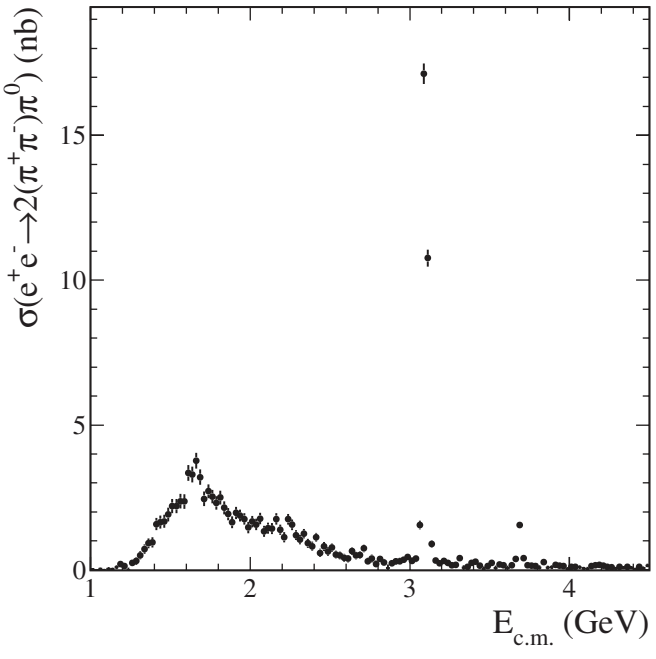

FIG. 4. The $e^+e^- \to 2(\pi^+\pi^-)\pi^0$ cross section as a function of e^+e^- c.m. energy measured with ISR data. Only statistical errors are shown.

D. Substructure in the $2(\pi^+\pi^-)\pi^0$ final state

The $2(\pi^+\pi^-)\pi^0$ final state has a rich internal structure. Figure 5(a) shows a scatter plot of the smallest $\pi^+\pi^-\pi^0$ mass in each candidate event versus the five-pion mass. There are horizontal bands corresponding to the $\eta\pi^+\pi^-$ and $\omega\pi^+\pi^-$ channels as well as vertical bands from the J/ψ and $\psi(2S)$. Figure 5(b) shows the full $\pi^+\pi^-\pi^0$ mass distribution (four entries per event) for selected events as the open histogram and for the estimated non-ISR background as the crosshatched histogram. There is also a small signal for the $\phi\pi^+\pi^-$ channel, and a peak at the J/ψ mass, which is due to the $\psi(2S) \to J/\psi\pi^+\pi^-, J/\psi \to \pi^+\pi^-\pi^0$ decay chain.

Figure 6(a) shows a scatter plot of all four $m_{\pi^+\pi^-}$ vs $m_{\pi^+\pi^-\pi^0}$ combinations in each event. There is a horizontal band corresponding to the $\rho^0(770)$ and an enhancement where it crosses the vertical η band. A $\rho^\pm(770)$ band is similarly visible in Fig. 6(b), a scatter plot of all four $m_{\pi^\pm\pi^0}$ vs $m_{\pi^+\pi^-\pi^\pm}$ combinations in each event. There is a suggestion of structure along these bands and in Fig. 5(b) around 1.2–1.3 GeV/c^2, which could correspond to the $a_1(1260)$, $\pi(1300)$ or $a_2(1320)$ resonances. We now study events containing an η, ω, or ρ in detail.

E. $\eta\pi^+\pi^-$ and $\eta\rho$ intermediate states

To extract the contribution from the $\eta\pi^+\pi^-$ intermediate state we select the $\pi^+\pi^-\pi^0$ combination in each event (from four possible combinations) with mass closest to the η mass. Figure 7 shows the distribution of this mass in the data as points, along with various simulated distributions. The open histogram is for simulated $\eta\rho \to 2(\pi^+\pi^-)\pi^0$ events, is normalized to data, and shows only a narrow η peak. The dashed histogram for simulated $\omega\pi^+\pi^-$ events shows a strong ω peak with a tail toward lower masses that contributes a small number of events in the η region. The hatched histogram for simulated uds events is normalized as described in Sec. IV A and shows both η and ω signals over a small combinatoric contribution.

We define an η signal region as mass in the range 525–575 MeV/c^2, indicated by the inner vertical lines in Fig. 7, and two sidebands, 500–525 and 575–600 MeV/c^2, indicated by the outer vertical lines. The η signal region contains 1897 data events, and we show their $2(\pi^+\pi^-)\pi^0$ invariant mass distribution as the open histogram in Fig. 8. The hatched histogram is the uds back-

TABLE I. Measurements of the $e^+e^- \to 2(\pi^+\pi^-)\pi^0$ cross section (errors are statistical only).

$E_{\rm c.m.}$ (GeV)	σ (nb)	$E_{\rm c.m.}$ (GeV)	σ (nb)	$E_{\rm c.m.}$ (GeV)	σ (nb)	$E_{\rm c.m.}$ (GeV)	σ (nb)
1.0125	0.02 ± 0.03	1.8875	1.64 ± 0.21	2.7625	0.39 ± 0.13	3.6375	0.16 ± 0.08
1.0375	-0.01 ± 0.04	1.9125	1.96 ± 0.21	2.7875	0.20 ± 0.12	3.6625	0.38 ± 0.09
1.0625	0.03 ± 0.05	1.9375	1.88 ± 0.21	2.8125	0.38 ± 0.12	3.6875	1.55 ± 0.12
1.0875	-0.01 ± 0.05	1.9625	1.76 ± 0.20	2.8375	0.25 ± 0.12	3.7125	0.40 ± 0.09
1.1125	0.04 ± 0.06	1.9875	1.47 ± 0.20	2.8625	0.07 ± 0.12	3.7375	0.17 ± 0.08
1.1375	0.02 ± 0.05	2.0125	1.66 ± 0.20	2.8875	0.23 ± 0.12	3.7625	0.14 ± 0.07
1.1625	0.09 ± 0.07	2.0375	1.57 ± 0.20	2.9125	0.30 ± 0.12	3.7875	0.14 ± 0.07
1.1875	0.20 ± 0.08	2.0625	1.77 ± 0.20	2.9375	0.29 ± 0.12	3.8125	0.08 ± 0.07
1.2125	0.13 ± 0.09	2.0875	1.33 ± 0.19	2.9625	0.35 ± 0.12	3.8375	0.27 ± 0.07
1.2375	-0.02 ± 0.10	2.1125	1.44 ± 0.19	2.9875	0.45 ± 0.11	3.8625	0.08 ± 0.06
1.2625	0.25 ± 0.12	2.1375	1.42 ± 0.19	3.0125	0.31 ± 0.12	3.8875	0.09 ± 0.07
1.2875	0.31 ± 0.13	2.1625	1.76 ± 0.19	3.0375	0.39 ± 0.12	3.9125	0.18 ± 0.07
1.3125	0.50 ± 0.14	2.1875	1.38 ± 0.18	3.0625	1.55 ± 0.15	3.9375	0.15 ± 0.07
1.3375	0.72 ± 0.16	2.2125	1.12 ± 0.18	3.0875	17.13 ± 0.35	3.9625	0.14 ± 0.06
1.3625	0.91 ± 0.17	2.2375	1.75 ± 0.19	3.1125	10.76 ± 0.29	3.9875	0.03 ± 0.06
1.3875	0.95 ± 0.18	2.2625	1.56 ± 0.18	3.1375	0.90 ± 0.13	4.0125	0.10 ± 0.06
1.4125	1.58 ± 0.21	2.2875	1.20 ± 0.17	3.1625	0.32 ± 0.11	4.0375	0.11 ± 0.06
1.4375	1.65 ± 0.22	2.3125	1.04 ± 0.16	3.1875	0.23 ± 0.11	4.0625	0.09 ± 0.06
1.4625	1.67 ± 0.22	2.3375	1.25 ± 0.17	3.2125	0.31 ± 0.10	4.0875	0.05 ± 0.06
1.4875	1.92 ± 0.24	2.3625	0.92 ± 0.16	3.2375	0.25 ± 0.10	4.1125	0.04 ± 0.06
1.5125	2.20 ± 0.24	2.3875	0.82 ± 0.15	3.2625	0.15 ± 0.09	4.1375	0.13 ± 0.06
1.5375	2.20 ± 0.24	2.4125	1.13 ± 0.15	3.2875	0.17 ± 0.10	4.1625	0.16 ± 0.06
1.5625	2.37 ± 0.25	2.4375	0.58 ± 0.14	3.3125	0.40 ± 0.10	4.1875	0.18 ± 0.06
1.5875	2.36 ± 0.25	2.4625	0.81 ± 0.15	3.3375	0.07 ± 0.09	4.2125	0.14 ± 0.06
1.6125	3.34 ± 0.27	2.4875	0.64 ± 0.15	3.3625	0.10 ± 0.09	4.2375	0.11 ± 0.06
1.6375	3.29 ± 0.27	2.5125	0.77 ± 0.14	3.3875	0.24 ± 0.09	4.2625	0.10 ± 0.06
1.6625	3.77 ± 0.27	2.5375	0.52 ± 0.14	3.4125	0.28 ± 0.09	4.2875	0.05 ± 0.06
1.6875	3.20 ± 0.26	2.5625	0.50 ± 0.14	3.4375	0.15 ± 0.09	4.3125	0.11 ± 0.05
1.7125	2.45 ± 0.25	2.5875	0.42 ± 0.13	3.4625	0.03 ± 0.08	4.3375	0.08 ± 0.05
1.7375	2.71 ± 0.24	2.6125	0.39 ± 0.13	3.4875	0.13 ± 0.08	4.3625	0.11 ± 0.05
1.7625	2.53 ± 0.24	2.6375	0.65 ± 0.14	3.5125	0.24 ± 0.09	4.3875	0.08 ± 0.05
1.7875	2.31 ± 0.23	2.6625	0.49 ± 0.13	3.5375	0.06 ± 0.08	4.4125	0.03 ± 0.05
1.8125	2.50 ± 0.23	2.6875	0.51 ± 0.13	3.5625	0.18 ± 0.08	4.4375	0.11 ± 0.05
1.8375	2.14 ± 0.22	2.7125	0.74 ± 0.13	3.5875	0.16 ± 0.08	4.4625	0.07 ± 0.05
1.8625	1.93 ± 0.21	2.7375	0.29 ± 0.12	3.6125	0.07 ± 0.08	4.4875	0.15 ± 0.06

ground, evaluated as described in Sec. IVA, which contributes mostly at higher masses. We evaluate the remaining background in two ways. Using the control region of the $\chi^2_{4\pi\pi^0}$ distribution, as discussed in Sec. IVA but only in the η signal region, we obtain the mass distribution shown as the points in Fig. 8. Alternatively, the mass distribution for events in the η sidebands is shown as the dashed histogram. These two distributions are consistent, indicating that very few non-η $2(\pi^+\pi^-)\pi^0$ events are present. Here we use the sideband distribution since it is more precise and contains all backgrounds. The inset in Fig. 8 shows the distribution in the region below 1.3 GeV/c^2 with finer binning. A signal from the direct $e^+e^- \to \eta'\gamma$ process is visible; these events were studied in our previous measurement [25].

The invariant mass distribution of the $\pi^+\pi^-$ pair not from the η is shown after subtraction of the uds and

TABLE II. Summary of systematic uncertainties on the $e^+e^- \to 2(\pi^+\pi^-)\pi^0$ cross section. The total uncertainty is the sum in quadrature of the components.

Source	Correction	Uncertainty	
Radiative corrections	$\cdots$	1%	
Backgrounds	$\cdots$	5%	$E_{\rm c.m.} = 1.7$ GeV
		20%	$E_{\rm c.m.} = 2.5$ GeV
		50%	$E_{\rm c.m.} = 3.5$ GeV
Model dependence	$\cdots$	3%	
$\chi^2_{4\pi\pi^0}$ Distribution	$\cdots$	3%	
Tracking efficiency	+3%	2%	
π^0 efficiency	+3%	3%	
ISR luminosity	$\cdots$	3%	
Total	+6%	8%	$E_{\rm c.m.} = 1.7$ GeV
		20%	$E_{\rm c.m.} = 2.5$ GeV
		50%	$E_{\rm c.m.} = 3.5$ GeV

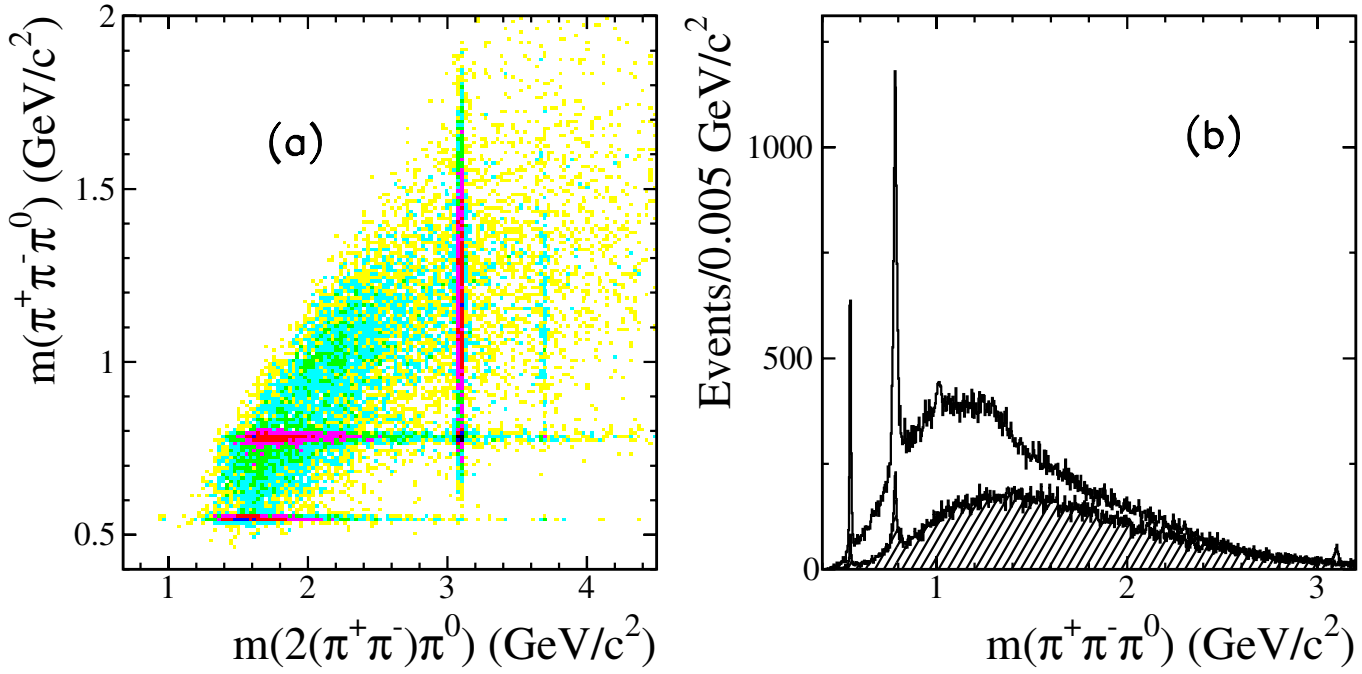

FIG. 5 (color online). (a) The smallest $\pi^+\pi^-\pi^0$ mass in each selected $2(\pi^+\pi^-)\pi^0$ event versus the five-pion mass. (b) The full $\pi^+\pi^-\pi^0$ mass distribution (four entries per event) in these events. The crosshatched histogram represents the estimated non-ISR background.

η-sideband backgrounds as the points in Fig. 9, and has a strong peak in the $\rho(770)$ region. The histogram in Fig. 9 is the distribution for simulated $\eta\rho \to 2(\pi^+\pi^-)\pi^0$ events, and its similarity to the data indicates that this channel dominates the $\eta\pi^+\pi^-$ intermediate state. We therefore use the simulated $\eta\rho$ events to estimate the detection efficiency for $\eta\pi^+\pi^-$ events, although the other simulations give consistent results. Figure 10(a) shows the simulated invariant mass distribution for selected events, and Fig. 10(b) shows the simulated efficiency, which includes the 22.6% branching fraction of $\eta \to \pi^+\pi^-\pi^0$.

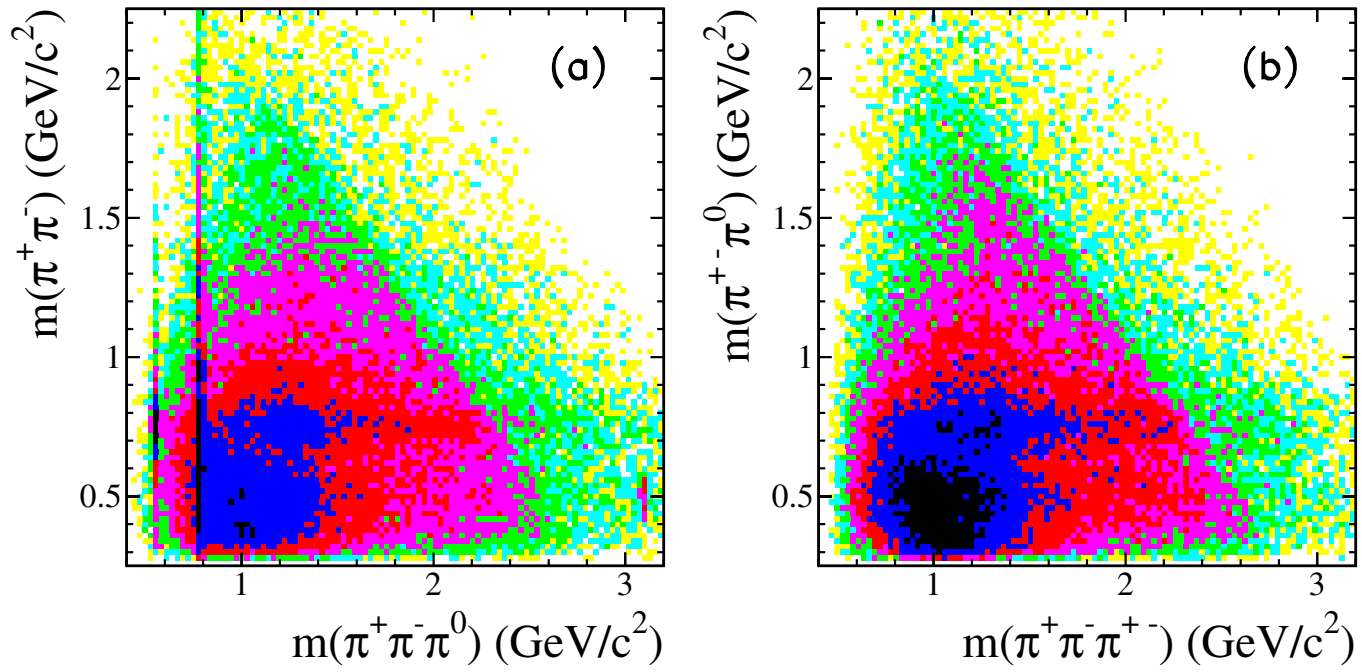

FIG. 6 (color online). Scatter plots of (a) each $\pi^+\pi^-$ mass versus the mass of the remaining $\pi^+\pi^-\pi^0$ and (b) each $\pi^\pm\pi^0$ mass versus the mass of the remaining $\pi^+\pi^-\pi^\pm$ for the selected $2(\pi^+\pi^-)\pi^0$ candidates (four entries per plot per event).

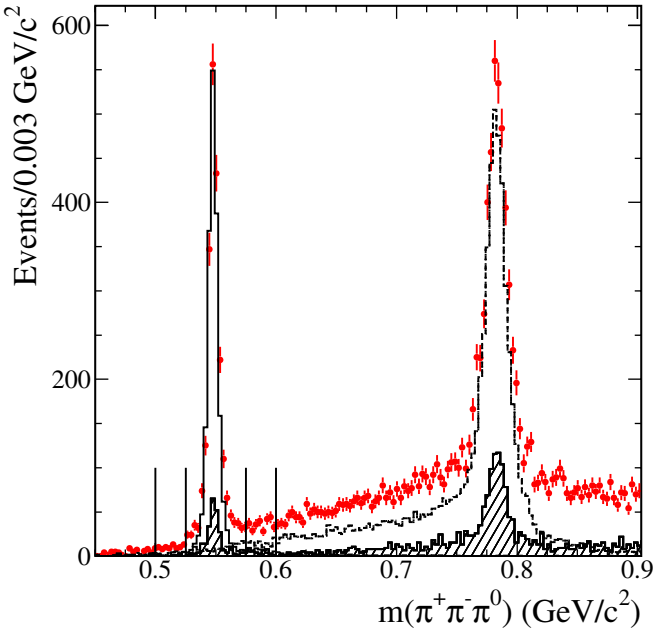

FIG. 7 (color online). Distribution of the $\pi^+\pi^-\pi^0$ mass closest to the η mass in the data (points). The histograms represent the distributions from simulated $\eta\rho$ (open), $\omega\pi^+\pi^-$ (dashed), and *uds* events (hatched), normalized as described in the text. The inner (inner and outer) vertical lines delimit the $\eta\pi^+\pi^-$ signal (sideband) region.

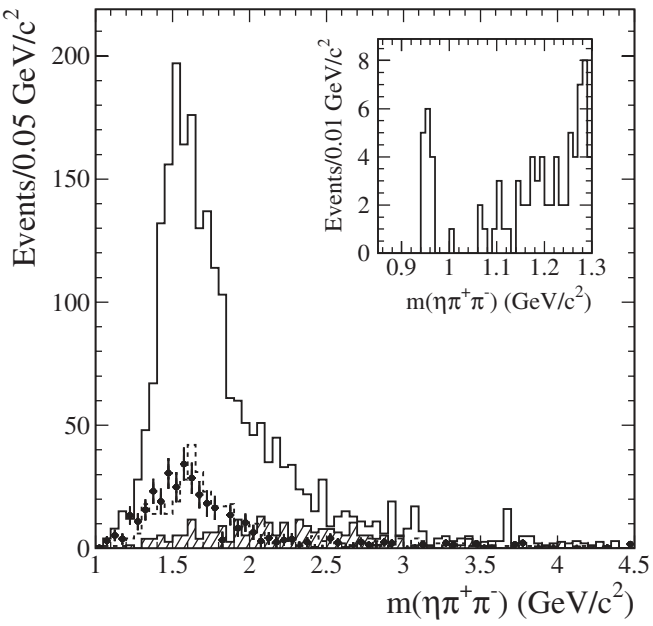

FIG. 8. Invariant mass distribution for events in the $\eta\pi^+\pi^-$ signal (open histogram) and sideband (dashed) regions (see Fig. 7). The points represent the background obtained from the $\chi^2_{4\pi\pi^0}$ control region, and the hatched histogram is that from *uds* events. The inset shows the low end of the mass distribution, where direct $e^+e^- \to \eta'\gamma$ events are visible.

Subtracting the backgrounds and dividing by the ISR luminosity and efficiency, parametrized by the third order polynomial fit shown in Fig. 10(b) and corrected as discussed above, we obtain the $e^+e^- \to \eta\pi^+\pi^-$ cross section shown in Fig. 11. Also shown are the previous direct e^+e^- measurements from the DM2 [13], CMD2 [15], and ND [16] experiments. All measurements are consistent, and ours covers the widest energy range and is by far the most precise above 1.4 GeV.

The cross section shows a steep rise from $\eta\rho(770)$ threshold, followed by a general decrease with increasing energy. Possible structures near 1.6 and 1.8 GeV cannot be resolved with the current statistics. We list the cross section in Table III for c.m. energies up to 3 GeV with statistical errors only. The systematic uncertainties are the same as those discussed in Sec. IV C, totaling about 8% below 3 GeV. Above 3 GeV the cross section is consistent with zero within the current statistical errors, except for the J/ψ peak, which is discussed below.

F. $\omega\pi^+\pi^-$ and ωf_0 intermediate states

To extract the contribution of the $\omega\pi^+\pi^-$ intermediate state we select the $\pi^+\pi^-\pi^0$ combination with mass closest to the ω mass. Events with this mass below 0.6 GeV/c^2 are predominantly $\eta\pi^+\pi^-$ events, and we ignore them. Subtracting the simulated *uds* background and ISR-type background from the $\chi^2_{4\pi\pi^0}$ control region, as described in Sec. IV A, we obtain the mass distribution shown in Fig. 12 as points. The histogram is for simulated $\omega\pi^+\pi^-$ events and describes the peak in the data well, but a background from non-$\omega\pi^+\pi^-$, non-$\eta\pi^+\pi^-$ events is still present.

We define an ω signal region as $\pi^+\pi^-\pi^0$ mass in the range 745–825 MeV/c^2, indicated by the inner vertical lines in Fig. 12 and containing 7693 events, and two sidebands, 706–745 and 825–865 MeV/c^2, indicated by the outer vertical lines. Figure 13 shows the invariant mass distributions for events in the signal region (points) and sidebands (hatched histogram). The sideband events are ISR $2(\pi^+\pi^-)\pi^0$ events but without an ω or η. They contribute mostly at higher energies including the J/ψ peak.

We evaluate the detection efficiency using the $\omega\pi^+\pi^-$ phase space simulation. It is similar to that in Fig. 3, differing by few percent due to the additional selection criteria. Subtracting the sideband background and dividing by the corrected efficiency, ISR luminosity and the 89.1% branching fraction of $\omega \to \pi^+\pi^-\pi^0$, we obtain the $e^+e^- \to \omega\pi^+\pi^-$ cross section shown in Fig. 14. Also shown are the previous direct e^+e^- measurements from the DM2 [14], DM1 [12], and CMD2 [15] experiments. All measurements are consistent, and ours cover the widest energy range and are by far the most precise above 1.4 GeV.

The cross section is consistent with zero below 1.2 GeV, then rises to a peak value of about 2.5 nb at about 1.65 GeV, followed by a general decrease with increasing energy. We

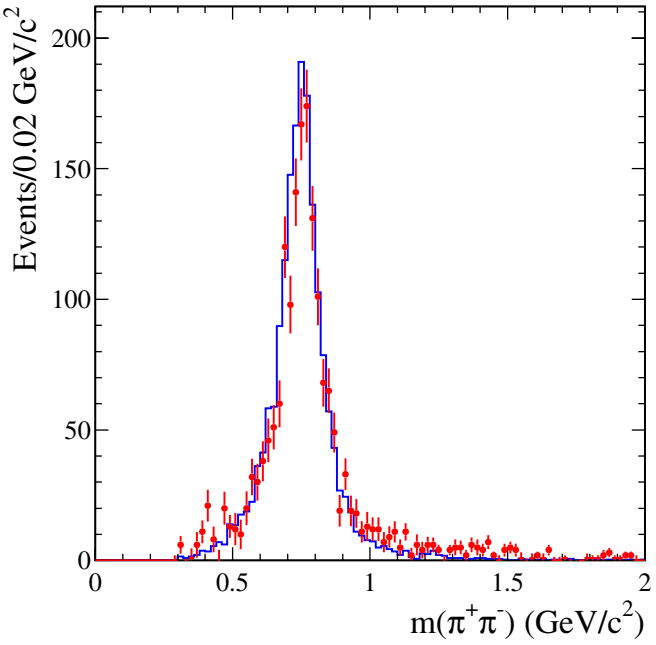

FIG. 9 (color online). Invariant mass distribution of the $\pi^+\pi^-$ pair not from the η in selected $\eta\pi^+\pi^-$ events in the data (points) and in simulated $\eta\rho$ events (histogram).

list the cross section in Table IV for c.m. energies up to 2.4 GeV with statistical errors only. The systematic uncertainties are the same as those discussed in Sec. IV C, totaling about 8% in this range. Above 2.4 GeV the cross section is consistent with zero within the current statistical errors, except for the J/ψ peak, which is discussed below.

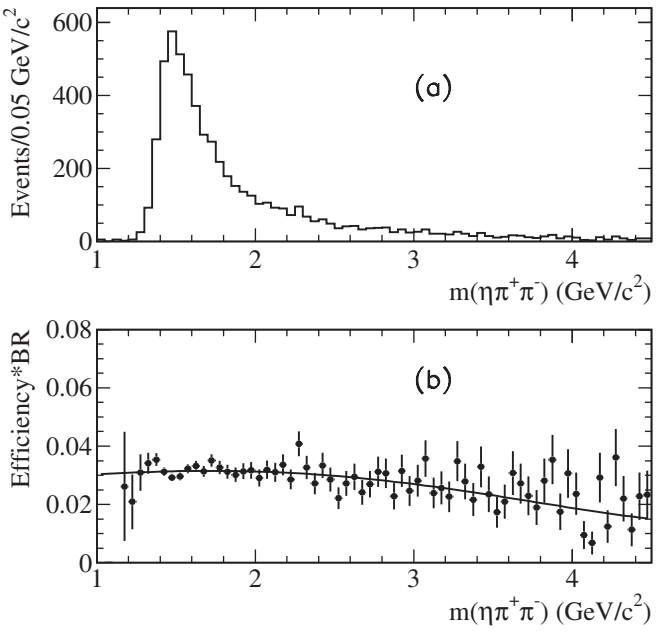

FIG. 10. (a) Invariant mass distribution for selected simulated $\eta\rho$ events, and (b) the detection efficiency versus mass, including the $\eta \to \pi^+\pi^-\pi^0$ branching fraction.

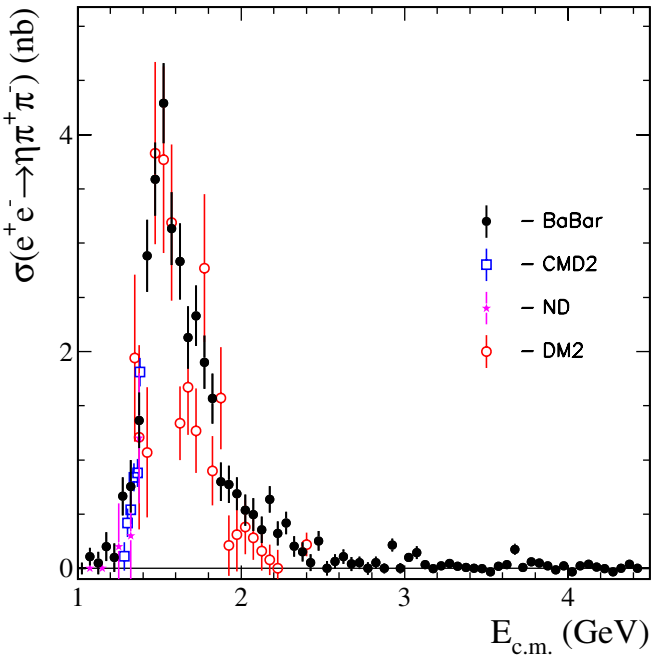

FIG. 11 (color online). The $e^+e^- \to \eta\pi^+\pi^-$ cross section as a function of c.m. energy obtained via ISR at *BABAR*. The direct measurements from DM2, ND, and CMD2 are also shown. Only statistical errors are shown.

For events in the ω signal region with a five-pion mass below 3.0 GeV/c^2, we show the invariant mass distribution of the $\pi^+\pi^-$ pair not from the ω in Fig. 15(a). A peak is visible in the data at the $f_0(980)$ mass, and the histogram is for a simulation that includes $\omega\pi^+\pi^-$ phase space and $\omega f_0(980)$ combined so as to describe the data. We define an $\omega f_0(980)$ signal region by this $\pi^+\pi^-$ mass in the region 0.88–1.04 GeV/c^2, indicated by the inner vertical lines in Fig. 15(a), and sidebands 0.80–0.88 and 1.04–1.12 GeV/c^2, indicated by the outer lines. Subtracting the sideband contribution from that in the signal region and dividing by the corrected efficiency, ISR luminosity and the 2/3 branching fraction of $f_0(980) \to \pi^+\pi^-$ (assuming 2π decay mode dominance [5]), we obtain the $e^+e^- \to \omega f_0(980)$ cross section shown in Fig. 15(b) and listed in Table V. This measurement of the cross section shows a very fast rise from threshold and a possible structure at about 1.85 GeV/c^2, followed by a monotonic decrease with increasing energy.

We subtract the $e^+e^- \to \omega f_0(980)$ cross section from the inclusive $e^+e^- \to \omega\pi^+\pi^-$ cross section to obtain the cross section shown in Fig. 16. A peak is visible, presumably from the $\omega(1650)$, and the shoulder at lower masses can be attributed to the $\omega(1420)$. We fit this cross section as a function of $E_{\text{c.m.}} = \sqrt{s}$ from threshold up to 2.4 GeV with a sum of vector resonances,

$$\sigma(E_{\text{c.m.}}) = \frac{P(s)}{s}\left|\sum_{k=1}^{n}\frac{\sqrt{\sigma_{0k}}m_k^2\Gamma_k}{m_k^2 - s - i\sqrt{s}\Gamma_k}\frac{e^{i\phi_k}}{\sqrt{P(m_k^2)}}\right|^2 \quad (3)$$

TABLE III. Measurements of the $e^+e^- \to \eta\pi^+\pi^-$ cross section (errors are statistical only).

$E_{\rm c.m.}$ (GeV)	σ (nb)	$E_{\rm c.m.}$ (GeV)	σ (nb)	$E_{\rm c.m.}$ (GeV)	σ (nb)	$E_{\rm c.m.}$ (GeV)	σ (nb)
1.0250	0.00 ± 0.05	1.5250	4.29 ± 0.37	2.0250	0.54 ± 0.14	2.5250	0.00 ± 0.07
1.0750	0.11 ± 0.08	1.5750	3.13 ± 0.34	2.0750	0.50 ± 0.15	2.5750	0.06 ± 0.07
1.1250	0.05 ± 0.10	1.6250	2.83 ± 0.35	2.1250	0.36 ± 0.12	2.6250	0.11 ± 0.07
1.1750	0.20 ± 0.13	1.6750	2.13 ± 0.29	2.1750	0.64 ± 0.12	2.6750	0.02 ± 0.07
1.2250	0.10 ± 0.13	1.7250	2.33 ± 0.28	2.2250	0.32 ± 0.11	2.7250	0.05 ± 0.06
1.2750	0.66 ± 0.18	1.7750	1.90 ± 0.25	2.2750	0.42 ± 0.10	2.7750	0.00 ± 0.06
1.3250	0.76 ± 0.24	1.8250	1.57 ± 0.23	2.3250	0.16 ± 0.10	2.8250	0.05 ± 0.06
1.3750	1.37 ± 0.26	1.8750	0.80 ± 0.18	2.3750	0.15 ± 0.09	2.8750	0.00 ± 0.05
1.4250	2.88 ± 0.33	1.9250	0.77 ± 0.17	2.4250	0.05 ± 0.08	2.9250	0.20 ± 0.06
1.4750	3.59 ± 0.34	1.9750	0.69 ± 0.15	2.4750	0.25 ± 0.09	2.9750	0.00 ± 0.05

$$\sigma_{0k} = \frac{12\pi B_{ke} B_{kf} C}{m_k^2}, \qquad P(s) = \sqrt{s - m_0^2}, \qquad (4)$$

where Γ_k and m_k are the full width and mass of the kth resonance, B_{ke} and B_{kf} are its branching fractions to e^+e^- and the final state $f = \omega\pi^+\pi^-$, respectively, $P(s)$ is a simple approximation of the phase space with a threshold cutoff at $m_0 = 1.2$ GeV, and $C = 3.893 \times 10^5$ nb GeV^2 is a conversion constant. This formulation allows the extraction not only of the product $B_{ke}B_{kf}$ but also the peak cross section σ_{0k} or the product $\Gamma_{ke}B_{vf}$.

We consider the resonances, $k = \omega(782)$ (ω), $\omega(1420)$ (ω'), and $\omega(1650)$ (ω''), where $\omega(782)$ is below threshold and is used as a convenient "coherent background" with parameters fixed to PDG values [5] and with $\phi_{\omega(782)}$ set to 0. We perform three fits, the results of which are listed in Table VI and compared with results of a similar fit from our study of the ISR $\pi^+\pi^-\pi^0$ process [8] and with current PDG values [5]. In the first fit, we set the contribution from ω to zero and set $\phi_{\omega''} = 0$. The fitted cross section is dominated by ω'', and the ω' has a relatively narrow width.

Next we float the contribution from ω but fix the relative phases to the values used in our ISR $\pi^+\pi^-\pi^0$ study [8], $\phi_{\omega'} = \pi$ and $\phi_{\omega''} = 0$. The resulting contribution from ω' is almost 10 times higher due to destructive interference, but the masses and widths are similar to those from the first fit. In particular the ω' width is lower than that found in Ref. [8]. The fitted peak ω cross section corresponds to a large $\omega\pi^+\pi^-$ branching fraction of about 7%, but this is driven by the data above 2 GeV and should be considered a measure of the coherent background.

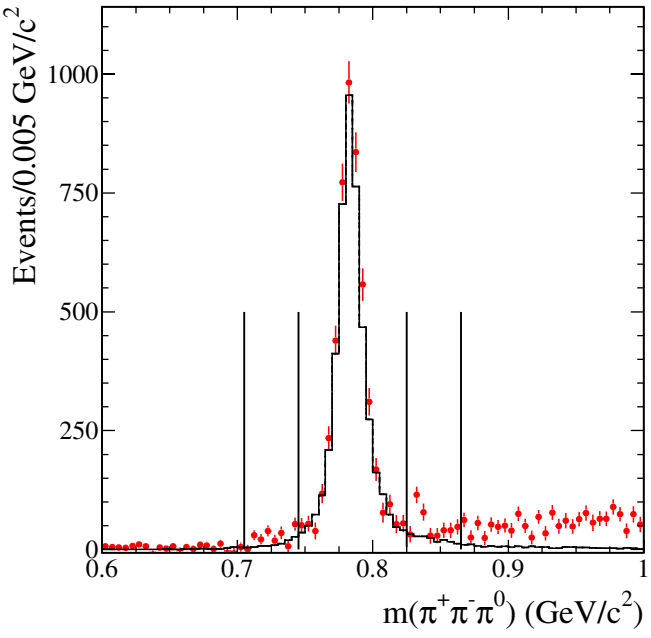

FIG. 12 (color online). Distribution of the $\pi^+\pi^-\pi^0$ mass closest to the ω mass in the data (points) after subtraction of *uds* and ISR-type backgrounds. The histogram is the distribution for simulated $\omega\pi^+\pi^-$ events. The inner (inner and outer) vertical lines delimit the ω signal (sideband) region.

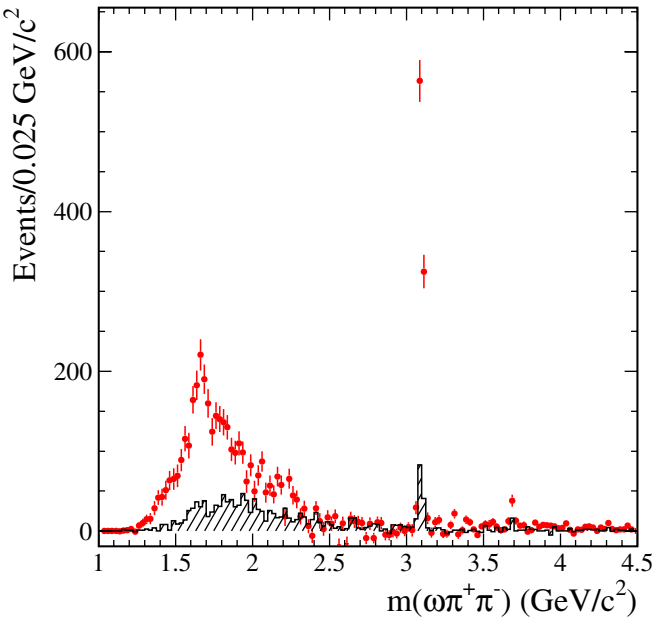

FIG. 13 (color online). Invariant mass distribution for events in the $\omega\pi^+\pi^-$ signal region (points) and sidebands (hatched histogram).

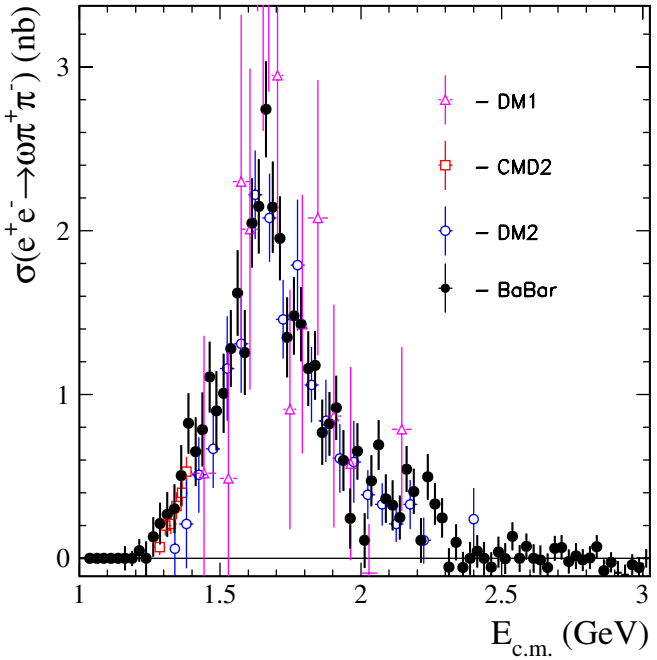

FIG. 14 (color online). The $e^+e^- \to \omega\pi^+\pi^-$ cross section as a function of c.m. energy obtained via ISR at *BABAR*. The direct measurements from DM1, DM2, and CMD2 are also shown. Only statistical errors are shown.

An interference with other unaccounted vector mesons could produce deviations from the assumed values of the phases. To demonstrate this we float the ω level and both relative phases, and show the result as the curve in Fig. 16. The coherent background is larger and both the ω' and ω'' peak cross sections are much lower than in the second fit. Both masses are consistent with the other fits, but the ω' (ω'') width is larger (smaller) and statistically consistent with our ISR $\pi^+\pi^-\pi^0$ study.

A better understanding of the background, including any structure above 2 GeV and any contribution from excited ρ or ϕ states, is needed in order to make precise measurements of the excited ω resonance parameters. Taking the results from the second fit and using the differences from the other fits to estimate systematic errors, we obtain:

$$m_{\omega(1420)} = 1.38 \pm 0.02 \pm 0.07 \text{ GeV}/c^2,$$
$$\Gamma_{\omega(1420)} = 0.13 \pm 0.05 \pm 0.10 \text{ GeV},$$
$$m_{\omega(1650)} = 1.667 \pm 0.013 \pm 0.006 \text{ GeV}/c^2,$$
$$\Gamma_{\omega(1650)} = 0.222 \pm 0.025 \pm 0.020 \text{ GeV}.$$

The $\omega(1650)$ width is significantly different from the PDG value [5] based on the DM2 results [14,15], but consistent with our measurement in ISR $\pi^+\pi^-\pi^0$ events [8]. Note that the structure, observed in our study of ISR $\omega(782)\eta$ events [10] and described by a resonance with $m = 1.645 \pm 0.008$ GeV/c^2 and $\Gamma = 0.114 \pm 0.014$ GeV can also be interpreted as $\omega(1650)$.

G. $\rho(770)3\pi$ intermediate states

To study events containing a charged or neutral $\rho(770)$ we first exclude any event in which a $\pi^+\pi^-\pi^0$ combination has invariant mass within 25 MeV/c^2 of the η mass or within 40 MeV/c^2 of the ω mass. For this study we also exclude events with a five-pion mass within 50 MeV/c^2 of the J/ψ mass. Figure 17 shows the invariant mass distributions for all four $\pi^+\pi^-$ pairs and all four $\pi^\pm\pi^0$ pairs in the remaining events. The ISR and non-ISR backgrounds are subtracted using the procedures described above. These two distributions are quite similar and show strong $\rho(770)$ peaks. The hatched histogram in Fig. 17 shows the mass distribution for the $\pi^+\pi^+$ and $\pi^-\pi^-$ pairs (two entries per event), which gives an estimate of the combinatorial background. The difference between these distributions is consistent with an average of two ρ per event: one ρ is charged and the other neutral, since the yields are consistent and

TABLE IV. Measurement of the $e^+e^- \to \omega\pi^+\pi^-$ cross section (errors are statistical only).

$E_{\text{c.m.}}$ GeV)	σ (nb)	$E_{\text{c.m.}}$ GeV)	σ (nb)	$E_{\text{c.m.}}$ GeV)	σ (nb)	$E_{\text{c.m.}}$ GeV)	σ (nb)
1.1500	0.00 ± 0.09	1.5000	1.06 ± 0.25	1.8500	0.79 ± 0.20	2.2000	0.11 ± 0.14
1.1750	0.00 ± 0.05	1.5250	1.33 ± 0.24	1.8750	0.84 ± 0.20	2.2250	0.52 ± 0.14
1.2000	0.06 ± 0.08	1.5500	1.67 ± 0.27	1.9000	0.95 ± 0.20	2.2500	0.35 ± 0.13
1.2250	0.00 ± 0.12	1.5750	1.30 ± 0.27	1.9250	0.61 ± 0.19	2.2750	0.27 ± 0.12
1.2500	0.15 ± 0.14	1.6000	2.10 ± 0.28	1.9500	0.28 ± 0.18	2.3000	−0.04 ± 0.12
1.2750	0.23 ± 0.14	1.6250	2.21 ± 0.29	1.9750	0.69 ± 0.17	2.3250	0.11 ± 0.11
1.3000	0.30 ± 0.15	1.6500	2.80 ± 0.30	2.0000	0.11 ± 0.17	2.3500	−0.03 ± 0.10
1.3250	0.33 ± 0.16	1.6750	2.19 ± 0.28	2.0250	0.49 ± 0.16	2.3750	0.00 ± 0.10
1.3500	0.55 ± 0.20	1.7000	1.99 ± 0.26	2.0500	0.70 ± 0.15	2.4000	0.05 ± 0.10
1.3750	0.88 ± 0.20	1.7250	1.38 ± 0.25	2.0750	0.40 ± 0.15	2.4250	0.02 ± 0.10
1.4000	0.69 ± 0.22	1.7500	1.51 ± 0.24	2.1000	0.35 ± 0.15	2.4500	−0.04 ± 0.09
1.4250	0.83 ± 0.24	1.7750	1.45 ± 0.23	2.1250	0.26 ± 0.14	2.4750	0.05 ± 0.10
1.4500	1.17 ± 0.23	1.8000	1.18 ± 0.23	2.1500	0.56 ± 0.14	2.5000	0.02 ± 0.10
1.4750	0.95 ± 0.25	1.8250	1.19 ± 0.21	2.1750	0.43 ± 0.14	2.5250	0.15 ± 0.09

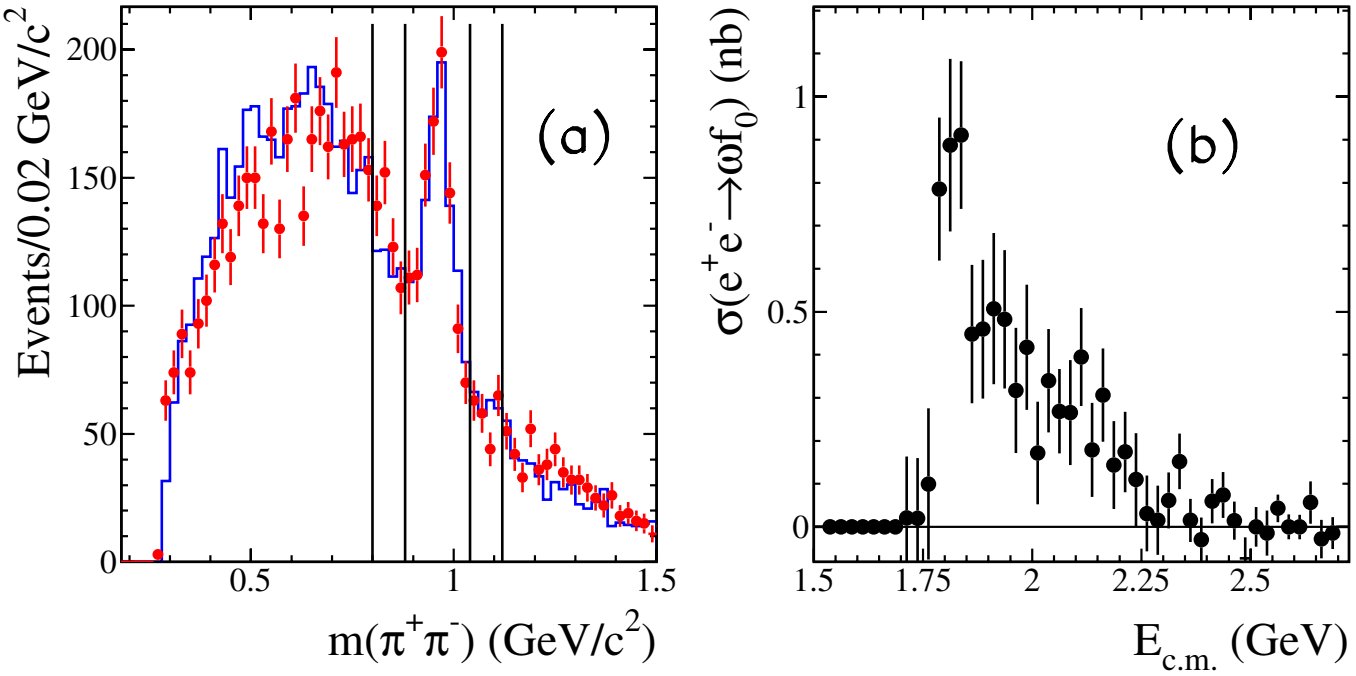

FIG. 15 (color online). (a) Invariant mass distribution of the $\pi^+\pi^-$ pair not from the ω in selected $\omega\pi^+\pi^-$ events in the data (points) and in simulated events (histogram). The vertical lines delimit the $f_0(980)$ signal region and sidebands. (b) The $e^+e^- \to \omega f_0(980)$ cross section.

$e^+e^- \to \rho^0\rho^0\pi^0$ is forbidden by C parity. This suggests one or more quasi-two-body intermediate states, $X^{\pm,0}\rho^{\mp,0}$, where X could be $a_1(1260)$, $\pi(1300)$ or $a_2(1370)$, which have $I = 1$ and a dominant $\rho\pi$ decay.

We now select events that contain a $\pi^\pm\pi^0$ or $\pi^+\pi^-$ pair with mass within 150 MeV/c^2 of the ρ mass. Figure 18(a) shows the mass distributions for the other charged (squares) and neutral (triangles) three-pion combinations (up to four total entries per event). These two distributions are consistent and the hatched histogram is an estimate of the combinatorial background from doubly charged ($\pi^+\pi^+\pi^0$ and $\pi^-\pi^-\pi^0$) combinations. By averaging the charged and neutral distributions and subtracting the combinatorial background we obtain the distribution shown in Fig. 18(b), which is consistent with a resonant structure. Fitting a single Breit-Wigner function gives

$$m(X) = 1.243 \pm 0.012 \pm 0.020 \text{ GeV}/c^2;$$
$$\Gamma(X) = 0.410 \pm 0.031 \pm 0.030 \text{ GeV}.$$

The first errors are statistical and the second systematic, dominated by the background subtraction procedure. These values are inconsistent with the $a_2(1320)$ resonance, but consistent, within large uncertainties, with the $\pi(1300)$ and $a_1(1260)$ [5]. An angular analysis could distinguish between these possibilities, but requires substantially higher statistics due to the large combinatorial background.

Since the events that do not contain an η or ω appear to be predominantly $X\rho(770) \to \rho^0\rho^\pm\pi^\mp$ events, where X is consistent with a single resonance, we obtain an

TABLE V. Measurements of the $e^+e^- \to \omega f_0(980)$ cross section (errors are statistical only).

$E_{c.m.}$ (GeV)	σ (nb)	$E_{c.m.}$ (GeV)	σ (nb)	$E_{c.m.}$ (GeV)	σ (nb)	$E_{c.m.}$ (GeV)	σ (nb)
1.7000	0.02 ± 0.14	1.9000	0.51 ± 0.18	2.1000	0.39 ± 0.11	2.3000	0.06 ± 0.07
1.7250	0.02 ± 0.14	1.9250	0.48 ± 0.16	2.1250	0.18 ± 0.11	2.3250	0.15 ± 0.06
1.7500	0.10 ± 0.18	1.9500	0.32 ± 0.15	2.1500	0.31 ± 0.11	2.3500	0.02 ± 0.05
1.7750	0.79 ± 0.17	1.9750	0.42 ± 0.15	2.1750	0.14 ± 0.10	2.3750	0.03 ± 0.05
1.8000	0.89 ± 0.20	2.0000	0.17 ± 0.12	2.2000	0.17 ± 0.09	2.4000	0.06 ± 0.05
1.8250	0.91 ± 0.17	2.0250	0.34 ± 0.12	2.2250	0.11 ± 0.11	2.4250	0.07 ± 0.05
1.8500	0.45 ± 0.16	2.0500	0.27 ± 0.10	2.2500	0.03 ± 0.09	2.4500	0.01 ± 0.04
1.8750	0.46 ± 0.16	2.0750	0.27 ± 0.12	2.2750	0.02 ± 0.08	2.4750	0.01 ± 0.05

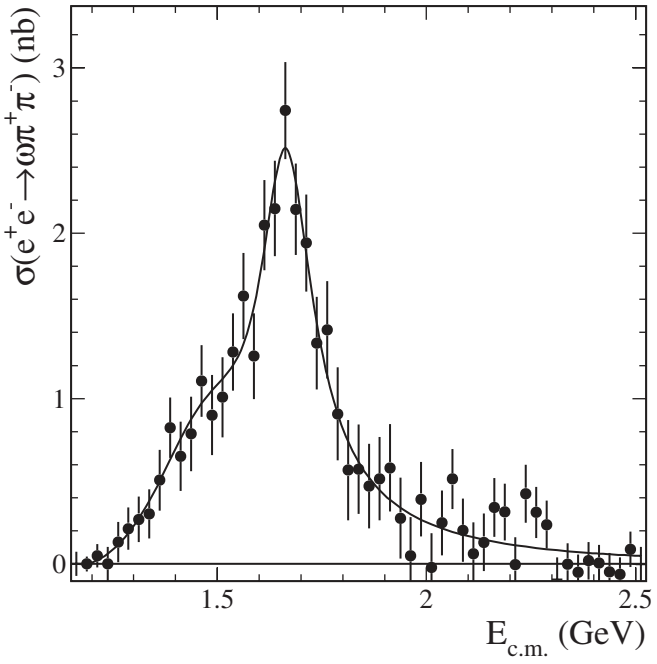

FIG. 16. The $e^+e^- \to \omega\pi^+\pi^-$ cross section excluding the $\omega f_0(980)$ contribution (points). The curve shows the result of the fit of the $\omega(1420)$ and $\omega(1650)$ resonances described in the text (Fit 3 in Table VI).

$e^+e^- \to X\rho(770)$ cross section as the difference between the total $e^+e^- \to 2(\pi^+\pi^-)\pi^0$ cross section (Fig. 4) and the $e^+e^- \to \omega\pi^+\pi^-$ and $e^+e^- \to \eta\pi^+\pi^-$ cross sections (Figs. 10 and 14 with branching fraction corrections removed). We show these three cross sections in Fig. 19(a) for energies up to 3 GeV, and the difference in Fig. 19(b); it shows no sharp structure. Above 3 GeV, the contributions from $\eta\pi^+\pi^-$ and $\omega\pi^+\pi^-$ are consistent with zero, so the cross section is as in Fig. 4, except for the J/ψ and $\psi(2S)$ peaks, which can have a different substructure (see Sec. VIII).

V. $2(\pi^+\pi^-)\eta$ FINAL STATE

A. Final selection and background

To suppress $K^+K^-\pi^+\pi^-\eta$ background, we require that no more than one track in the event is identified as a kaon, and we also require $\chi^2_{2K2\pi\eta} > 30$. We suppress any $K^\pm K^0_S \pi^\mp \eta$ background by requiring all tracks to extrapolate within 2.5 mm of the beam axis. The $\chi^2_{4\pi\eta}$ distribution for the remaining events is shown as points in Fig. 20, and the distribution for simulated $2(\pi^+\pi^-)\pi^0$ events (open histogram) is normalized to the data in the region $\chi^2_{4\pi\eta} < 10$. We have no correct simulation for the $2(\pi^+\pi^-)\eta$ events, but because of uniform acceptance and similar photon spectra we expect the efficiency and resolution for η to be similar to that for π^0. The hatched histogram represents the non-ISR background contribution obtained from the JETSET simulation. It is dominated by $2(\pi^+\pi^-)\pi^0\eta$ events, and we use the same normalization factor as for the $2(\pi^+\pi^-)\pi^0$ events described in Sec. IV B. We define a signal region, $\chi^2_{4\pi\eta} < 40$, containing 4272 events, and a control region for the estimation of other backgrounds, $40 < \chi^2_{4\pi\eta} < 80$, containing 1485 events.

Figure 21 shows the $2(\pi^+\pi^-)\eta$ invariant mass distribution from threshold up to 4.5 GeV/c^2 for events in the signal region. A J/ψ signal is visible. The hatched histogram represents the non-ISR background, and the open histogram represents the sum of all backgrounds, where the ISR-type background is estimated from the control region. Both backgrounds are relatively small at low mass, about 20% altogether, but they account for 50%–80% of the observed data in the 3.0–4.5 GeV/c^2 region. We subtract this total background in each bin to obtain a number of signal events.

B. Cross section for $e^+e^- \to 2(\pi^+\pi^-)\eta$

We calculate the cross section for the $e^+e^- \to 2(\pi^+\pi^-)\eta$ process as described in Sec. IV C, by dividing

TABLE VI. Summary of parameters obtained from the fits described in the text. The values without errors were fixed in that fit.

Fit	1	2	3	3π [8]	PDG [5]
$\sigma_{0w'}$ (nb)	0.10 ± 0.08	1.01 ± 0.29	0.64 ± 0.34	···	···
$B_{ee}B_{w'f} \times 10^6$	0.013 ± 0.010	0.13 ± 0.04	0.101 ± 0.055	0.82 ± 0.08	···
$\Gamma_{ee}B_{w'f}$ (eV)	1.4 ± 1.01	17.5 ± 5.4	37.8 ± 12.1	369	···
$m_{w'}$ (GeV/c^2)	1.381 ± 0.032	1.382 ± 0.023	1.463 ± 0.070	1.350 ± 0.030	1.40–1.45
$\Gamma_{w'}$ (GeV)	0.105 ± 0.090	0.133 ± 0.048	0.383 ± 0.233	0.450 ± 0.140	0.180–0.250
$\phi_{w'}$ (rad.)	-1.93 ± 0.73	π	-0.61 ± 0.94	π	···
$\sigma_{0w''}$ (nb)	2.14 ± 0.18	2.47 ± 0.18	1.03 ± 0.54	···	···
$B_{ee}B_{w''f} \times 10^6$	0.41 ± 0.03	0.47 ± 0.04	0.193 ± 0.087	1.3 ± 0.2	···
$\Gamma_{ee}B_{w''f}$ (eV)	96.5 ± 10.9	103.5 ± 8.3	28.7 ± 7.7	286	···
$m_{w''}$ (GeV/c^2)	1.673 ± 0.011	1.667 ± 0.013	1.661 ± 0.032	1.660 ± 0.011	1.670 ± 0.030
$\Gamma_{w''}$ (GeV)	0.236 ± 0.029	0.222 ± 0.025	0.148 ± 0.037	0.220 ± 0.040	0.315 ± 0.035
$\phi_{w''}$ (rad.)	0	0	0.02 ± 0.71	0	···
σ_{0w} (nb)	0	102 ± 67	147 ± 140	PDG	···
χ^2/n.d.f.	36.2/48	34.9/48	32.2/46	···	···

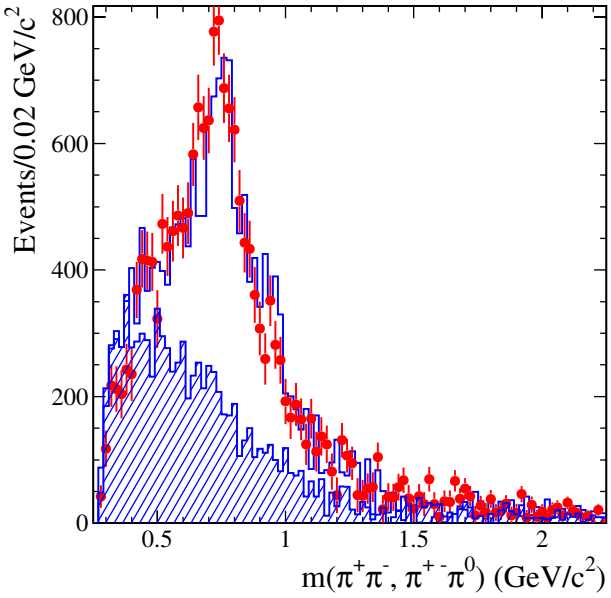

FIG. 17 (color online). The background-subtracted invariant mass distributions for all $\pi^+\pi^-$ pairs (open histogram, four entries per event), $\pi^\pm\pi^0$ pairs (points, four entries per event), and $\pi^+\pi^+$ and $\pi^-\pi^-$ pairs (hatched histogram, two entries per event), for events with no η or $\omega \to \pi^+\pi^-\pi^0$ candidates.

the number of events in each $2(\pi^+\pi^-)\eta$ mass bin by the corrected detection efficiency and differential luminosity. The angular acceptance is uniform in all of our simulations, and this has been demonstrated in our previous studies of four- and six-pion final states [9,10]. We therefore use the same detection efficiency as for the $2(\pi^+\pi^-)\pi^0$ process, shown in Fig. 3, divided by the $\eta \to \gamma\gamma$ branching fraction of 39.28% [5], and with the systematic error increased to 5%. We use the same corrections and uncertainties for the χ^2 cut, tracking efficiency and η-finding efficiency.

We show the cross section as a function of energy in Fig. 22 with statistical errors only, and provide a list of our results in Table VII. This is the first measurement of this cross section, which shows a peak value of about 1.2 nb at about 2.2 GeV, followed by a monotonic decrease toward higher energies, broken only by a peak at the J/ψ mass, discussed in Sec. VIII. Again, the energy resolution is much smaller than the bin width and we apply no correction. The overall systematic error is about 10% for energies below 3 GeV, rising to 30%–50% in the 3–4.5 GeV region.

C. Substructure in the $2(\pi^+\pi^-)\eta$ final state

We might expect a rich internal structure in the $2(\pi^+\pi^-)\eta$ final state. Figure 23(a) shows the invariant mass distribution of the $\pi^+\pi^-\pi^+\pi^-$ system recoiling against the η, after subtraction of the ISR and non-ISR backgrounds. The concentration around 1.5 GeV/c^2 is consistent with final state $\eta\rho(1450)$ being one of the dominant channels in the $2(\pi^+\pi^-)\eta$ process. Figure 23(b) shows the mass distribution for all neutral $\pi^+\pi^-\eta$ combinations (four entries per event). Signals from the $\eta'(958)$ and a peak at 1.3 GeV/c^2 are evident.

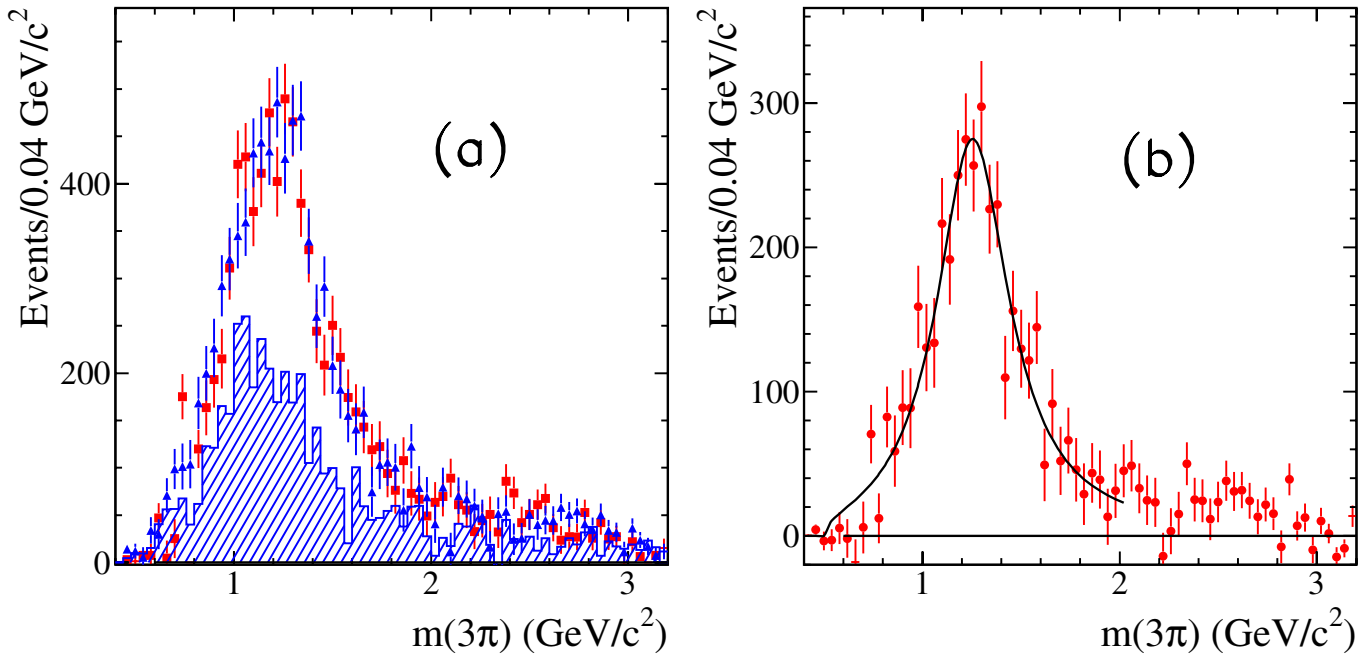

FIG. 18 (color online). (a) The invariant mass distributions for $\pi^+\pi^-\pi^0$ (triangles) and $\pi^+\pi^-\pi^\pm$ (squares) combinations for events in which the other $\pi^+\pi^-$ or $\pi^\pm\pi^0$ pair is in the ρ signal region. The hatched histogram is an estimate of the combinatorial background. (b) The average of the triangles and squares in (a) minus the combinatorial background. The line is the result of a Breit-Wigner fit.

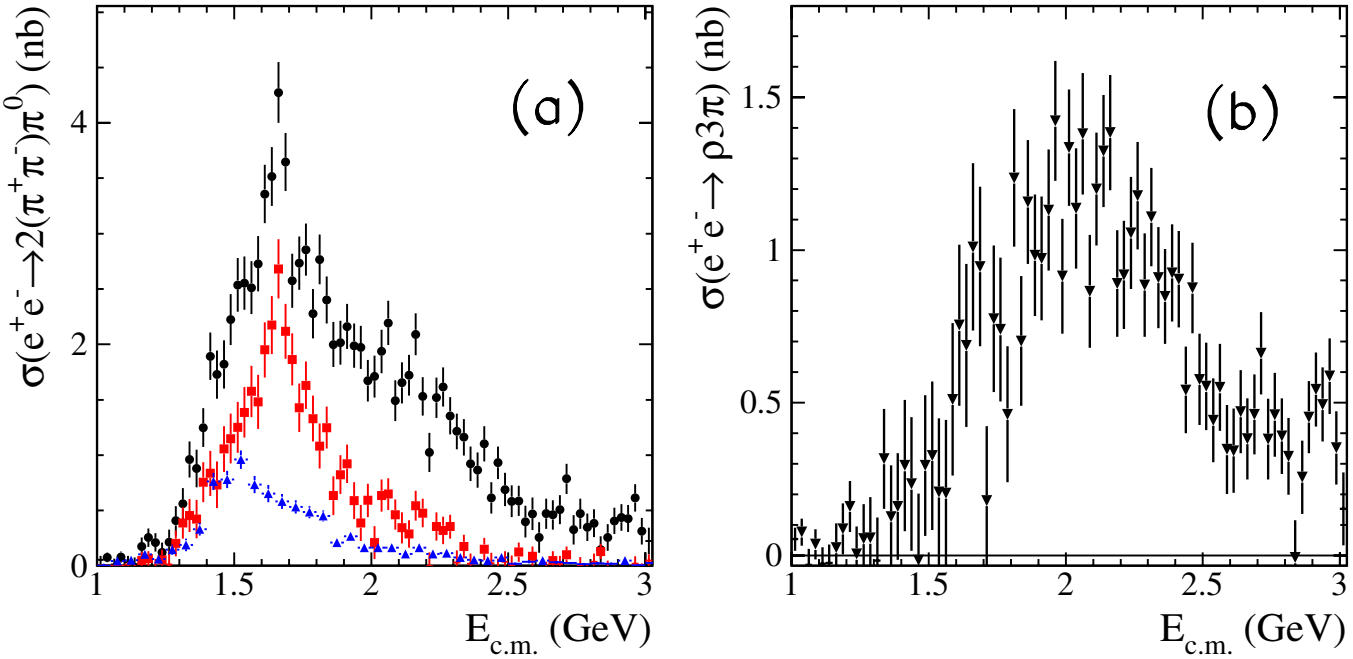

FIG. 19 (color online). (a) The total $e^+e^- \to 2(\pi^+\pi^-)\pi^0$ cross section (circles) and the contributions from $\omega\pi^+\pi^-$ (squares) and $\eta\pi^+\pi^-$ (triangles). (b) The cross section obtained as the difference between the total and the latter two contributions, which is dominated by the $e^+e^- \to \rho(770)X$ process.

There are two candidates decaying to $\eta\pi^+\pi^-$ and allowed by quantum numbers for the latter: $f_1(1285)$ and $\eta(1295)$ [5]. For events with an entry in one of these peaks, the mass of the remaining $\pi^+\pi^-$ pair is concentrated in the $\rho(770)$ region, indicating that these events are predominantly from the $\eta'(958)\rho$ and $\eta(1295)\rho$ $[f_1(1285)\rho]$. The process $e^+e^- \to f_1(1285)\rho(770)$ seems to be preferred, because $f_1(1285)$ has the decay to $\gamma\rho(770)$, but $\eta(1295)$ decays to $\eta\pi\pi$ with pions in S wave [5] (and not well studied). We now study these events in detail.

D. $\eta'(958)\pi^+\pi^-$ intermediate state

To extract the contribution from the $\eta'(958)\pi^+\pi^-$ channel, we select the $\pi^+\pi^-\eta$ combination with mass closest to the $\eta'(958)$ mass. Figure 24(a) shows the distribution of this mass below 1.1 GeV/c^2. A clean $\eta'(958)$ signal is visible. Also shown is the estimated contribution from non-ISR background, which is small but also shows an η' peak.

We obtain a cross section in a manner similar to that described in Sec. IV C. We first subtract the non-ISR background in each mass bin, then subtract the events in two sidebands, 930–945 and 975–990 MeV/c^2, from those in an $\eta'(958)$ signal region, 945–975 MeV/c^2, obtaining a total of 120 ± 14 $\eta'(958)\pi^+\pi^-$ events. Repeating this procedure in bins of the $2(\pi^+\pi^-)\eta$ invariant mass and dividing by the efficiency, ISR luminosity, $\eta \to \gamma\gamma$ branching fraction, and the $\eta'(958) \to \eta\pi^+\pi^-$ branching fraction of 0.445 [5], we obtain the $e^+e^- \to \eta'(958)\pi^+\pi^-$ cross section shown in Fig. 24(b) and listed in Table VIII. It shows a resonancelike behavior at around 2.1 GeV and a sharp drop at 3.3 GeV. Fitting a single Breit-Wigner function, Eq. (3) with $m_0 = 1.5$ GeV to describe the phase space, we obtain:

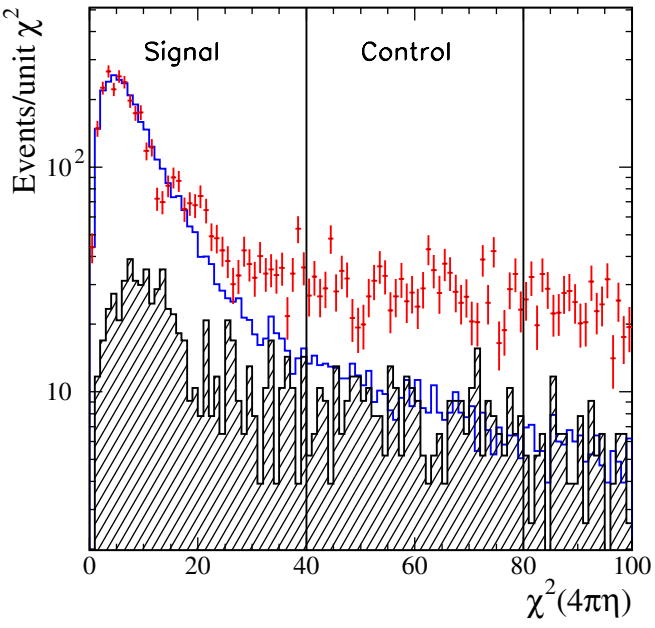

FIG. 20 (color online). Distribution of χ^2 from the 5C fit for $2(\pi^+\pi^-)\eta$ candidates in the data (points). The open and hatched histograms are the distribution for simulated signal events and non-ISR background, respectively, normalized as described in the text.

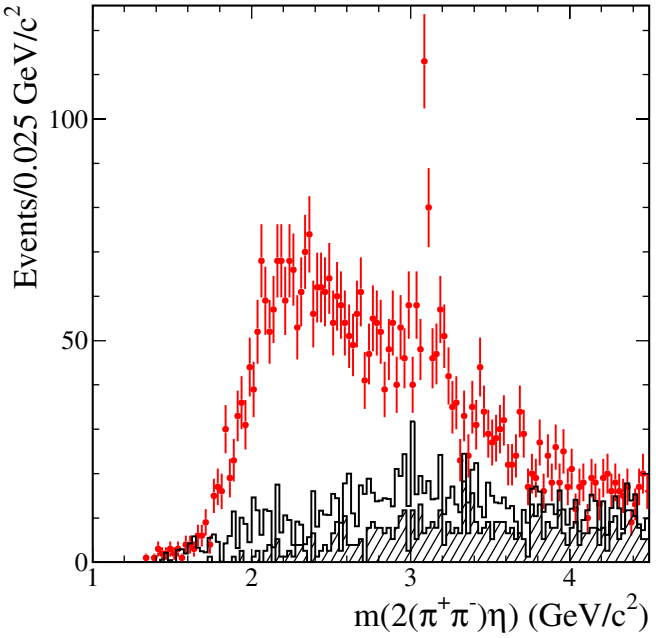

FIG. 21 (color online). Invariant mass distribution for selected $2(\pi^+\pi^-)\eta$ events in the data (points). The hatched and open histograms represent the non-ISR background and the sum of all backgrounds, respectively.

$$\sigma_0 = 0.18 \pm 0.07 \text{ nb}, \qquad m_x = 1.99 \pm 0.08 \text{ GeV}/c^2,$$
$$\Gamma_x = 0.31 \pm 0.14 \text{ GeV}.$$

This might be the $\rho(2150)$, the next radial excitation of the ρ family, reported previously and listed in the detailed PDG tables [5]. The structure around the J/ψ region cannot be explained by the $J/\psi \to \eta'(958)\pi^+\pi^-$ decay, but could be a background from other J/ψ decay modes with a missing π^0 or undetected radiative photon(s).

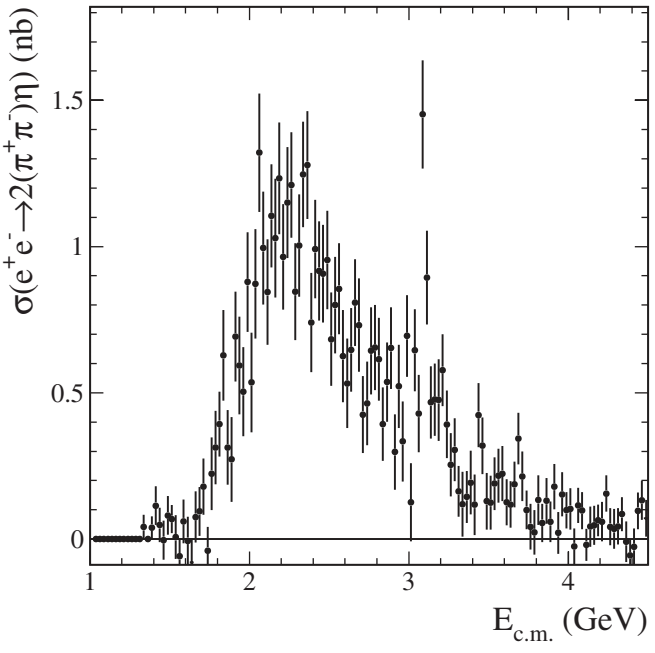

FIG. 22. The $e^+e^- \to 2(\pi^+\pi^-)\eta$ cross section as a function of c.m. energy measured with ISR data. Only statistical errors are shown.

E. $f_1(1285)\pi^+\pi^-$ intermediate state

Figure 25(a) shows an expanded view of the $\pi^+\pi^-\eta$ invariant mass distribution [Fig. 23(b)] in the region around 1.3 GeV/c^2. We fit this distribution with a Breit-Wigner signal function plus a second order polynomial to describe the combinatorial background, obtaining 649 ± 85 events in the peak. The fitted mass and width, $1.281 \pm 0.002 \pm 0.001$ GeV/c^2 and $0.035 \pm 0.006 \pm 0.004$ GeV, are compatible with the $f_1(1285)$ parameters [5] and are not in agreement with those listed for the $\eta(1295)$. We conclude that contribution from the $\eta(1295)\pi^+\pi^-$ is small and more data is needed for detailed study. A similar fit to the η' peak gives a mass shifted from the PDG value by -0.9 ± 0.4 MeV, from which we estimate a 1 MeV systematic error on the $f_1(1285)$ mass. The systematic error on the width is estimated by varying the shape of the combinatorial background.

We extract the number of $f_1(1285)\pi^+\pi^-$ events in 80 MeV/c^2 bins of the $2(\pi^+\pi^-)\eta$ mass using similar fits with the $f_1(1285)$ mass and width fixed to the above values. Because of the uncertainty in the background shape we assign an additional 10% systematic error on the number of signal events. Dividing the fitted number of events by the efficiency, ISR luminosity and $\eta \to \gamma\gamma$ and $f_1(1285) \to \eta\pi^+\pi^-$ branching fractions yields the cross section shown in Fig. 25(b) and listed in Table IX. There is no evidence of the J/ψ decay into this mode, and the cross section again demonstrates resonancelike behavior at around 2.1 GeV. Fitting with a single Breit-Wigner function, Eq. (3) with $m_0 = 1.8$ GeV, we obtain:

$$\sigma_0 = 1.00 \pm 0.18 \pm 0.15 \text{ nb},$$
$$m_x = 2.15 \pm 0.04 \pm 0.05 \text{ GeV}/c^2,$$
$$\Gamma_x = 0.35 \pm 0.04 \pm 0.05 \text{ GeV}.$$

The mass and width are consistent with those obtained above for the $\eta'(958)\pi^+\pi^-$ channel, and with those listed in the PDG tables [5] for the $\rho(2150)$, but the cross section is substantially larger.

VI. $K^+K^-\pi^+\pi^-\pi^0$ FINAL STATE

A. Final selection and backgrounds

To suppress ISR $2(\pi^+\pi^-)\pi^0$ background, we fit each event under that hypothesis and require $\chi^2_{4\pi\pi^0} > 30$. The $\chi^2_{2K2\pi\pi^0}$ distribution for the remaining events is shown as points in Fig. 26 and the distribution for simulated $K^+K^-\pi^+\pi^-\pi^0$ events (open histogram) is normalized to the data in the region $\chi^2_{2K2\pi\pi^0} < 20$. The hatched histo-

TABLE VII. Measurements of the $e^+e^- \to 2(\pi^+\pi^-)\eta$ cross section (errors are statistical only).

$E_{\rm c.m.}$ (GeV)	σ (nb)	$E_{\rm c.m.}$ (GeV)	σ (nb)	$E_{\rm c.m.}$ (GeV)	σ (nb)	$E_{\rm c.m.}$ (GeV)	σ (nb)
1.3125	0.00 ± 0.00	2.1125	0.84 ± 0.18	2.9125	0.30 ± 0.13	3.7125	0.21 ± 0.08
1.3375	0.04 ± 0.04	2.1375	1.10 ± 0.18	2.9375	0.52 ± 0.14	3.7375	0.10 ± 0.07
1.3625	0.00 ± 0.00	2.1625	1.03 ± 0.20	2.9625	0.33 ± 0.14	3.7625	0.04 ± 0.08
1.3875	0.04 ± 0.04	2.1875	1.23 ± 0.19	2.9875	0.69 ± 0.14	3.7875	0.02 ± 0.08
1.4125	0.11 ± 0.07	2.2125	0.96 ± 0.18	3.0125	0.13 ± 0.13	3.8125	0.13 ± 0.08
1.4375	0.05 ± 0.06	2.2375	1.15 ± 0.19	3.0375	0.65 ± 0.14	3.8375	0.06 ± 0.07
1.4625	0.00 ± 0.07	2.2625	1.21 ± 0.18	3.0625	0.43 ± 0.13	3.8625	0.13 ± 0.08
1.4875	0.08 ± 0.07	2.2875	0.85 ± 0.17	3.0875	1.45 ± 0.19	3.8875	0.06 ± 0.07
1.5125	0.07 ± 0.05	2.3125	1.00 ± 0.17	3.1125	0.89 ± 0.16	3.9125	0.18 ± 0.08
1.5375	0.01 ± 0.07	2.3375	1.25 ± 0.18	3.1375	0.47 ± 0.12	3.9375	0.02 ± 0.07
1.5625	-0.06 ± 0.06	2.3625	1.28 ± 0.18	3.1625	0.48 ± 0.12	3.9625	0.15 ± 0.08
1.5875	0.06 ± 0.07	2.3875	0.74 ± 0.17	3.1875	0.48 ± 0.14	3.9875	0.10 ± 0.06
1.6125	-0.01 ± 0.08	2.4125	0.99 ± 0.17	3.2125	0.58 ± 0.12	4.0125	0.10 ± 0.07
1.6375	-0.08 ± 0.08	2.4375	0.92 ± 0.17	3.2375	0.39 ± 0.12	4.0375	-0.02 ± 0.06
1.6625	0.08 ± 0.09	2.4625	0.91 ± 0.17	3.2625	0.25 ± 0.11	4.0625	0.11 ± 0.06
1.6875	0.09 ± 0.08	2.4875	0.95 ± 0.17	3.2875	0.31 ± 0.11	4.0875	0.10 ± 0.06
1.7125	0.18 ± 0.10	2.5125	0.68 ± 0.16	3.3125	0.16 ± 0.09	4.1125	-0.02 ± 0.05
1.7375	-0.04 ± 0.08	2.5375	0.80 ± 0.17	3.3375	0.12 ± 0.11	4.1375	0.04 ± 0.07
1.7625	0.22 ± 0.12	2.5625	0.86 ± 0.16	3.3625	0.14 ± 0.09	4.1625	0.05 ± 0.07
1.7875	0.31 ± 0.13	2.5875	0.63 ± 0.16	3.3875	0.19 ± 0.11	4.1875	0.06 ± 0.05
1.8125	0.39 ± 0.11	2.6125	0.53 ± 0.15	3.4125	0.12 ± 0.10	4.2125	0.06 ± 0.07
1.8375	0.63 ± 0.16	2.6375	0.65 ± 0.14	3.4375	0.42 ± 0.11	4.2375	0.16 ± 0.06
1.8625	0.31 ± 0.13	2.6625	0.81 ± 0.15	3.4625	0.32 ± 0.10	4.2625	0.04 ± 0.06
1.8875	0.27 ± 0.14	2.6875	0.73 ± 0.16	3.4875	0.13 ± 0.10	4.2875	0.03 ± 0.07
1.9125	0.69 ± 0.15	2.7125	0.43 ± 0.13	3.5125	0.12 ± 0.09	4.3125	0.04 ± 0.06
1.9375	0.59 ± 0.17	2.7375	0.46 ± 0.14	3.5375	0.19 ± 0.09	4.3375	0.09 ± 0.06
1.9625	0.50 ± 0.15	2.7625	0.64 ± 0.15	3.5625	0.22 ± 0.09	4.3625	-0.01 ± 0.07
1.9875	0.88 ± 0.17	2.7875	0.65 ± 0.15	3.5875	0.22 ± 0.09	4.3875	-0.06 ± 0.06
2.0125	0.54 ± 0.17	2.8125	0.61 ± 0.14	3.6125	0.13 ± 0.08	4.4125	-0.03 ± 0.06
2.0375	0.87 ± 0.19	2.8375	0.39 ± 0.13	3.6375	0.12 ± 0.08	4.4375	0.10 ± 0.06
2.0625	1.32 ± 0.20	2.8625	0.54 ± 0.14	3.6625	0.19 ± 0.08	4.4625	0.13 ± 0.07
2.0875	0.99 ± 0.19	2.8875	0.65 ± 0.14	3.6875	0.34 ± 0.09	4.4875	0.07 ± 0.06

gram represents the non-ISR background, which is dominated by $K^+K^-\pi^+\pi^-\pi^0\pi^0$ events and checked against data as in Sec. IV A. Since the statistics are low and the scale factor is consistent, we use the same value as for the $2(\pi^+\pi^-)\pi^0$ final state. The largest remaining background is from ISR $K^+K^-\pi^+\pi^-$ events. This contribution, estimated from the simulation using the measured cross section [11], is shown as the dashed histogram in Fig. 26. All other backgrounds are either negligible or distributed uniformly in $\chi^2_{2K2\pi\pi^0}$. We define a signal region, $\chi^2_{2K2\pi\pi^0} < 40$, containing 5565 events and a control region, $40 < \chi^2_{2K2\pi\pi^0} < 80$, containing 1758 events.

Figure 27 shows the $K^+K^-\pi^+\pi^-\pi^0$ invariant mass distribution from threshold up to 4.5 GeV/c^2 for events in the signal region. The hatched histogram represents the non-ISR background, and the open histogram represents the sum of all backgrounds, where the ISR-type background is estimated from the control region. The total background is about 15% at low mass, but accounts for a large fraction of the selected events above about 3.5 GeV/c^2. We subtract the sum of backgrounds from the number of selected events in each mass bin to obtain a number of signal events. Considering uncertainties in the cross sections for the background processes, the normalization of events in the control region and the simulation statistics, we estimate a systematic uncertainty on the signal yield of less than 5% in the 1.6–3.0 GeV/c^2 region, but increasing to 10% in the region above 3 GeV/c^2.

B. Selection efficiency

The detection efficiency is determined in the same manner as in Sec. IV B. Figure 28(a) shows the simulated $K^+K^-\pi^+\pi^-\pi^0$ invariant mass distributions in the signal and control regions from the phase space simulation. We divide the number of reconstructed events in each mass interval by the number generated in that interval to obtain the efficiency shown as the points in Fig. 28(b); the curve

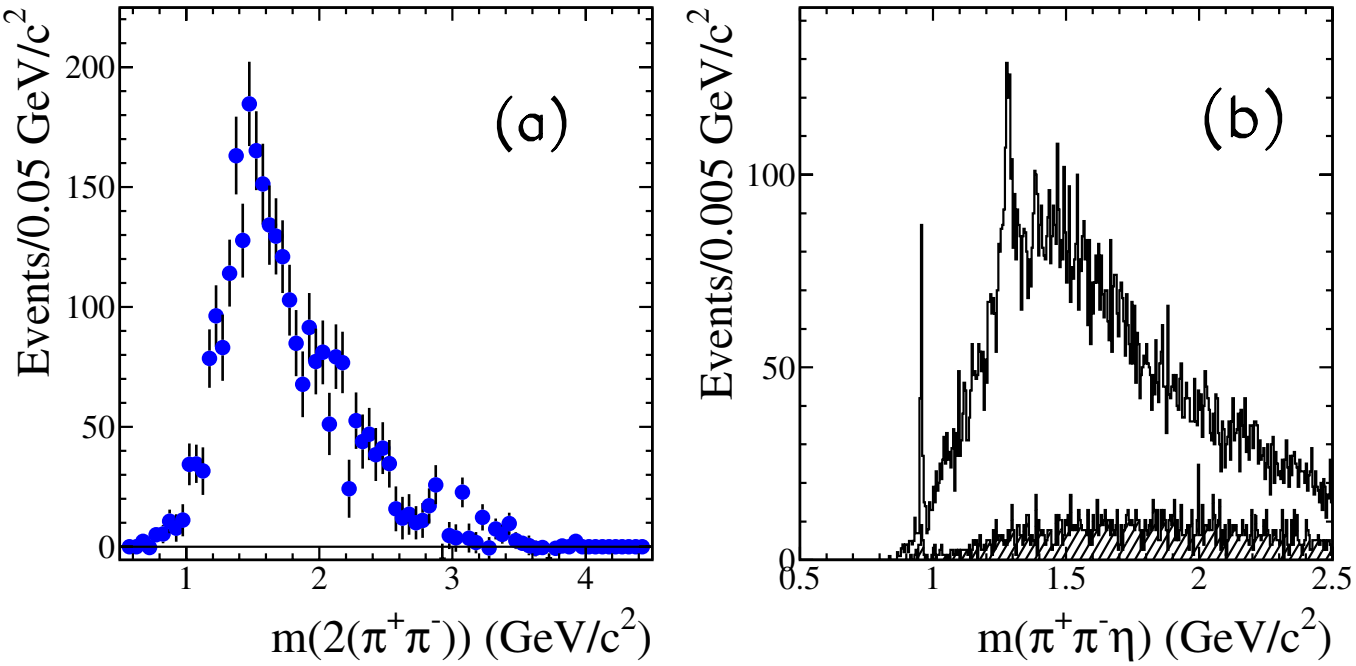

FIG. 23 (color online). (a) Background-subtracted invariant mass distribution for the four pions recoiling against the η in $2(\pi^+\pi^-)\eta$ events. (b) Invariant mass distribution for all $\pi^+\pi^-\eta$ combinations (four entries per event) in selected $2(\pi^+\pi^-)\eta$ candidates (open histogram) and the estimated non-ISR background (hatched).

represents a third order polynomial fit to the points, which we use to calculate the cross section. Simulations assuming dominance of the $\phi\pi^+\pi^-\pi^0$ and ηK^+K^- channels give consistent results, and we apply a 5% systematic uncertainty for possible model dependence, as in Sec. IV B.

We correct for track- and π^0-finding efficiencies, and the shape of the $\chi^2_{2K2\pi\pi^0}$ distribution as in Sec. IV B. We measure the kaon identification efficiency using $e^+e^- \to \phi(1020)\gamma \to K^+K^-\gamma$ events, as described in Ref. [11], and apply a correction of $+(2.0 \pm 2.0)\%$ to the efficiency.

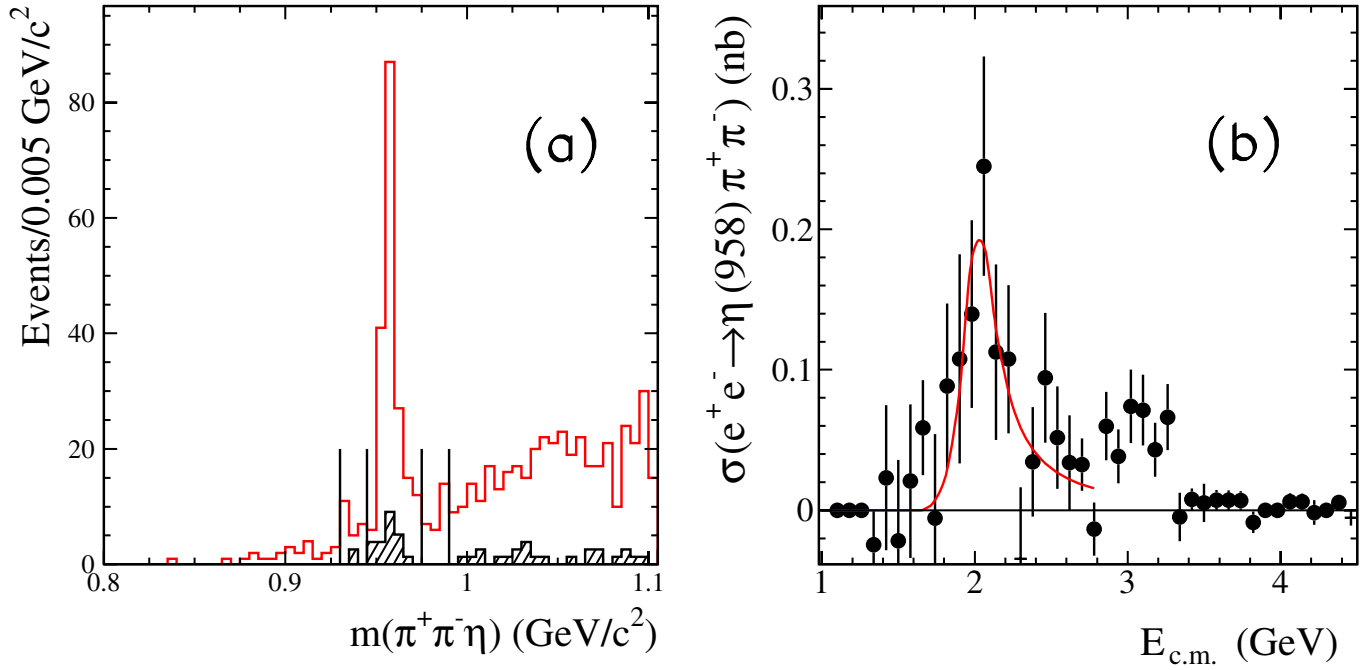

FIG. 24 (color online). (a) Distribution of the $\pi^+\pi^-\eta$ mass closest to the η' mass in the data (open histogram), along with the estimated non-ISR background contribution (hatched). The vertical lines indicate the $\eta'(958)$ signal and sideband regions. (b) The $e^+e^- \to \eta'(958)\pi^+\pi^-$ cross section obtained via ISR. The line is the result of the Breit-Wigner fit described in the text.

TABLE VIII. Measurements of the $e^+e^- \to \eta'(958)\pi^+\pi^-$ cross section (errors are statistical only).

$E_{\rm c.m.}$ (GeV)	σ (nb)	$E_{\rm c.m.}$ (GeV)	σ (nb)	$E_{\rm c.m.}$ (GeV)	σ (nb)	$E_{\rm c.m.}$ (GeV)	σ (nb)
1.58	0.02 ± 0.05	2.06	0.24 ± 0.08	2.54	0.05 ± 0.04	3.02	0.07 ± 0.03
1.66	0.06 ± 0.03	2.14	0.10 ± 0.06	2.62	0.03 ± 0.03	3.10	0.07 ± 0.03
1.74	0.01 ± 0.06	2.22	0.11 ± 0.05	2.70	0.03 ± 0.02	3.18	0.04 ± 0.02
1.82	0.07 ± 0.06	2.30	-0.05 ± 0.05	2.78	-0.01 ± 0.02	3.26	0.07 ± 0.02
1.90	0.11 ± 0.07	2.38	0.03 ± 0.04	2.86	0.06 ± 0.02	3.34	0.00 ± 0.02
1.98	0.16 ± 0.06	2.46	0.09 ± 0.05	2.94	0.04 ± 0.02	3.42	0.01 ± 0.01

The total efficiency correction is +8% and we estimate a systematic error of 10% for masses below 3.0 GeV/c^2, increasing to 30% at 4.5 GeV/c^2.

C. Cross section for $e^+e^- \to K^+K^-\pi^+\pi^-\pi^0$

We calculate the cross section for the $e^+e^- \to K^+K^-\pi^+\pi^-\pi^0$ process by dividing the number of events in each $K^+K^-\pi^+\pi^-\pi^0$ mass bin by the corrected efficiency and differential luminosity. We show the first measurement of this cross section in Fig. 29, with statistical errors only, and list the results in Table X. Again, the energy resolution is much smaller than the bin width and we apply no correction. The cross section rises to a peak value near 1 nb at 2.5 GeV, followed by a slow decrease with increasing energy. The only statistically significant structure is the J/ψ peak.

D. Substructure in the $K^+K^-\pi^+\pi^-\pi^0$ final state

Figure 30(a) shows a scatter plot of the $\pi^+\pi^-\pi^0$ mass versus the $K^+K^-\pi^+\pi^-\pi^0$ mass in the selected $K^+K^-\pi^+\pi^-\pi^0$ events. There are horizontal bands corresponding to the η signal and $\omega(782)$ resonance. The $\pi^+\pi^-\pi^0$ mass projection, Fig. 30(b), shows η and ω peaks, as well as a small signal for the $\phi(1020)$. The non-ISR background contribution is shown as the hatched histogram and also contains η and ω signals. Figure 31(a) shows a scatter plot of the $\pi^+\pi^-\pi^0$ mass versus the K^+K^- mass in the event. A vertical band corresponding to the $\phi(1020)$ is visible, and almost all η are produced through the $\phi\eta$ channel, whereas the $\omega(782)$ band is spread out across the plot. The K^+K^- mass projection in Fig. 31(b) shows a $\phi(1020)$ signal, but the non-ISR background distribution has no structure.

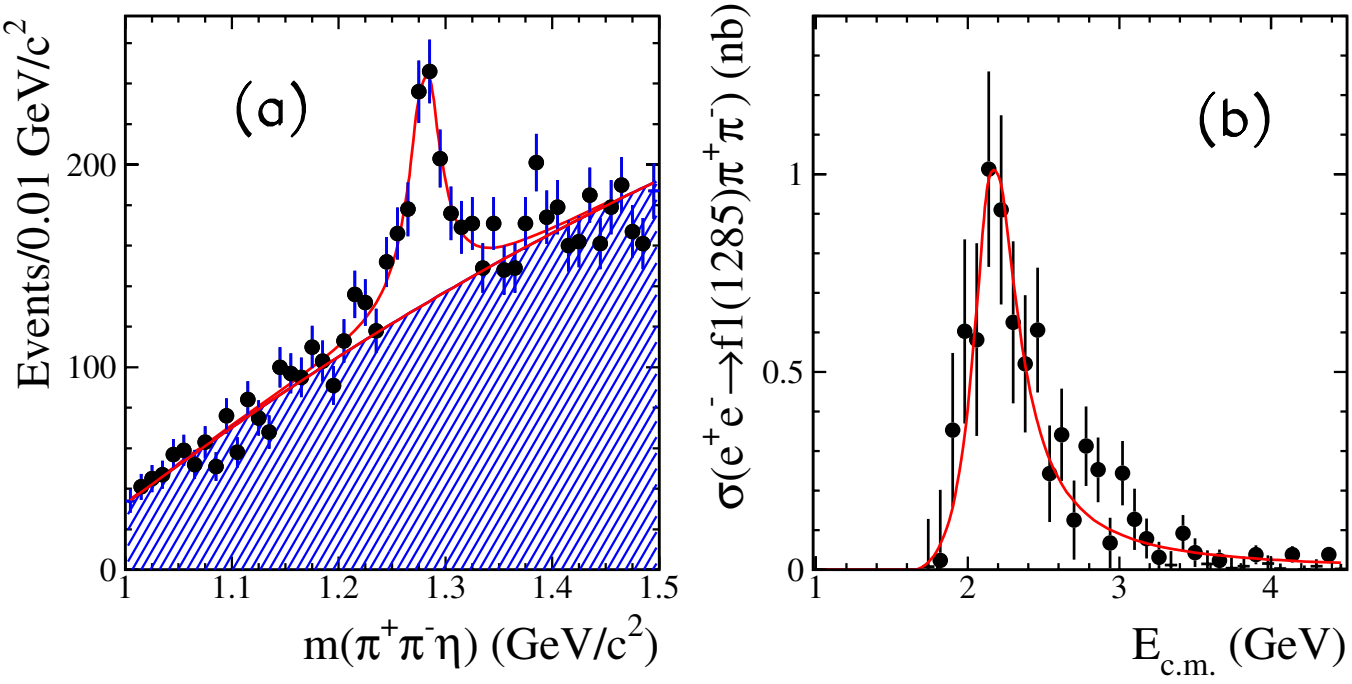

FIG. 25 (color online). (a) Distribution of the $\pi^+\pi^-\eta$ invariant mass in the 1–1.5 GeV/c^2 region for the data (points). The line represents the result of the fit described in the text, with the shaded region representing the background component. (b) The $e^+e^- \to f_1(1285)\pi^+\pi^-$ cross section obtained via ISR. The line is the result of the Breit-Wigner fit described in the text.

TABLE IX. Measurements of the $e^+e^- \to f_1(1285)\pi^+\pi^-$ cross section (errors are statistical only).

$E_{\rm c.m.}$ (GeV)	σ (nb)	$E_{\rm c.m.}$ (GeV)	σ (nb)	$E_{\rm c.m.}$ (GeV)	σ (nb)	$E_{\rm c.m.}$ (GeV)	σ (nb)
1.66	0.00 ± 0.00	2.14	0.99 ± 0.24	2.62	0.32 ± 0.12	3.10	0.11 ± 0.08
1.74	0.01 ± 0.11	2.22	0.89 ± 0.24	2.70	0.13 ± 0.10	3.18	0.08 ± 0.05
1.82	0.02 ± 0.18	2.30	0.64 ± 0.21	2.78	0.31 ± 0.10	3.26	0.03 ± 0.04
1.90	0.35 ± 0.20	2.38	0.54 ± 0.17	2.86	0.25 ± 0.08	3.34	0.02 ± 0.03
1.98	0.61 ± 0.23	2.46	0.61 ± 0.16	2.94	0.07 ± 0.06	3.42	0.09 ± 0.05
2.06	0.59 ± 0.24	2.54	0.25 ± 0.12	3.02	0.24 ± 0.08	3.50	0.05 ± 0.04

E. $\phi\eta$ intermediate state

Requiring the K^+K^- mass to be within ± 15 MeV/c^2 of the nominal $\phi(1020)$ mass and plotting the mass of the recoiling $\pi^+\pi^-\pi^0$ system below 700 MeV/c^2, we obtain the distribution shown in Fig. 32(a). The distribution from the ISR $\phi\eta$ simulation is also shown, and this channel can account for all entries below 700 MeV/c^2. Counting events with a three-pion mass in the 0.5–0.6 GeV/c^2 region in bins of the $K^+K^-\pi^+\pi^-\pi^0$ mass, and dividing by the corrected efficiency [Fig. 28(b)], differential luminosity and $\phi \to K^+K^-$ and $\eta \to \pi^+\pi^-\pi^0$ branching fractions, we obtain the $e^+e^- \to \phi\eta$ cross section shown in Fig. 32(b) and listed in Table XI.

The cross section shows a rise from threshold to a peak value of about 2 nb at around 1.7 GeV, followed by a monotonic decrease with increasing energy. This measurement is consistent with the more precise *BABAR* measurement in the $K^+K^-\gamma\gamma$ final state [26], which is also shown in Fig. 32(b)

F. $\omega(782)K^+K^-$ intermediate state

Figure 33(a) shows the $\pi^+\pi^-\pi^0$ mass distribution in the region near the $\omega(782)$ mass for all selected $K^+K^-\pi^+\pi^-\pi^0$ events in the data and the estimated non-ISR contribution. We first subtract the non-ISR background in each mass bin, then subtract the events in two sidebands, 690–735 and 825–870 MeV/c^2, from those in an ω signal region, 735–825 MeV/c^2. The mass distribution of the recoiling K^+K^- pair after this background subtraction shows no resonant structure. Dividing by the corrected efficiency, differential luminosity and $\omega \to \pi^+\pi^-\pi^0$ branching fraction, we obtain the first measurement of the $e^+e^- \to \omega(782)K^+K^-$ cross section, shown in Fig. 33(b) and listed in Table XII.

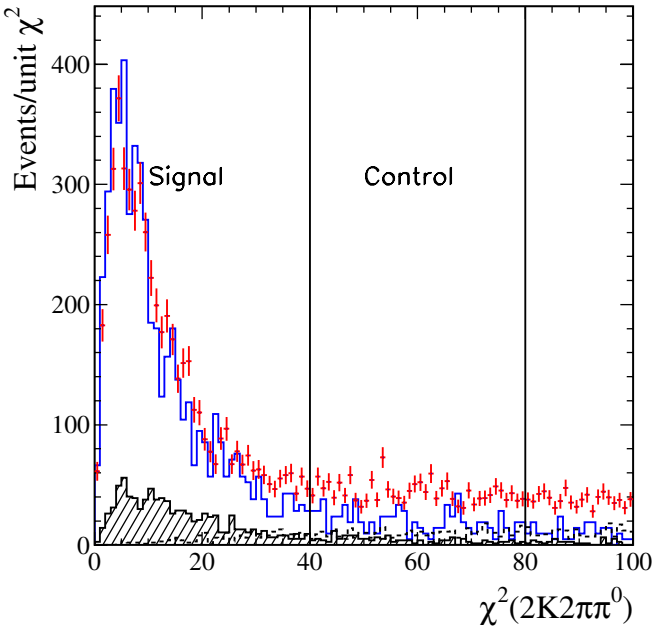

FIG. 26 (color online). Distribution of χ^2 from the 5C fit for $K^+K^-\pi^+\pi^-\pi^0$ candidates in the data (points). The open histogram is the distribution for simulated signal events, normalized as described in the text. The hatched and dashed histograms are the backgrounds from non-ISR events and ISR $K^+K^-\pi^+\pi^-$ events, respectively, estimated as described in the text.

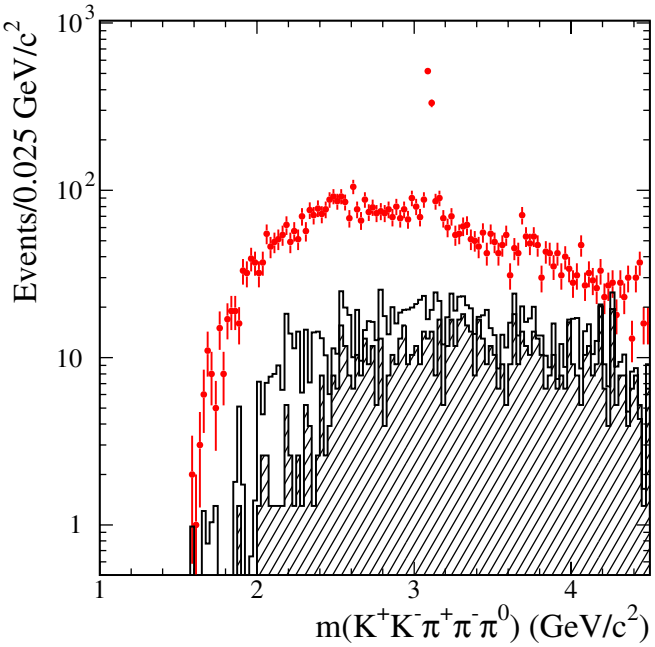

FIG. 27 (color online). Invariant mass distribution for selected $K^+K^-\pi^+\pi^-\pi^0$ candidates in the data (points). The hatched and open histograms represent the non-ISR background and the sum of all backgrounds, respectively.

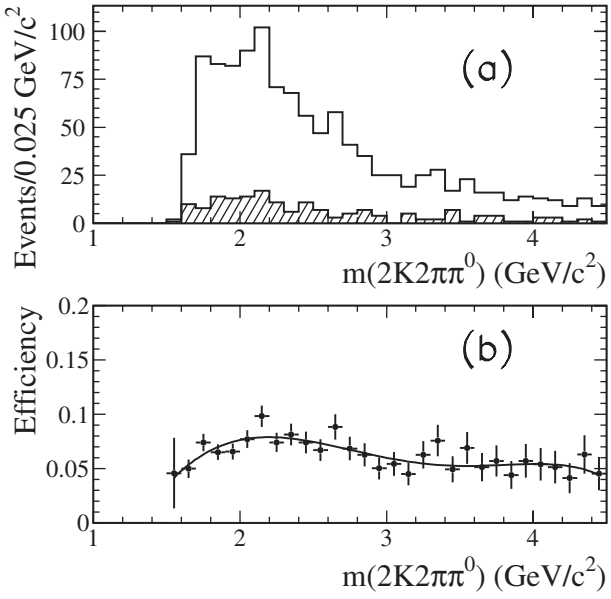

FIG. 28. (a) Invariant mass distribution for simulated $K^+K^-\pi^+\pi^-\pi^0$ events in the signal (open) and control (hatched) regions of Fig. 26. (b) Net reconstruction and selection efficiency as a function of mass obtained from this simulation; the curve represents a third order polynomial fit.

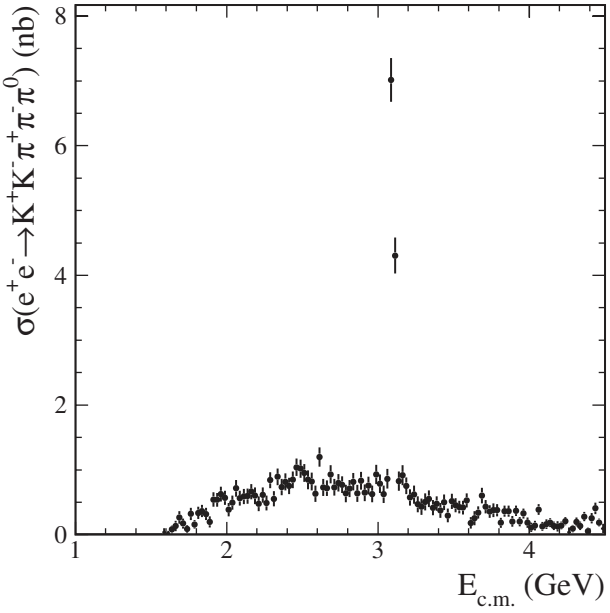

FIG. 29. The $e^+e^- \to K^+K^-\pi^+\pi^-\pi^0$ cross section as a function of e^+e^- c.m. energy measured with ISR data. The errors are statistical only.

TABLE X. Measurements of the $e^+e^- \to K^+K^-\pi^+\pi^-\pi^0$ cross section (errors are statistical only).

$E_{\rm c.m.}$ (GeV)	σ (nb)	$E_{\rm c.m.}$ (GeV)	σ (nb)	$E_{\rm c.m.}$ (GeV)	σ (nb)	$E_{\rm c.m.}$ (GeV)	σ (nb)
1.6125	0.02 ± 0.04	2.3375	0.89 ± 0.13	3.0625	0.86 ± 0.15	3.7875	0.38 ± 0.10
1.6375	0.08 ± 0.06	2.3625	0.73 ± 0.13	3.0875	7.01 ± 0.34	3.8125	0.18 ± 0.08
1.6625	0.13 ± 0.08	2.3875	0.82 ± 0.13	3.1125	4.31 ± 0.28	3.8375	0.36 ± 0.09
1.6875	0.27 ± 0.10	2.4125	0.75 ± 0.13	3.1375	0.83 ± 0.15	3.8625	0.36 ± 0.08
1.7125	0.17 ± 0.08	2.4375	0.85 ± 0.13	3.1625	0.92 ± 0.15	3.8875	0.20 ± 0.08
1.7375	0.09 ± 0.06	2.4625	1.04 ± 0.13	3.1875	0.75 ± 0.13	3.9125	0.37 ± 0.08
1.7625	0.32 ± 0.10	2.4875	1.02 ± 0.14	3.2125	0.57 ± 0.13	3.9375	0.20 ± 0.07
1.7875	0.16 ± 0.07	2.5125	0.95 ± 0.14	3.2375	0.62 ± 0.14	3.9625	0.33 ± 0.08
1.8125	0.34 ± 0.09	2.5375	0.85 ± 0.15	3.2625	0.47 ± 0.12	3.9875	0.18 ± 0.08
1.8375	0.36 ± 0.09	2.5625	0.82 ± 0.14	3.2875	0.43 ± 0.13	4.0125	0.11 ± 0.07
1.8625	0.32 ± 0.09	2.5875	0.63 ± 0.12	3.3125	0.50 ± 0.13	4.0375	0.14 ± 0.07
1.8875	0.20 ± 0.09	2.6125	1.20 ± 0.15	3.3375	0.55 ± 0.13	4.0625	0.39 ± 0.08
1.9125	0.54 ± 0.11	2.6375	0.73 ± 0.13	3.3625	0.42 ± 0.12	4.0875	0.13 ± 0.07
1.9375	0.54 ± 0.11	2.6625	0.71 ± 0.12	3.3875	0.48 ± 0.11	4.1125	0.16 ± 0.07
1.9625	0.63 ± 0.11	2.6875	0.93 ± 0.14	3.4125	0.37 ± 0.11	4.1375	0.19 ± 0.07
1.9875	0.57 ± 0.11	2.7125	0.73 ± 0.13	3.4375	0.50 ± 0.12	4.1625	0.13 ± 0.07
2.0125	0.39 ± 0.10	2.7375	0.80 ± 0.13	3.4625	0.29 ± 0.11	4.1875	0.13 ± 0.08
2.0375	0.49 ± 0.11	2.7625	0.77 ± 0.13	3.4875	0.52 ± 0.12	4.2125	0.14 ± 0.06
2.0625	0.71 ± 0.13	2.7875	0.64 ± 0.14	3.5125	0.45 ± 0.11	4.2375	0.21 ± 0.06
2.0875	0.56 ± 0.11	2.8125	0.71 ± 0.13	3.5375	0.42 ± 0.10	4.2625	0.04 ± 0.08
2.1125	0.59 ± 0.12	2.8375	0.82 ± 0.13	3.5625	0.42 ± 0.10	4.2875	0.10 ± 0.06
2.1375	0.59 ± 0.12	2.8625	0.64 ± 0.13	3.5875	0.53 ± 0.11	4.3125	0.20 ± 0.07
2.1625	0.66 ± 0.12	2.8875	0.83 ± 0.14	3.6125	0.18 ± 0.09	4.3375	0.14 ± 0.07
2.1875	0.60 ± 0.13	2.9125	0.65 ± 0.13	3.6375	0.25 ± 0.11	4.3625	0.28 ± 0.07
2.2125	0.48 ± 0.11	2.9375	0.76 ± 0.14	3.6625	0.34 ± 0.10	4.3875	0.05 ± 0.06
2.2375	0.61 ± 0.12	2.9625	0.63 ± 0.13	3.6875	0.60 ± 0.12	4.4125	0.25 ± 0.08
2.2625	0.49 ± 0.11	2.9875	0.93 ± 0.15	3.7125	0.43 ± 0.10	4.4375	0.41 ± 0.09
2.2875	0.84 ± 0.13	3.0125	0.78 ± 0.14	3.7375	0.36 ± 0.10	4.4625	0.19 ± 0.06
2.3125	0.55 ± 0.12	3.0375	0.62 ± 0.13	3.7625	0.38 ± 0.10	4.4875	0.10 ± 0.07

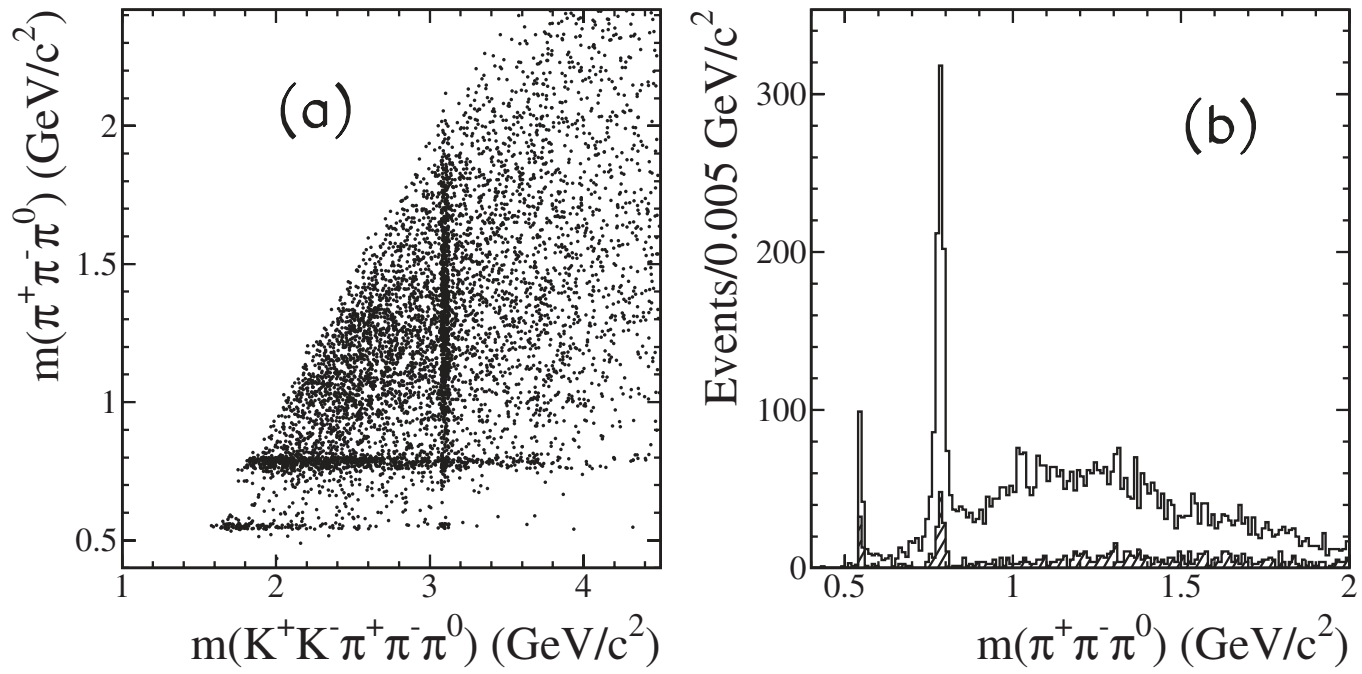

FIG. 30. (a) The $\pi^+\pi^-\pi^0$ mass versus two-kaon-three-pion mass, and (b) the $\pi^+\pi^-\pi^0$ mass projection for selected $K^+K^-\pi^+\pi^-\pi^0$ candidates. The hatched histogram represents the estimated non-ISR background.

The cross section rises from threshold to a peak value of about 0.55 nb at about 2 GeV, then decreases with increasing energy except for peaks at the J/ψ and $\psi(2S)$ masses. The events in the latter peak are partly due to the $\psi(2S) \to J/\psi\pi^+\pi^-$, $J/\psi \to K^+K^-\pi^0$ decay.

VII. $K^+K^-\pi^+\pi^-\eta$ FINAL STATE

A. Final selection and backgrounds

To suppress ISR $2(\pi^+\pi^-)\eta$ background, we fit each event under that hypothesis and require $\chi^2_{4\pi\eta} > 30$. The

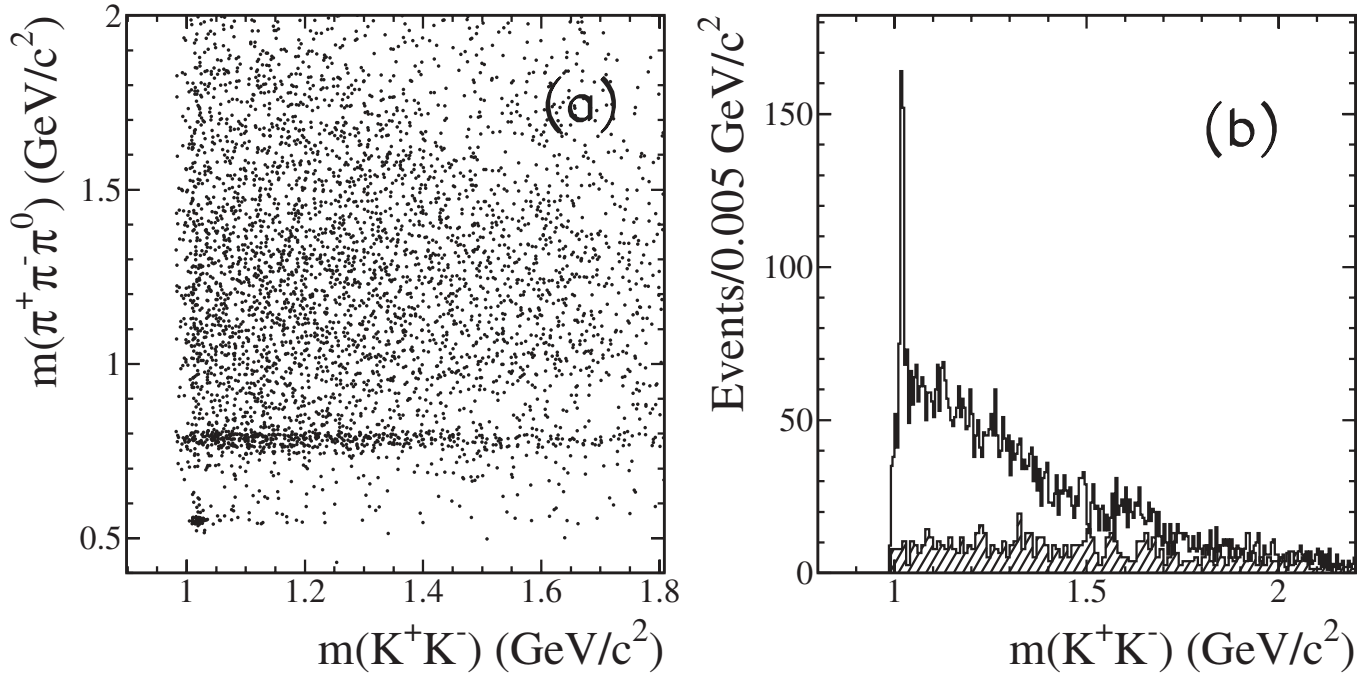

FIG. 31. (a) The $\pi^+\pi^-\pi^0$ mass versus the K^+K^- mass and (b) the K^+K^- mass projection for selected $K^+K^-\pi^+\pi^-\pi^0$ candidates. The hatched histogram represents the estimated non-ISR background.

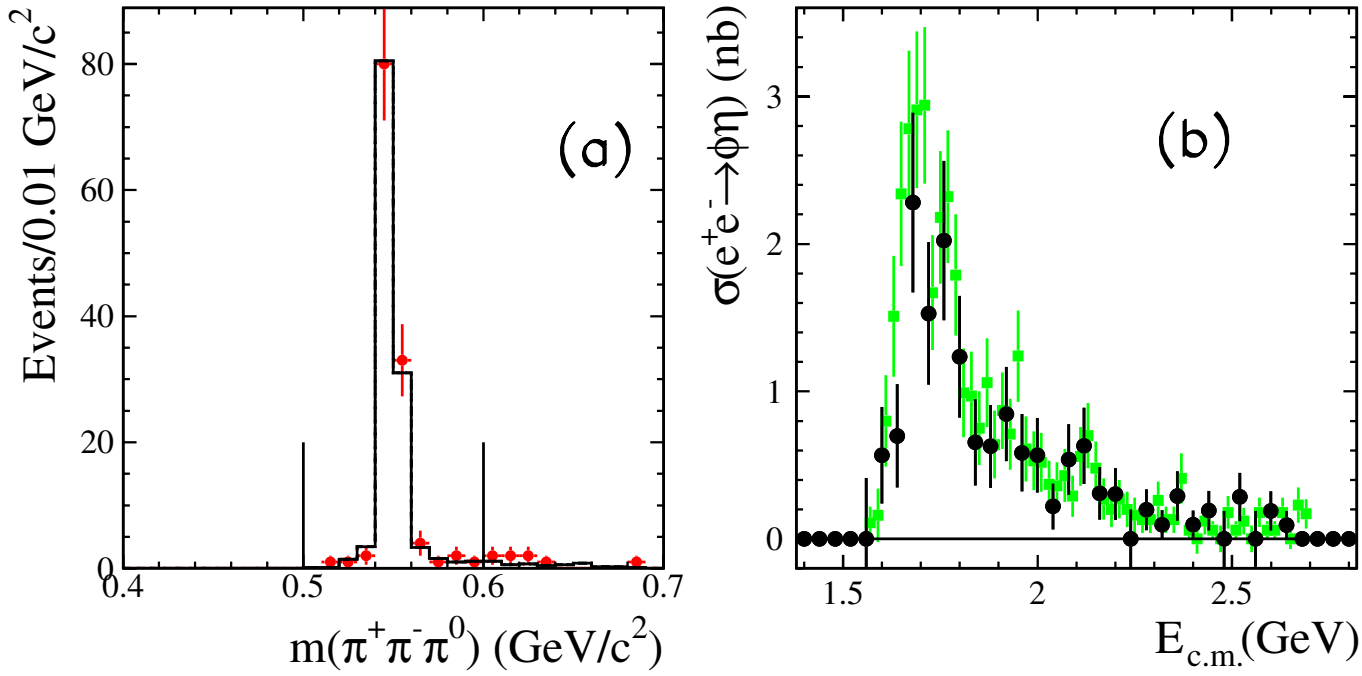

FIG. 32 (color online). (a) The $\pi^+\pi^-\pi^0$ mass distribution in the region below 700 MeV/c^2 for events with a K^+K^- mass within 15 MeV/c^2 of the ϕ mass (points). The histogram is the distribution for the ISR $\phi\eta$ simulation. (b) The $e^+e^- \to \phi\eta$ cross section measured here in the $K^+K^-\pi^+\pi^-\pi^0$ final state (large dots), compared with the previous *BABAR* measurement in the ISR $K^+K^-\gamma\gamma$ final state [26].

$\chi^2_{2K2\pi\eta}$ distribution for the remaining events is shown as points in Fig. 34, and the distribution for simulated ISR $\phi\eta \to K^+K^-\pi^+\pi^-\pi^0$ events (open histogram) is normalized to the data in the region $\chi^2_{2K2\pi\pi^0} < 20$. We do not simulate $K^+K^-\pi^+\pi^-\eta$ events, but we expect the resolution and efficiency to be indistinguishable from the generated mode. The hatched histogram represents the non-ISR background, which is dominated by $K^+K^-\pi^+\pi^-\pi^0\eta$ events and is evaluated from the simulation using the same scale factor as for the $K^+K^-\pi^+\pi^-\pi^0$ final state. We define a signal region, $\chi^2_{2K2\pi\eta} < 40$, containing 375 events and a control region, $40 < \chi^2_{2K2\pi\eta} < 80$, containing 162 events. We subtract the non-ISR background and the ISR-type background, estimated from the control region, to obtain a number of signal events.

B. Cross section for $K^+K^-\pi^+\pi^-\eta$

We calculate the cross section for the process $e^+e^- \to K^+K^-\pi^+\pi^-\eta$ as described in Sec. IV C, by dividing the number of background-subtracted events in each $K^+K^-\pi^+\pi^-\eta$ mass bin by the corrected detection efficiency and differential luminosity. Since the model dependence of the acceptance is small, we use the efficiency for $K^+K^-\pi^+\pi^-\pi^0$ events shown in Fig. 28(b), divided by the $\eta \to \gamma\gamma$ branching fraction and with an increased systematic error of 5%.

We show the cross section as a function of energy in Fig. 35 and list in Table XIII with statistical errors only. This is the first measurement of this cross section, which shows a rise from threshold to a maximum value of about 0.2 nb at about 2.8 GeV, followed by a monotonic decrease with increasing energy, except for a prominent peak at the

TABLE XI. Measurements of the $e^+e^- \to \phi(1020)\eta$ cross section (errors are statistical only).

$E_{c.m.}$ (GeV)	σ (nb)	$E_{c.m.}$ (GeV)	σ (nb)	$E_{c.m.}$ (GeV)	σ (nb)	$E_{c.m.}$ (GeV)	σ (nb)
1.56	0.00 ± 0.41	1.84	0.65 ± 0.29	2.12	0.63 ± 0.26	2.40	0.10 ± 0.10
1.60	0.57 ± 0.33	1.88	0.63 ± 0.28	2.16	0.31 ± 0.18	2.44	0.19 ± 0.13
1.64	0.70 ± 0.35	1.92	0.85 ± 0.32	2.20	0.30 ± 0.18	2.48	0.00 ± 0.19
1.68	2.28 ± 0.61	1.96	0.58 ± 0.26	2.24	0.00 ± 0.20	2.52	0.28 ± 0.16
1.72	1.53 ± 0.48	2.00	0.57 ± 0.25	2.28	0.20 ± 0.14	2.56	0.00 ± 0.19
1.76	2.02 ± 0.54	2.04	0.22 ± 0.16	2.32	0.10 ± 0.10	2.60	0.19 ± 0.13
1.80	1.23 ± 0.41	2.08	0.54 ± 0.24	2.36	0.29 ± 0.17	2.64	0.09 ± 0.09

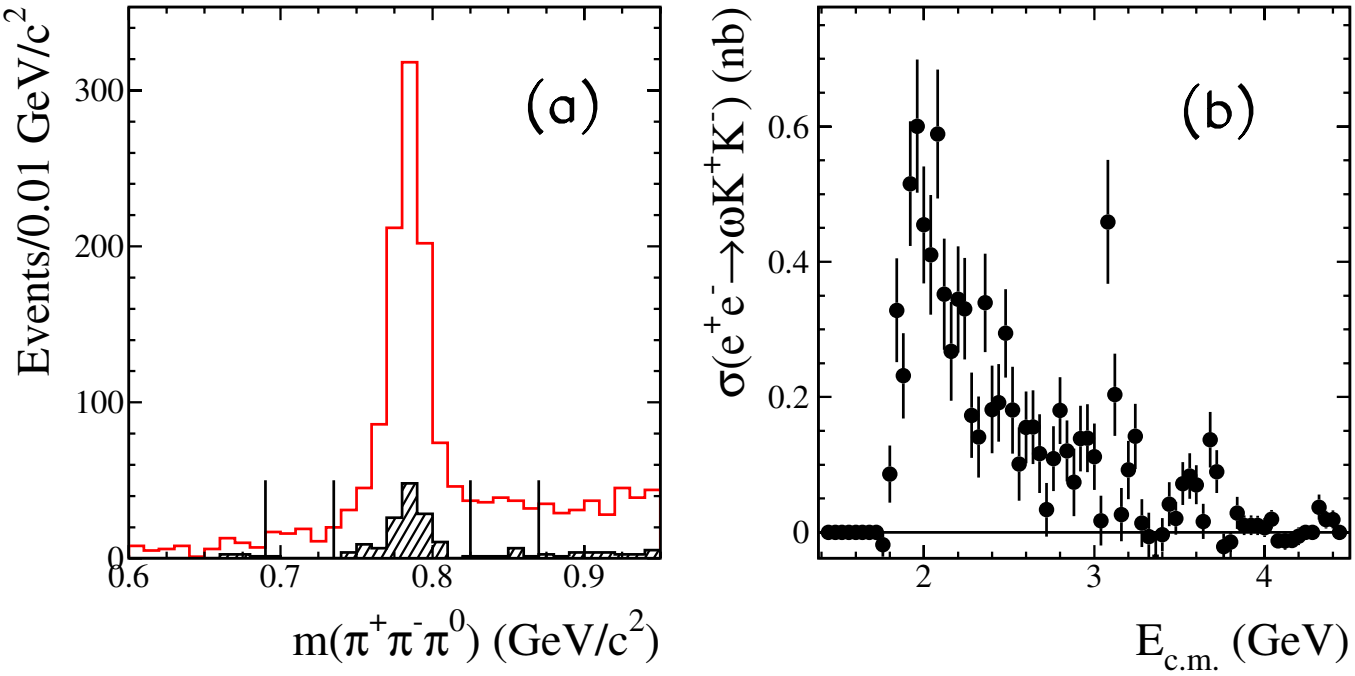

FIG. 33 (color online). (a) Expanded view of the $\pi^+\pi^-\pi^0$ invariant mass distribution [Fig. 30(b)] in the region near the $\omega(782)$ for all selected events in the data (open histogram) and the estimated non-ISR background (hatched). The vertical lines delimit the ω signal region and sidebands. (b) The $e^+e^- \to \omega(782)K^+K^-$ cross section obtained via ISR.

J/ψ mass. The systematic errors are similar to those for the other modes presented here, totaling about 10% at all energies.

C. Substructure in the $K^+K^-\pi^+\pi^-\eta$ final state

Figure 36(a) shows a scatter plot of the $\pi^+\pi^-\eta$ mass versus the $K^+K^-\pi^+\pi^-\eta$ mass and Fig. 36(b) shows the $\pi^+\pi^-\eta$ mass projection. A horizontal band and peak, respectively, corresponding to the $\eta'(958)$ are visible. The non-ISR background, shown as the shaded histogram in Fig. 36(b), is small, but may include a few η'. Figure 37(a) shows a scatter plot of the $\pi^+\pi^-\eta$ mass versus the K^+K^- mass in the event. A vertical band corresponding to the $\phi(1020)$ is visible, and almost all $\eta'(958)$ are produced through the $\phi\eta'$ channel. The K^+K^- mass projection in Fig. 37(b) shows a $\phi(1020)$

TABLE XII. Measurements of the $e^+e^- \to \omega(782)K^+K^-$ cross section (errors are statistical only).

$E_{c.m.}$ (GeV)	σ (nb)	$E_{c.m.}$ (GeV)	σ (nb)	$E_{c.m.}$ (GeV)	σ (nb)	$E_{c.m.}$ (GeV)	σ (nb)
1.80	0.09 ± 0.04	2.48	0.31 ± 0.07	3.16	0.07 ± 0.04	3.84	0.04 ± 0.02
1.84	0.33 ± 0.08	2.52	0.27 ± 0.06	3.20	0.12 ± 0.04	3.88	0.01 ± 0.01
1.88	0.25 ± 0.06	2.56	0.18 ± 0.05	3.24	0.17 ± 0.05	3.92	0.01 ± 0.01
1.92	0.52 ± 0.09	2.60	0.20 ± 0.05	3.28	0.06 ± 0.04	3.96	0.01 ± 0.01
1.96	0.60 ± 0.10	2.64	0.20 ± 0.05	3.32	0.07 ± 0.04	4.00	0.02 ± 0.01
2.00	0.45 ± 0.09	2.68	0.18 ± 0.06	3.36	0.06 ± 0.03	4.04	0.02 ± 0.01
2.04	0.43 ± 0.09	2.72	0.10 ± 0.04	3.40	0.01 ± 0.02	4.08	0.00 ± 0.01
2.08	0.61 ± 0.10	2.76	0.16 ± 0.05	3.44	0.07 ± 0.03	4.12	0.00 ± 0.01
2.12	0.37 ± 0.08	2.80	0.18 ± 0.05	3.48	0.04 ± 0.02	4.16	0.00 ± 0.01
2.16	0.28 ± 0.07	2.84	0.12 ± 0.05	3.52	0.07 ± 0.03	4.20	0.02 ± 0.01
2.20	0.39 ± 0.08	2.88	0.12 ± 0.05	3.56	0.08 ± 0.03	4.24	0.00 ± 0.01
2.24	0.36 ± 0.08	2.92	0.17 ± 0.05	3.60	0.07 ± 0.03	4.28	0.00 ± 0.01
2.28	0.17 ± 0.06	2.96	0.17 ± 0.05	3.64	0.05 ± 0.03	4.32	0.04 ± 0.02
2.32	0.22 ± 0.06	3.00	0.16 ± 0.05	3.68	0.14 ± 0.04	4.36	0.02 ± 0.01
2.36	0.34 ± 0.07	3.04	0.05 ± 0.04	3.72	0.09 ± 0.03	4.40	0.02 ± 0.01
2.40	0.23 ± 0.06	3.08	0.51 ± 0.09	3.76	0.02 ± 0.02	4.44	0.00 ± 0.01
2.44	0.19 ± 0.06	3.12	0.24 ± 0.06	3.80	0.00 ± 0.02	4.48	0.00 ± 0.01

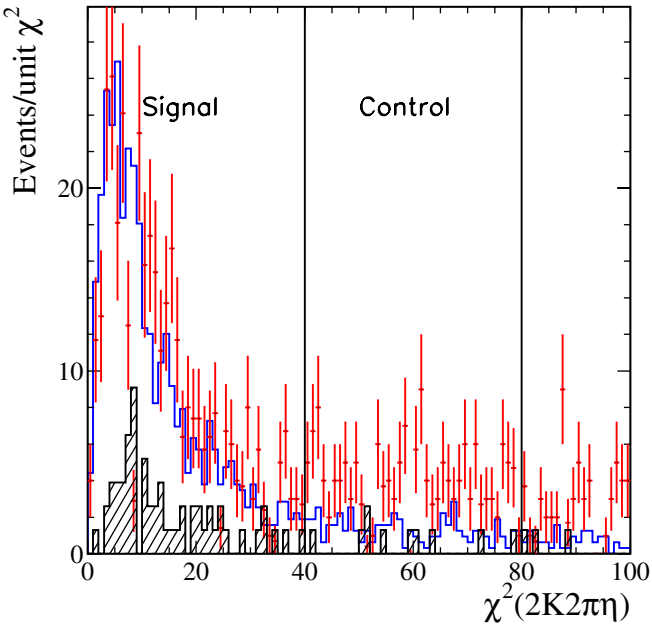

FIG. 34 (color online). Distribution of χ^2 from the 5C fit for $K^+K^-\pi^+\pi^-\eta$ candidates in the data (points). The open histogram is the distribution for simulated signal events, and the hatched histogram is the estimated background from non-ISR events.

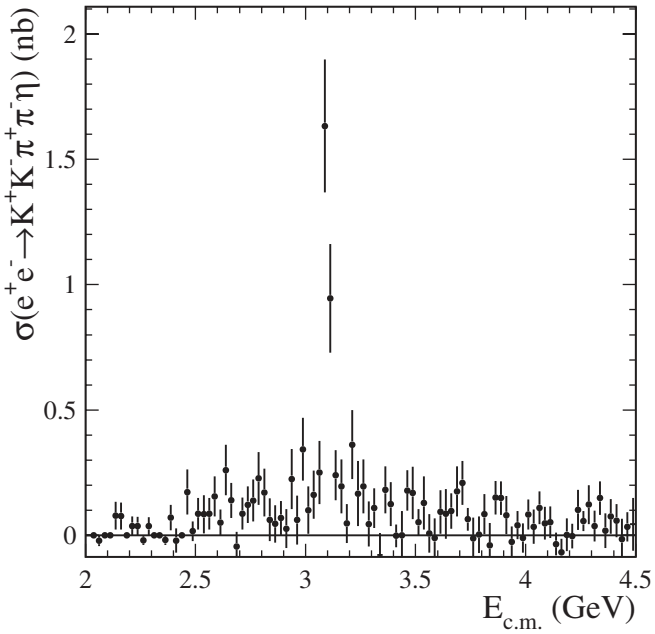

FIG. 35. The $e^+e^- \to K^+K^-\pi^+\pi^-\eta$ cross section as a function of c.m. energy measured with ISR data. Only statistical errors are shown.

signal, but the non-ISR background distribution has no resonant structure. Because of the low statistics, we do not study the mass dependence of these channels.

VIII. CHARMONIUM REGION

The data at masses above 3 GeV/c^2 can be used to measure or set limits on the branching fractions of narrow resonances, such as charmonia, and the narrow J/ψ and $\psi(2S)$ peaks allow measurements of our mass scale and resolution. Figures 38–41, show the invariant mass distributions for the selected $2(\pi^+\pi^-)\pi^0$, $2(\pi^+\pi^-)\eta$, $K^+K^-\pi^+\pi^-\pi^0$ and $K^+K^-\pi^+\pi^-\eta$ events, respectively, in this region, with finer binning than in the corresponding Figs. 2, 21, 27, and 35. We do not subtract any background, since it is small and nearly uniformly distributed. Signals from the J/ψ and $\psi(2S)$ are visible in all four distributions.

We fit these distributions using a sum of two Gaussian functions to describe each of the J/ψ and $\psi(2S)$ signals plus a polynomial to describe the remainder of the distribution. We fix the shape of the combination of the two Gaussians by fitting simulated events, but let the overall mean and width float in the fit, along with the amplitude and the coefficients of the polynomial. In all cases, the fitted mean values are within 1 MeV/c^2 of the PDG [5] J/ψ and $\psi(2S)$ masses, and the widths are consistent with the simulated resolutions within 10%.

In the J/ψ peak the fits yield 4990 ± 79 $2(\pi^+\pi^-)\pi^0$ events, 85 ± 14 $2(\pi^+\pi^-)\eta$ events, 768 ± 31 $K^+K^-\pi^+\pi^-\pi^0$ events, and 72.9 ± 9.4 $K^+K^-\pi^+\pi^-\eta$ events. From the number of observed events in each final state f, $N_{J/\psi\to f}$, we calculate the product of the J/ψ branching fraction to f and the J/ψ electronic width:

$$\mathcal{B}_{J/\psi\to f}\cdot\Gamma_{ee}^{J/\psi} = \frac{N_{J/\psi\to f}\cdot m_{J/\psi}^2}{6\pi^2\cdot d\mathcal{L}/dE\cdot\epsilon_f(m_{J/\psi})\cdot C}, \qquad (5)$$

where $d\mathcal{L}/dE = 65.6 \pm 2.0$ nb^{-1}/MeV and $\epsilon_f(m_{J/\psi})$ are the ISR luminosity and corrected selection efficiency, respectively, at the J/ψ mass and C is a conversion constant. We estimate efficiencies of 0.105 for the $2(\pi^+\pi^-)\pi^0$ and $2(\pi^+\pi^-)\eta$ final states, and 0.046 for the $K^+K^-\pi^+\pi^-\pi^0$ and $K^+K^-\pi^+\pi^-\eta$ modes, with systematic uncertainties of about 5% for modes with π^0 and about 7% for modes with η. Adding the error on the ISR luminosity in quadrature, we assign a 6% (7.5% for η) overall systematic uncertainty on each product.

Using $\Gamma_{ee}^{J/\psi} = 5.55 \pm 0.14$ keV [5], we obtain the branching fractions listed in Table XIV, along with the measured products and the current PDG values. The systematic errors include the 2.5% uncertainty on $\Gamma_{ee}^{J/\psi}$. The $J/\psi \to K^+K^-\pi^+\pi^-\eta$ channel has not been previously observed and the $K^+K^-\pi^+\pi^-\pi^0$ and $2(\pi^+\pi^-)\eta$ branching fractions are consistent and competitive with the PDG values. However, we find a $2(\pi^+\pi^-)\pi^0$ branching fraction 4.8 standard deviations higher than the PDG value.

In the $\psi(2S)$ peak the fits yield 410 ± 30 $2(\pi^+\pi^-)\pi^0$ events, 15.6 ± 7.6 $2(\pi^+\pi^-)\eta$ events, 31.8 ± 11.9 $K^+K^-\pi^+\pi^-\pi^0$ events, and 7.0 ± 4.0 $K^+K^-\pi^+\pi^-\eta$ events. Using a calculation analogous to Eq. (5), with

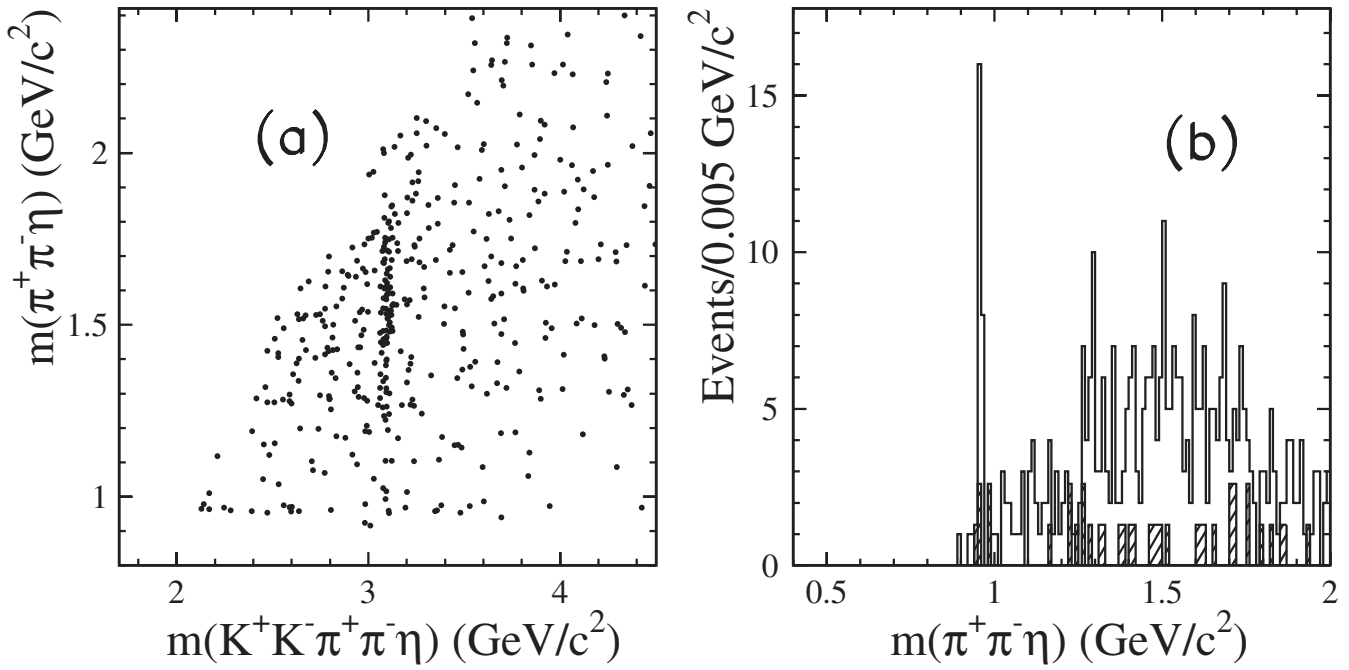

FIG. 36. (a) The $\pi^+\pi^-\eta$ mass versus the $K^+K^-\pi^+\pi^-\eta$ mass, and (b) the $\pi^+\pi^-\eta$ mass projection for selected $K^+K^-\pi^+\pi^-\eta$ candidates. The hatched histogram represents the estimated non-ISR background.

$d\mathcal{L}/dE = 84.0 \pm 2.5$ nb^{-1}/MeV and $\epsilon(\psi(2S)) = 0.0965$ (0.0400) for the $2(\pi^+\pi^-)\pi^0$ and $2(\pi^+\pi^-)\eta$ ($K^+K^-\pi^+\pi^-\pi^0$ and $K^+K^-\pi^+\pi^-\eta$) modes, we obtain the product of the $\psi(2S)$ branching fractions to these final states and its electronic width. Dividing by the world average value of $\Gamma_{ee}^{\psi(2S)}$ [5], we obtain the branching fractions listed in Table XIV. The $2(\pi^+\pi^-)\eta$ and $K^+K^-\pi^+\pi^-\eta$ branching fractions are first measurements, and the $K^+K^-\pi^+\pi^-\pi^0$ branching fraction is consistent with the PDG value.

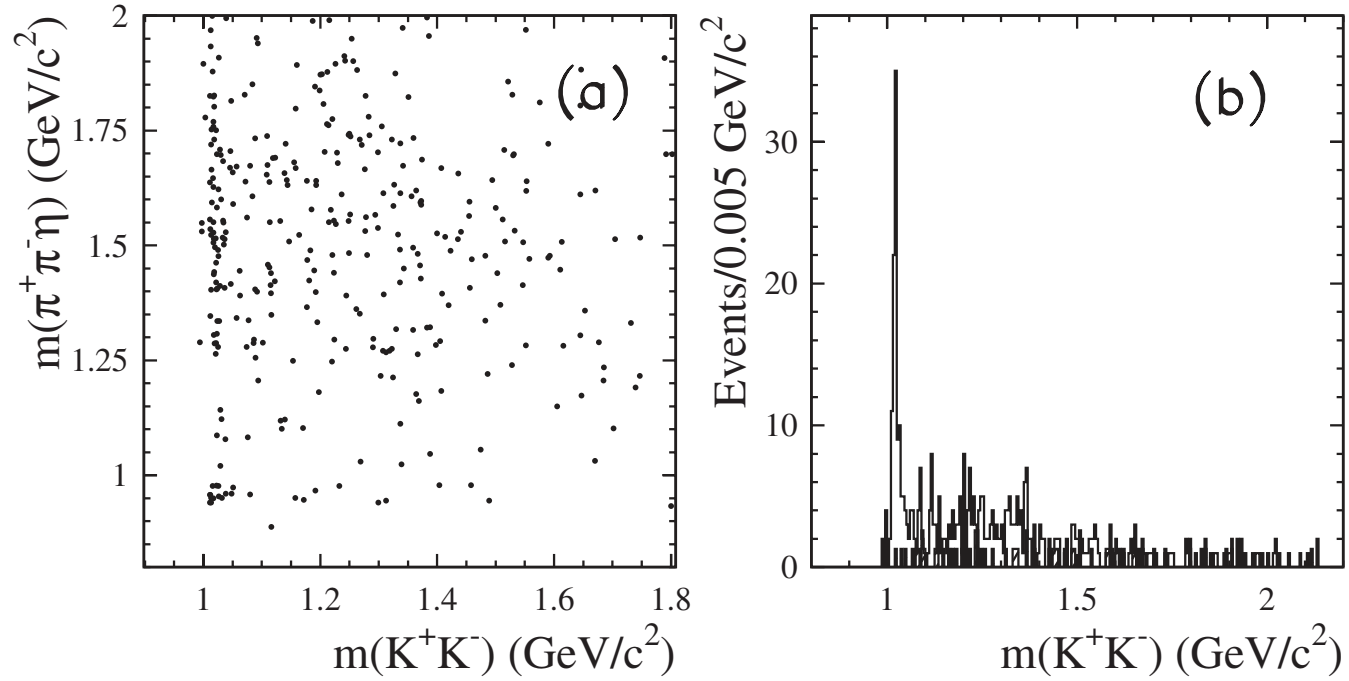

FIG. 37. (a) The $\pi^+\pi^-\eta$ mass versus the K^+K^- mass and (b) the K^+K^- mass projection for selected $K^+K^-\pi^+\pi^-\eta$ candidates. The hatched histogram represents the estimated non-ISR background.

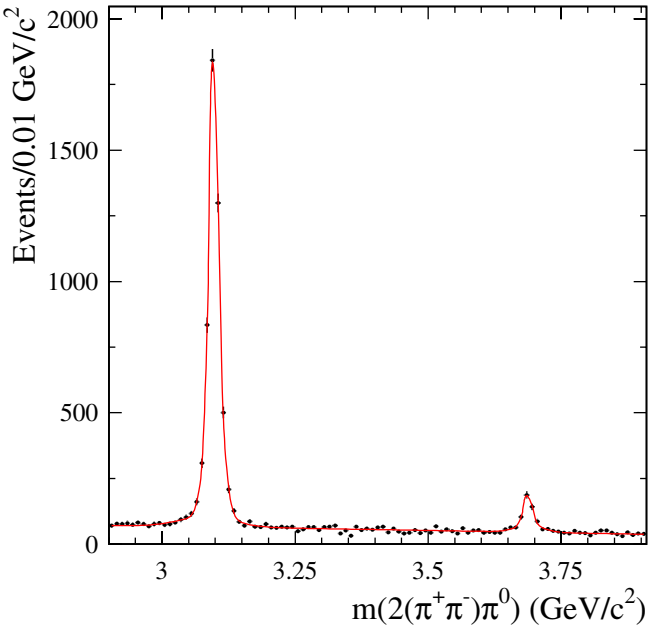

FIG. 38 (color online). Raw invariant mass distribution for all selected $e^+e^- \to 2(\pi^+\pi^-)\pi^0$ events in the charmonium region. The line represents the result of the fit described in the text.

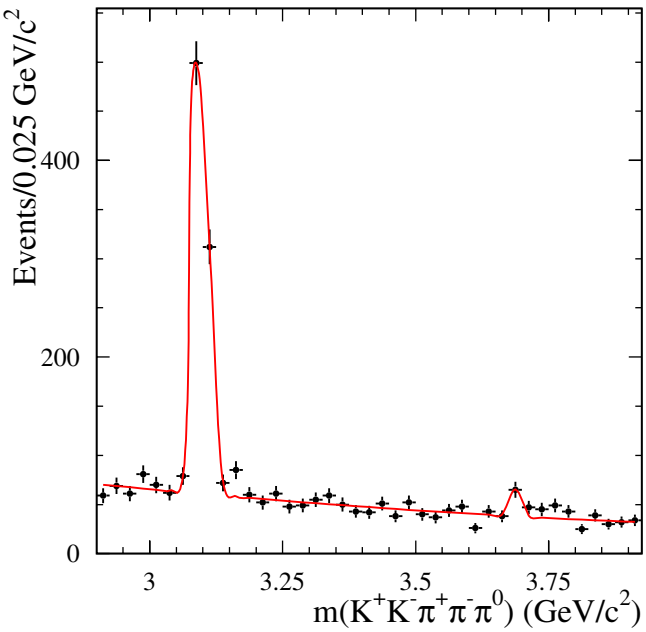

FIG. 40 (color online). Raw invariant mass distribution for all selected $e^+e^- \to K^+K^-\pi^+\pi^-\pi^0$ events in the charmonium region. The line represents the result of the fit described in the text.

However, we find a $2(\pi^+\pi^-)\pi^0$ branching fraction 7.6 standard deviations higher than the PDG value. We note that some of the observed $\psi(2S)$ could be due to the decay chain $\psi(2S) \to J/\psi\pi^+\pi^-$, $J/\psi \to \pi^+\pi^-\pi^0$, and we use this chain to check our result. The scatter plot of the $\pi^+\pi^-\pi^0$ mass closest to the J/ψ mass versus the $2(\pi^+\pi^-)\pi^0$ mass in Fig. 42(a) shows a cluster corresponding to this decay chain. We select events with a three-pion mass within 50 MeV/c^2 of the J/ψ mass [lines in

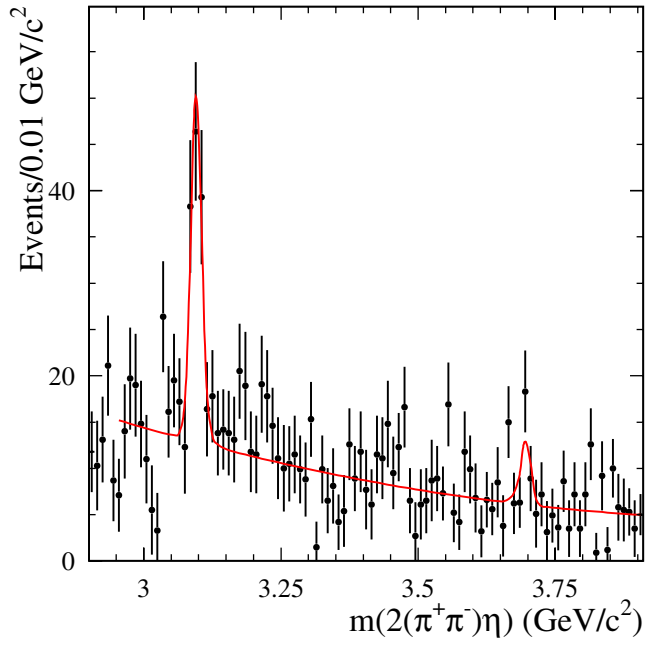

FIG. 39 (color online). Raw invariant mass distribution for all selected $e^+e^- \to 2(\pi^+\pi^-)\eta$ events in the charmonium region. The line represents the result of the fit described in the text.

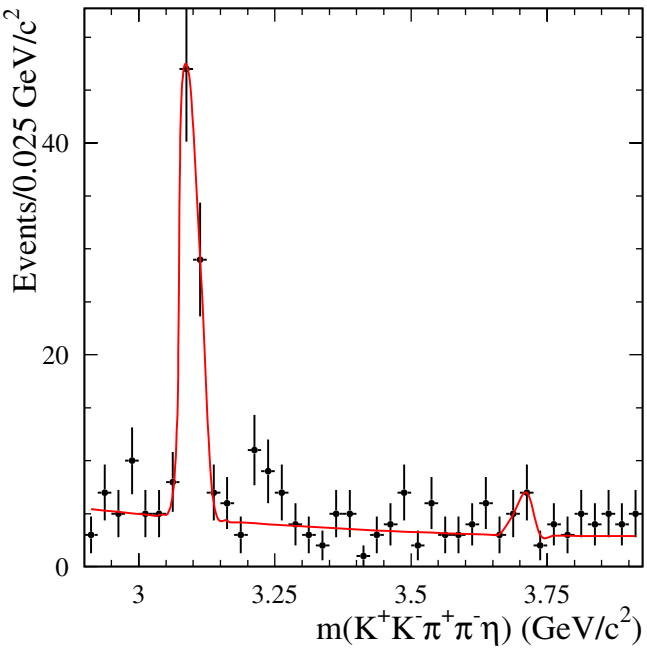

FIG. 41 (color online). Raw invariant mass distribution for all selected $e^+e^- \to K^+K^-\pi^+\pi^-\eta$ events in the charmonium region. The line represents the result of the fit described in the text.

TABLE XIII. Measurements of the $e^+e^- \to K^+K^-\pi^+\pi^-\eta$ cross section (errors are statistical only).

$E_{\text{c.m.}}$ (GeV)	σ (nb)	$E_{\text{c.m.}}$ (GeV)	σ (nb)	$E_{\text{c.m.}}$ (GeV)	σ (nb)	$E_{\text{c.m.}}$ (GeV)	σ (nb)
2.1125	0.00 ± 0.00	2.7125	0.09 ± 0.06	3.3125	0.11 ± 0.08	3.9125	0.08 ± 0.08
2.1375	0.08 ± 0.06	2.7375	0.12 ± 0.07	3.3375	-0.08 ± 0.09	3.9375	-0.03 ± 0.06
2.1625	0.08 ± 0.05	2.7625	0.14 ± 0.08	3.3625	0.18 ± 0.09	3.9625	0.04 ± 0.06
2.1875	0.00 ± 0.00	2.7875	0.23 ± 0.11	3.3875	0.12 ± 0.09	3.9875	-0.01 ± 0.06
2.2125	0.04 ± 0.04	2.8125	0.17 ± 0.09	3.4125	0.00 ± 0.05	4.0125	0.08 ± 0.06
2.2375	0.04 ± 0.04	2.8375	0.06 ± 0.08	3.4375	0.00 ± 0.10	4.0375	0.03 ± 0.07
2.2625	-0.02 ± 0.02	2.8625	0.05 ± 0.07	3.4625	0.18 ± 0.08	4.0625	0.11 ± 0.07
2.2875	0.04 ± 0.04	2.8875	0.07 ± 0.07	3.4875	0.17 ± 0.10	4.0875	0.05 ± 0.07
2.3125	0.00 ± 0.00	2.9125	0.03 ± 0.08	3.5125	0.05 ± 0.05	4.1125	0.05 ± 0.06
2.3375	0.00 ± 0.00	2.9375	0.22 ± 0.12	3.5375	0.13 ± 0.11	4.1375	-0.03 ± 0.05
2.3625	-0.02 ± 0.02	2.9625	0.06 ± 0.10	3.5625	0.01 ± 0.08	4.1625	-0.07 ± 0.05
2.3875	0.07 ± 0.05	2.9875	0.34 ± 0.13	3.5875	-0.01 ± 0.08	4.1875	0.00 ± 0.06
2.4125	-0.02 ± 0.05	3.0125	0.10 ± 0.09	3.6125	0.09 ± 0.09	4.2125	0.00 ± 0.05
2.4375	0.00 ± 0.00	3.0375	0.16 ± 0.10	3.6375	0.09 ± 0.10	4.2375	0.10 ± 0.08
2.4625	0.17 ± 0.09	3.0625	0.25 ± 0.13	3.6625	0.10 ± 0.07	4.2625	0.06 ± 0.04
2.4875	0.02 ± 0.04	3.0875	1.63 ± 0.26	3.6875	0.18 ± 0.10	4.2875	0.12 ± 0.08
2.5125	0.09 ± 0.06	3.1125	0.95 ± 0.22	3.7125	0.21 ± 0.09	4.3125	0.04 ± 0.06
2.5375	0.08 ± 0.08	3.1375	0.24 ± 0.10	3.7375	0.06 ± 0.05	4.3375	0.15 ± 0.07
2.5625	0.09 ± 0.06	3.1625	0.20 ± 0.11	3.7625	-0.01 ± 0.08	4.3625	0.02 ± 0.07
2.5875	0.16 ± 0.08	3.1875	0.05 ± 0.08	3.7875	0.00 ± 0.07	4.3875	0.08 ± 0.07
2.6125	0.05 ± 0.05	3.2125	0.36 ± 0.14	3.8125	0.08 ± 0.08	4.4125	0.06 ± 0.07
2.6375	0.26 ± 0.10	3.2375	0.17 ± 0.13	3.8375	-0.04 ± 0.09	4.4375	-0.02 ± 0.08
2.6625	0.14 ± 0.07	3.2625	0.20 ± 0.11	3.8625	0.15 ± 0.07	4.4625	0.03 ± 0.06
2.6875	-0.04 ± 0.06	3.2875	0.04 ± 0.09	3.8875	0.15 ± 0.07	4.4875	0.04 ± 0.11

Fig. 42(a)] and plot their $2(\pi^+\pi^-)\pi^0$ mass in Fig. 42(b). A fit yields 256 ± 17 $\psi(2S)$ events, and using the well measured $\psi(2S) \to J/\psi\pi^+\pi^-$ branching fraction of 0.318 ± 0.06 [5], we calculate a $J/\psi \to \pi^+\pi^-\pi^0$ branching fraction $\mathcal{B}_{J/\psi\to\pi^+\pi^-\pi^0} = (2.36 \pm 0.16 \pm 0.16)\%$ that is consistent with our previous measurement $\mathcal{B}_{J/\psi\to\pi^+\pi^-\pi^0} = (2.19 \pm 0.19)\%$ [8] as well as with the current PDG value. We obtain significantly higher values for both the J/ψ and $\psi(2S)$ branching fractions to $2(\pi^+\pi^-)\pi^0$ compared to previous experiments [5]. A similar difference was reported for the $J/\psi \to \pi^+\pi^-\pi^0$ decay in recent experiments [8,27].

We are also able to measure J/ψ and $\psi(2S)$ branching fractions for some of the submodes studied above.

TABLE XIV. Measurements of the J/ψ and $\psi(2S)$ branching fractions.

Measured quantity	Measured value (eV)	J/ψ or $\psi(2S)$ branching fraction (10^{-3}) Calculated, this work	PDG2006
$\Gamma_{ee}^{J/\psi}\cdot\mathcal{B}_{J/\psi\to2(\pi^+\pi^-)\pi^0}$	$303.0 \pm 5 \pm 18$	$54.6 \pm 0.9 \pm 3.4$	33.7 ± 2.6
$\Gamma_{ee}^{J/\psi}\cdot\mathcal{B}_{J/\psi\to\omega\pi^+\pi^-}\cdot\mathcal{B}_{\omega\to3\pi}$	$47.8 \pm 3.1 \pm 3.2$	$9.7 \pm 0.6 \pm 0.6$	7.2 ± 1.0
$\Gamma_{ee}^{J/\psi}\cdot\mathcal{B}_{J/\psi\to\eta\pi^+\pi^-}\cdot\mathcal{B}_{\eta\to3\pi}$	$0.51 \pm 0.22 \pm 0.03$	$0.40 \pm 0.17 \pm 0.03$	0.193 ± 0.023
$\Gamma_{ee}^{J/\psi}\cdot\mathcal{B}_{J/\psi\to2(\pi^+\pi^-)\eta}$	$5.16 \pm 0.85 \pm 0.39$	$2.35 \pm 0.39 \pm 0.20$	2.26 ± 0.28
$\Gamma_{ee}^{J/\psi}\cdot\mathcal{B}_{J/\psi\to K^+K^-\pi^+\pi^-\pi^0}$	$107.0 \pm 4.3 \pm 6.4$	$19.2 \pm 0.8 \pm 1.5$	12.0 ± 3.0
$\Gamma_{ee}^{J/\psi}\cdot\mathcal{B}_{J/\psi\to\phi\eta}\cdot\mathcal{B}_{\phi\to K^+K^-}\cdot\mathcal{B}_{\eta\to3\pi}$	$0.84 \pm 0.37 \pm 0.05$	$1.4 \pm 0.6 \pm 0.1$	0.74 ± 0.08
$\Gamma_{ee}^{J/\psi}\cdot\mathcal{B}_{J/\psi\to K^+K^-\pi^+\pi^-\eta}$	$3.3 \pm 1.3 \pm 0.2$	$1.36 \pm 0.50 \pm 0.10$	1.9 ± 0.4
$\Gamma_{ee}^{\psi(2S)}\cdot\mathcal{B}_{\psi(2S)\to2(\pi^+\pi^-)\pi^0}$	$10.2 \pm 1.3 \pm 0.8$	$4.7 \pm 0.6 \pm 0.4$	
$\Gamma_{ee}^{J/\psi}\cdot\mathcal{B}_{J/\psi\to\omega K^+K^-}\cdot\mathcal{B}_{\omega\to3\pi}$	$29.7 \pm 2.2 \pm 1.8$	$12.0 \pm 0.9 \pm 0.7$	2.66 ± 0.29
$\Gamma_{ee}^{\psi(2S)}\cdot\mathcal{B}_{\psi(2S)\to J/\psi\pi^+\pi^-}\cdot\mathcal{B}_{J/\psi\to3\pi}$	$18.6 \pm 1.2 \pm 1.1$	$23.6 \pm 1.6 \pm 1.6$	20.2 ± 1.4
$\Gamma_{ee}^{\psi(2S)}\cdot\mathcal{B}_{\psi(2S)\to\omega\pi^+\pi^-}\cdot\mathcal{B}_{\omega\to3\pi}$	$2.69 \pm 0.73 \pm 0.16$	$1.22 \pm 0.33 \pm 0.07$	0.66 ± 0.17
$\Gamma_{ee}^{\psi(2S)}\cdot\mathcal{B}_{\psi(2S)\to J/\psi\eta}\cdot\mathcal{B}_{\eta\to3\pi}\cdot\mathcal{B}_{J/\psi\to\mu^+\mu^-}$	$1.11 \pm 0.33 \pm 0.07$	$33.4 \pm 9.9 \pm 2.0$	30.9 ± 0.8
$\Gamma_{ee}^{\psi(2S)}\cdot\mathcal{B}_{\psi(2S)\to2(\pi^+\pi^-)\eta}$	$1.13 \pm 0.55 \pm 0.08$	$1.2 \pm 0.6 \pm 0.1$	
$\Gamma_{ee}^{\psi(2S)}\cdot\mathcal{B}_{\psi(2S)\to K^+K^-\pi^+\pi^-\pi^0}$	$4.4 \pm 1.3 \pm 0.3$	$1.8 \pm 0.5 \pm 0.1$	1.24 ± 0.10
$\Gamma_{ee}^{\psi(2S)}\cdot\mathcal{B}_{\psi(2S)\to K^+K^-\pi^+\pi^-\eta}$	$1.2 \pm 0.7 \pm 0.1$	$1.3 \pm 0.7 \pm 0.1$	

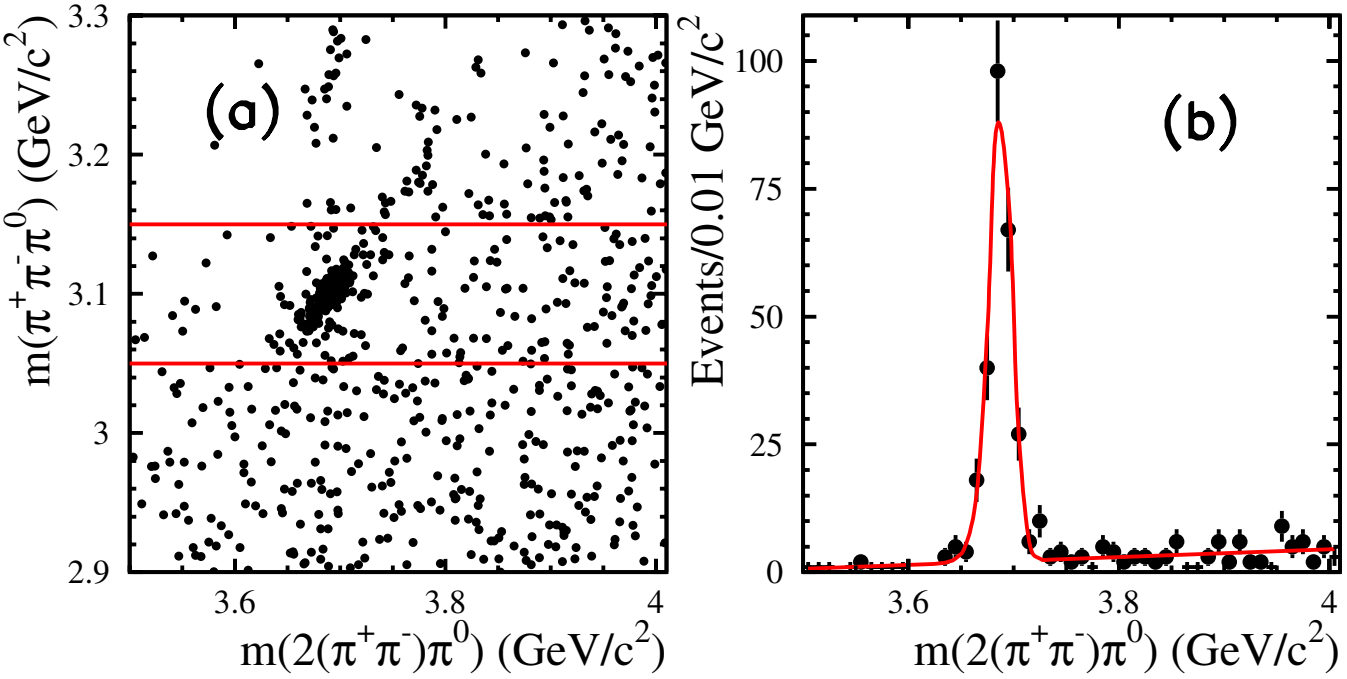

FIG. 42 (color online). (a) The $\pi^+\pi^-\pi^0$ mass closest to J/ψ mass versus the five-pion mass for selected $2(\pi^+\pi^-)\pi^0$ events. (b) The five-pion mass for events with a three-pion mass within 50 MeV of the J/ψ mass.

Figure 43 shows expanded views of the $2(\pi^+\pi^-)\pi^0$ mass distribution in the charmonium region for the $\eta\pi^+\pi^-$ and $\omega\pi^+\pi^-$ intermediate states. Our fits yield 8.9 ± 3.8 and 788 ± 51 J/ψ decays to $\eta\pi^+\pi^-$ and $\omega\pi^+\pi^-$, respectively, and 14.2 ± 4.2 and 37 ± 10 $\psi(2S)$ decays. We list the corresponding products and branching fractions in Table XIV. The $\psi(2S) \to \eta\pi^+\pi^-$ branching fraction is very small [5] and the observed events are from the decay chain $\psi(2S) \to J/\psi\eta$, $J/\psi \to \mu^+\mu^-$, $\eta \to \pi^+\pi^-\pi^0$. The result in Table XIV assumes this decay chain. We

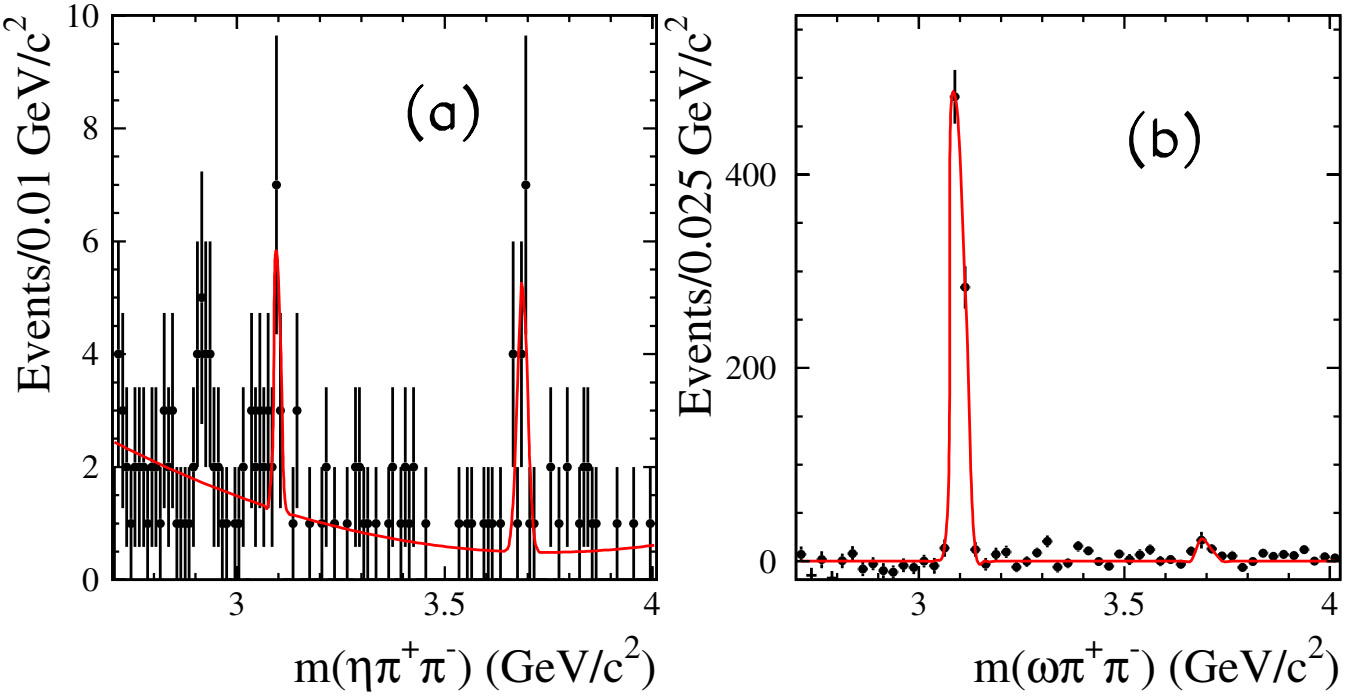

FIG. 43 (color online). Background-subtracted $2(\pi^+\pi^-)\pi^0$ invariant mass distributions in the charmonium region for events with a $\pi^+\pi^-\pi^0$ mass in the (a) η and (b) $\omega(782)$ mass region.

also observe 6.0 ± 2.7 and 24 ± 9 events in the J/ψ peaks for the $\phi\eta$ and $K^+K^-\omega$ modes, respectively. The corresponding products are also listed in Table XIV.

IX. SUMMARY

The photon energy and charged particle momentum resolutions together with the particle identification capabilities of the *BABAR* detector permit the reconstruction of $e^+e^- \to 2(\pi^+\pi^-)\pi^0$, $2(\pi^+\pi^-)\eta$, $K^+K^-\pi^+\pi^-\pi^0$ and $K^+K^-\pi^+\pi^-\eta$ events produced at low effective e^+e^- c.m. energy via ISR in data taken in the $\Upsilon(4S)$ mass region. Luminosity and efficiency can be understood with 6%–10% accuracy, so that ISR production yields useful measurements of R, the ratio of the hadronic to dimuon cross section values, used for the $(g-2)_\mu$ calculations.

Our measurements of the $e^+e^- \to 2(\pi^+\pi^-)\pi^0$ cross section represent a significant improvement upon existing data in both energy range and precision. In addition, these data provide new information on hadron spectroscopy. The observed $e^+e^- \to \omega\pi^+\pi^-$ and $\eta\pi^+\pi^-$ cross sections show evidence of resonant structures around 1.4–1.7 GeV/c^2, which were previously observed by DM2 and interpreted as $\omega(1420)$ and $\omega(1650)$ resonances. We obtain new measurements of the parameters of these resonances, which confirm the results of our previous study of ISR $\pi^+\pi^-\pi^0$ events, that the $\omega(1650)$ is substantially narrower than currently listed in PDG.

We also use this final state to make the first measurements of the $e^+e^- \to \omega f_0(980)$ and $\rho(770)3\pi$ cross sections. In the latter events, there is an isovector resonant structure with $m = 1.243 \pm 0.012 \pm 0.020$ GeV/c^2 and $\Gamma = 0.410 \pm 0.031 \pm 0.030$ GeV in the three-pion system recoiling against the $\rho(770)$.

We present the first measurements of the cross sections for $e^+e^- \to 2(\pi^+\pi^-)\eta$, $\eta'(958)\pi^+\pi^-$ and $f_1(1285)\pi^+\pi^-$. We measure the mass and width of the $f_1(1285)$, and observe a candidate $\rho(2150)$ resonance with $m_{\rho(2150)} = 2.15 \pm 0.04 \pm 0.05$ GeV/c^2 and $\Gamma_{\rho(2150)} = 0.35 \pm 0.04 \pm 0.05$ GeV.

We present the first measurements of the cross sections for $e^+e^- \to K^+K^-\pi^+\pi^-\pi^0$, $K^+K^-\omega$ and $K^+K^-\pi^+\pi^-\eta$. Using the latter final state, we measure a contribution from $e^+e^- \to \phi\eta$ consistent with our measurement in the $K^+K^-\gamma\gamma$ final state [26].

The final states analyzed in this paper, based on 232 fb^{-1} of *BABAR* data in the 1.0–4.5 GeV/c^2 mass range, are already better in quality and precision than the direct measurements from the DCI and ADONE machines, and do not suffer from the relative normalization uncertainties which seem to exist for direct measurements of these final states.

The ISR events also allow a study of J/ψ and $\psi(2S)$ production, and the measurement of 15 products of branching fractions into observed modes and the e^+e^- width of the J/ψ or $\psi(2S)$. Three of these are first measurements, and two others are the most precise measurements to date, thanks to our relatively small systematic error due to acceptance. We observe substantial discrepancies with respect to the previous experiments in the $J/\psi \to 2(\pi^+\pi^-)\pi^0$ and $\psi(2S) \to 2(\pi^+\pi^-)\pi^0$ decay modes.

ACKNOWLEDGMENTS

We are grateful for the extraordinary contributions of our PEP-II colleagues in achieving the excellent luminosity and machine conditions that have made this work possible. The success of this project also relies critically on the expertise and dedication of the computing organizations that support *BABAR*. The collaborating institutions wish to thank SLAC for its support and the kind hospitality extended to them. This work is supported by the U.S. Department of Energy and National Science Foundation, the Natural Sciences and Engineering Research Council (Canada), the Commissariat à l'Energie Atomique and Institut National de Physique Nucléaire et de Physique des Particules (France), the Bundesministerium für Bildung und Forschung and Deutsche Forschungsgemeinschaft (Germany), the Istituto Nazionale di Fisica Nucleare (Italy), the Foundation for Fundamental Research on Matter (The Netherlands), the Research Council of Norway, the Ministry of Science and Technology of the Russian Federation, Ministerio de Educación y Ciencia (Spain), and the Science and Technology Facilities Council (United Kingdom). Individuals have received support from the Marie-Curie IEF program (European Union) and the A. P. Sloan Foundation.

[1] V. N. Baier and V. S. Fadin, Phys. Lett. B **27**, 223 (1968).
[2] A. B. Arbuzov *et al.*, J. High Energy Phys. 12 (1998) 009.
[3] S. Binner, J. H. Kühn, and K. Melnikov, Phys. Lett. B **459**, 279 (1999).
[4] M. Benayoun *et al.*, Mod. Phys. Lett. A **14**, 2605 (1999).
[5] Review of Particle Physics, W.-M. Yao *et al.*, J. Phys. G **33**, 1 (2006).
[6] M. Davier, Nucl. Phys. B, Proc. Suppl. **169**, 288 (2007).
[7] B. Aubert *et al.* (*BABAR* Collaboration), Phys. Rev. D **69**, 011103 (2004).

[8] B. Aubert *et al.* (*BABAR* Collaboration), Phys. Rev. D **70**, 072004 (2004).
[9] B. Aubert *et al.* (*BABAR* Collaboration), Phys. Rev. D **71**, 052001 (2005).
[10] B. Aubert *et al.* (*BABAR* Collaboration), Phys. Rev. D **73**, 052003 (2006).
[11] B. Aubert *et al.* (*BABAR* Collaboration), Phys. Rev. D **76**, 012008 (2007).
[12] A. Cordier *et al.* (DM1 Collaboration), Phys. Lett. B **106**, 155 (1981).
[13] A. Antonelli *et al.* (DM2 Collaboration), Phys. Lett. B **212**, 133 (1988).
[14] A. Antonelli *et al.* (DM2 Collaboration), Z. Phys. C **56**, 15 (1992).
[15] A. Akhmetshin *et al.* (CMD2 Collaboration), Phys. Lett. B **489**, 125 (2000).
[16] V. Druzhinin *et al.* (ND Collaboration), Phys. Lett. B **174**, 115 (1986).
[17] B. Aubert *et al.* (*BABAR* Collaboration), Nucl. Instrum. Methods Phys. Res., Sect. A **479**, 1 (2002).
[18] H. Czyż and J. H. Kühn, Eur. Phys. J. C **18**, 497 (2001).
[19] A. B. Arbuzov *et al.*, J. High Energy Phys. 10 (1997) 001.
[20] M. Caffo, H. Czyż, and E. Remiddi, Nuovo Cimento Soc. Ital. Fis. A **110**, 515 (1997); Phys. Lett. B **327**, 369 (1994).
[21] E. Barberio, B. van Eijk, and Z. Was, Comput. Phys. Commun. **66**, 115 (1991).
[22] S. Agostinelli *et al.* (GEANT4 Collaboration), Nucl. Instrum. Methods Phys. Res., Sect. A **506**, 250 (2003).
[23] T. Sjostrand, Comput. Phys. Commun. **82**, 74 (1994).
[24] S. Jadach and Z. Was, Comput. Phys. Commun. **85**, 453 (1995).
[25] B. Aubert *et al.* (*BABAR* Collaboration), Phys. Rev. D **74**, 012002 (2006).
[26] B. Aubert *et al.* (*BABAR* Collaboration), arXiv:0710.4451.
[27] J. Z. Bai *et al.* (BES Collaboration), Phys. Rev. D **70**, 012005 (2004).